Stark Spectroscopy and Atom Optics with Rydberg Helium Atoms

A Thesis Presented

by

Andreas Vernaleken

to

The Graduate School

in Partial Fulfillment of the Requirements

for the Degree of

Master of Arts

in

Physics

Stony Brook University

August 2006

Stony Brook University

The Graduate School

Andreas Vernaleken

We, the Thesis committee for the above candidate for the Master of Arts degree, hereby recommend acceptance of the Thesis.

Distinguished Teaching Professor Harold J. Metcalf, Thesis Advisor

Department of Physics and Astronomy, Stony Brook University

Professor Chris J. Jacobsen

Department of Physics and Astronomy, Stony Brook University

Assistant Professor Adam Durst

Department of Physics and Astronomy, Stony Brook University

This Thesis is accepted by the Graduate School.

Dean of the Graduate School

Abstract of the Thesis

Stark Spectroscopy and Atom Optics with Rydberg Helium Atoms

by

Andreas Vernaleken

Master of Arts

in

Physics

Stony Brook University

2006

The key concept of atom optics is the controlled manipulation of atomic translational motion. Whereas most atom optical experiments rely on forces arising from the interaction of ground state atoms with laser light, schemes to exert forces on Rydberg atoms taking advantage of their unique properties were first suggested by Breeden and Metcalf in 1981 [1].

Rydberg atoms have an enormous dipole moment and thus interact strongly with inhomogeneous electrostatic fields. In order to exploit this property for effective focusing of a beam of metastable helium atoms, we use the coherent Stimulated Raman Adiabatic Passage (STIRAP) [2; 3; 4] excitation technique to efficiently transfer population from the metastable state to selected Rydberg

states. STIRAP is successfully implemented in the three-level ladder system $2\,^3\mathrm{S}_1 \rightarrow 3\,^3\mathrm{P}_2 \rightarrow n\,^3\mathrm{L}_J$ of atomic helium and considerable population transfer can be observed experimentally.

Precision spectroscopy on the Stark-shifted energy level structure of the Rydberg helium atoms enables us to record a Stark map and to experimentally determine the Rydberg state with the highest transfer efficiency. The results can be compared to the theoretical Stark map and to the oscillator strengths obtained from numerical calculations. Furthermore, the Autler-Townes effect [5] is observed and exploited to adjust the Rabi frequencies of our lasers so that they meet the conditions for STIRAP.

Finally, we successfully demonstrate the focusing effect of an electrostatic hexapole lens on neutral atoms by manipulating the trajectories of the Rydberg helium atoms created by means of the STIRAP excitation technique. Once this atom optical technique has been perfected, nanolithography lies within the scope of future applications.

Contents

List of Figures

List of Tables

Acknowledgements

Looking back on one of the most challenging, entertaining, thrilling, and wonderful years of my life, I would like to thank the people who contributed both directly to this work and to the overall success of my stay in the United States:

First and foremost, I want to thank my advisor Hal for giving me the opportunity of working in his lab and for taking care of me in his inimitable way throughout the year. His enthusiasm for physics was definitely contagious, and he did an incredible job in providing a fruitful environment for research. It will be very hard if not impossible to find a better advisor.

Seung did not only teach me everything about the Rydberg experiment in countless nights in the lab, but also shared his invaluable non-physics experiences with me. Working, joking and celebrating with him was always a great pleasure, and I am looking forward to visiting him on Jeju island soon.

Claire, Esther, Jason, Michael, and Xiyue mastered the numerous ups and downs of experimental physics with me. They made the lab one of my favorite places, and I enjoyed both working and hanging out with them a lot. Jonathan, Kyung, MinMin, Tak Chu, and Xiaoxu blended into that hard core of our group very well. It was a great pleasure to work with Marty both in the LTC and in

our group and to benefit from his experience. I am also grateful to Tom and John who were always willing to share their enormous knowledge with me.

Among the staff in the department, I would especially like to thank Pat and Linda, who kept most of the bureaucracy away from me, and also Pete, Chuck, Walter and Mark, who helped me with all kinds of technical problems.

I am indebted to those responsible for the exchange program between Würzburg and Stony Brook and hope that they realize that such a unique cooperation should persist despite all current funding problems.

My time in Stony Brook has been exceptionally great because of all the wonderful people from in- and outside the department with whom I spent most of my time when not working. Thanks for countless rides, invitations to parties and weddings, giving me an understanding of the American way of life, and just all the fun we had! Similarly, I would like to thank all those who kept in touch with me from all over the world during the last year.

My housemates at 4 Friends Road, Christian and Michael, have not only made our place a resort from all worries of daily life, but also been my primary source of help, adventures, and entertainment throughout the year. We have been an incomparably great team!

Last but not least, I want to thank my family who supported and encouraged me and kept me grounded at all times during my stay abroad. I am inexpressibly grateful for their patience with and their faith in me.

This work was supported by the German National Academic Foundation and the Research Foundation of the State University of New York.

Chapter 1

Introduction

The rapidly growing field of *atom optics* combines the manipulation of internal atomic states with the controlled alteration of the translational motion of atoms. In a lot of cases, atom optics reverses the roles of matter and light as known from conventional optics by realizing atom optical elements such as mirrors, lenses, beamsplitters, etc. with specifically arranged laser beams [6], taking advantage of the forces associated with atom-photon interactions. Lenses and mirrors based on the interaction of atoms with inhomogeneous electrostatic [1] or magnetostatic fields present an important exception which will be considered in more detail in the course of this thesis.

Reaching back to Kepler, who proposed an explanation for the orientation of comet tails away from the sun based on the idea that light carries momentum, Newtonian atom optics describes atoms as point particles, whose trajectories are subject to Newtonian mechanics. This view provides an analogy to the simplifications made in classical optics, as long as effects of gravity, which are naturally absent in classical optics, and dissipative processes, which

are necessary for laser cooling [7], are excluded.

Numerous experiments have been inspired and explained by the classical view of the interaction between atoms and light. Due to advances in both theory and technology, however, experiments that require a quantum mechanical description of this interaction have become possible. The starting point for this development was a paper published by Louis de Broglie in 1923 [8], in which he proposed that all massive particles should exhibit wave-like properties that can be expressed in what is today known as the de Broglie wavelength

$$\lambda_{dB} = \frac{h}{Mv} \tag{1.1}$$

where M and v are the mass and the velocity of the particle, respectively, and h is Planck's constant. Davisson and Germer confirmed Equation (1.1) experimentally for electrons [9], before Stern demonstrated the deflection and diffraction of atoms from metal and crystal surfaces [10]. The first measurement of the deflection of atoms due to absorption and subsequent spontaneous emission of light dates back to Frisch [11], but it was not until the 1980s that Bragg diffraction by optical gratings was experimentally observed [12].

The main problem in the development of early wave atom optics was the fact that effects on the order of the de Broglie wavelength of thermal atoms are extremely small ($\sim 10^{-10}$ m at room temperature) due to the $\frac{1}{\sqrt{T}}$-dependence of λ_{dB} and therefore exceedingly difficult to resolve experimentally [13]. Cooling atoms with laser light as first proposed by Hänsch and Schawlow [14] and Wineland and Dehmelt [15] made atomic samples at temperatures on the or-

der of μK readily available, resulting in atomic de Broglie wavelengths in the range of μm or even longer. Following the advances in laser cooling, the first experimental realization of Bose-Einstein condensation (BEC) [16; 17], which was independently achieved by two groups in 1995 [18; 19], pioneered a new class of high resolution atom optical experiments which took advantage of the ultra-low temperature, the high density and the well-defined quantum state of a BEC (see for example [20; 21; 22; 23]).

However, the translational motion of atoms cannot exclusively be manipulated with light. A different scheme proposed by Breeden and Metcalf in 1981 [1] exploits the comparably strong interaction between highly excited atoms and inhomogeneous electric fields. Whereas neutral ground state atoms do not strongly interact with external electric fields $\mathbf{E}$, because their dipole moment $\mathbf{P} = \alpha\mathbf{E}$ is extraordinarily small for applicable laboratory fields as a result of their very small polarizability α ($\sim 10^{-50}\,\mathrm{Fm}^2$ [24]), the polarizability of Rydberg atoms (see Chapter 2) scales with the principal quantum number as n^7 (see Table 2.1) so that the dipole interaction becomes significantly stronger even for moderate electric fields. Based on this interaction, atom optical elements such as a normal-incidence electrostatic Rydberg atom mirror [25] can be designed.

In the experiment described in this thesis, an electrostatic hexapole lens, whose magnetic counterpart was employed sucessfully to increase the flux of an atomic beam [26], was used to focus a beam of coherently excited Rydberg

helium atoms. In order to elucidate why Rydberg atoms are an indispensable prerequisite for this experiment, the theory of Rydberg atoms, their extraordinary properties, and their behavior in external electric fields will be described in Chapter 2. The high excitation efficiency of the counter-intuitive Stimulated Raman Adiabatic Passage (STIRAP) technique used in the experiment motivates a detailed discussion of the theory of coherent excitation along with remarks on experimental limitations of STIRAP given in Chapter 3, which is followed by a review of the basics of focusing neutral atoms in Chapter 4. Since our experiments are carried out with helium, Chapter 5 provides a short discussion of the energy level structure of helium and the actual excitation scheme used in the experiment. Chapter 6 gives a detailed description of our vacuum system and the available detection systems, before the laser systems and their stabilization schemes are discussed in Chapter 7. The results of our measurements on the Stark energy level structure of helium (Stark map), the relative excitation efficiency of STIRAP compared to the intuitive two-photon transition and the Autler-Townes effect as well as the first results of the successful application of the hexapole lens will be presented in Chapter 8. Finally, Chapter 9 will give a brief summary of our experimental work along with prospective improvements and future plans.

Chapter 2

Rydberg Atoms

2.1 Introduction

Atoms in electronic states of high principal quantum number n are called Rydberg atoms in honor of swedish physicist Johannes R. Rydberg (1854 – 1919). After an initial period of fundamental research, interest was rekindled in the 1970s when new technologies became available, Rydberg atoms are commonly used today in many diverse experiments that take advantage of their unique properties, such as their large orbital radii (scaling with the principal quantum number as n^2), their huge polarizability ($\propto n^7$), and their long radiative lifetimes ($\propto n^3$, see also Table 2.1). Thus, atomic properties that are not accessible in experiments carried out with ground state atoms can be observed experimentally. Furthermore, experimental tests of fundamental concepts and theories become possible. One example is the research field of Cavity Quantum Electrodynamics (CQED), where the interaction of an atom with the structured vacuum produced by a resonant cavity as well as other quantum

mechanical phenomena, e. g. entanglement, can be studied using Rydberg atoms [27].

In this experiment, another interesting feature of Rydberg atoms is exploited: Due to their huge polarizability, Rydberg atoms strongly interact with external fields. Therefore, they cannot only serve as sensitive field probes which allow an experimental resolution of extremely small perturbations, but they also facilitate the atom optical manipulations described in Chapter 4.

The remainder of this chapter will first briefly review the general properties of Rydberg atoms. After a quantum mechanical derivation of their wavefunctions, the effect of external electric fields and the transition strengths and lifetimes will be discussed. A more comprehensive review on Rydberg atoms can be found in [27].

2.2 General Properties of Rydberg Atoms

The first signatures of Rydberg atoms made an appearance in atomic spectroscopy in 1885, when Balmer found that the wavelengths of the four visible spectral lines of atomic hydrogen can be expressed by [27]

$$\lambda = \frac{bn^2}{n^2 - 4} \tag{2.1}$$

where $n = 3, 4, ...$ and $b = 3645.6$ Å. As had been realized by Hartley [28], the significance of Balmer's formula becomes more obvious if Equation (2.1) is rewritten in terms of the wavenumber, which is the inverse of the wavelength

in vacuum, rather than the wavelength [27]

$$\overline{\nu} = \left(\frac{1}{4b}\right)\left(\frac{1}{4} - \frac{1}{n^2}\right) \tag{2.2}$$

This form of Balmer's formula shows that the wavenumber of a transition is directly linked to an electronic transition from states with higher principal quantum number n to the state with $n = 2$. Quite naturally, this description includes Rydberg atoms for which $n \gg 2$.

Classifying the spectra of mostly alkali atoms into sharp (s), principal (p), and diffuse (d) series – a terminology that is still used today to label the electron orbits with angular quantum number $l = 0, 1, 2$ – it was Rydberg [29] who noticed that the wavenumbers of the different series are related and can be described by a single formula [30]

$$\overline{\nu}_l = \overline{\nu}_{\infty l} - \frac{R_y}{(n - \delta_l)^2} \quad \text{for} \quad \mathrm{l} = \mathrm{s}, \mathrm{p}, \mathrm{d} \tag{2.3}$$

where the constants $\overline{\nu}_{\infty l}$ and δ_l are the series limit and the quantum defect, respectively. Rydberg's second major achievement was to realize that the Rydberg constant R_y in (2.3) is a universal constant for all atoms [27]. Moreover, he found an expression for the wavenumbers of the lines connecting different series, for example, s and p series [29]

$$\pm\overline{\nu} = R_y \left[\frac{1}{(m - \delta_s)^2} - \frac{1}{(n - \delta_p)^2}\right] \tag{2.4}$$

where the $(+)$ sign and n represent a sharp series, while the $(-)$ sign and m describe a principal series. The generalized form of Equations (2.2) and (2.4)

$$\overline{\nu}\,(n, n') = R_y \left[\frac{1}{(n' - \delta_{l'})^2} - \frac{1}{(n - \delta_n)^2}\right] \tag{2.5}$$

is known as Rydberg formula, which for $\delta_{l'} = \delta_l = 0$ and $n' = 2$ becomes the familiar Balmer formula for atomic hydrogen.

The model proposed by Bohr in 1913 for the hydrogen atom essentially contains all the interesting features of Rydberg atoms. The Bohr model assumes that an electron with charge $-e$ and mass m_e in the field of a positive charge Ze with infinite mass will follow Newtonian mechanics and move in a circular orbit around the positive charge. The orbital radius r can be derived under the assumption that the angular momentum of the electron is quantized in integral multiples of Planck's constant divided by 2π. With $m_e v r = n\hbar$ [27]

$$r = \frac{\hbar^2 n^2}{Ze^2 m_e k} \tag{2.6}$$

where $k = 1/4\pi\varepsilon_o$, and ε_o is the permittivity of free space. Adding the kinetic and potential energy and inserting (2.6), the total energy E_n of a state n becomes [27]

$$E_n = -\frac{k^2 Z^2 e^4 m_e}{2n^2\hbar^2} = -\frac{m_e c^2 \alpha^2 Z^2}{2n^2} \tag{2.7}$$

where α and c are the fine structure constant and the speed of light, respectively. The negative binding energy shows that the electron is bound to the nucleus. Assuming that, as experimental observations had suggested, the electron will only undergo transitions at a frequency corresponding to the energy separation of two distinct states divided by Planck's constant, Bohr was able to derive the Rydberg formula with his model. Comparing Equation (2.5) and the subtraction of the energies of two different states as given by (2.7), the originally purely experimentally determined Rydberg constant R_y can be

related to atomic properties [27]

$$R_y = \frac{k^2 e^4 m_e}{2\hbar^2} = \frac{m_e c^2 \alpha^2}{2} \tag{2.8}$$

However, this expression is only valid for a nucleus of infinite mass. The effects of nuclear motion can be implemented, if the electron mass m_e in (2.8) is replaced by an effective mass $\mu = m_e(1 + m_e/M)$. The Rydberg constant R_y for a given atom is therefore dependent on its nuclear mass M.

As can be seen from Equations (2.6) and (2.7), the electron of a Rydberg atom is far away from the ionic core and loosely bound. Consequently, Rydberg atoms are easily ionized even in weak fields. Moreover, since their dipole moments and polarizabilities are enormous (see Table 2.1), they exhibit a strong interaction with external fields (see Section 2.4) and a pronounced van der Waals interaction [30]. In most cases, these properties are already present for relatively low n Rydberg states. Considering, for example, the orbital radius which scales as n^2, a hydrogen atom with $n = 10$ has an orbital radius of 100 a_0 where $a_0 = 5.29 \times 10^{-11}$ m is the orbital radius for $n = 1$, the so-called Bohr radius. In contrast, the binding energy ($\propto n^{-2}$) of the same atom is a hundred times smaller than the the binding energy of a ground state atom and already comparable to thermal energies [27].

The three basic mechanisms to create Rydberg atoms [27] are charge exchange, where a positive ion collides with a ground state atom and excites it to a Rydberg state, electron impact, where the excitation is achieved through an electron bombardement of ground state atoms, and optical excitation. The latter has the big advantage of being state selective, because the frequency of

the exciting laser can be tuned to be resonant with a specific Rydberg state.

For non-hydrogenic atoms, the theory presented in this chapter is still valid if the principal quantum number n is replaced by an effective quantum number $n^* = n - \delta_l$ where the quantum defect δ_l (see Section 2.3.2) accounts for the deviations of the ionic core from a pure hydrogenic core that arise from an imperfect shielding of the positive nucleus by the additional core electrons. Table 2.1 shows the scaling properties of Rydberg atoms with respect to their effective quantum number.

Property	Formula	n^{*x}
Binding energy	$E_n = -R_y/(n-\delta_l)^2$	n^{*-2}
Energy difference	$E_n - E_{n-1}$	n^{*-3}
Orbital radius $\langle r \rangle$	$\sim \frac{1}{2}[3(n-\delta_l)^2 - l(l+1)]$	n^{*2}
Geometric cross section	$\pi \langle r \rangle^2$	n^{*4}
Dipole moment	$\langle n, l \left\vert er \right\vert n, l+1 \rangle$	n^{*2}
Polarizability	$2e^2 \sum_{n \neq n'} \frac{\vert\langle nlm\vert z\vert n'l'm'\rangle\vert^2}{E_{nlm} - E_{n'l'm'}}$	n^{*7}
Radiative lifetime	$\left(\frac{e^2}{3\hbar c^3 \pi \varepsilon_0} \sum_{n<n'}^{l=l'\pm 1} \frac{l_{\max}}{2l'+1} \omega^3 \vert\langle n'l' \left\vert r \right\vert nl\rangle\vert^2\right)^{-1}$	n^{*3}
Fine structure		n^{*-3}

Table 2.1 Scaling properties of Rydberg atoms [30; 27]

2.3 Wavefunctions

In order to describe Rydberg atoms and especially their behavior in external fields in a more profound way, a quantum mechanical treatment is indispensable. Before quantum defect theory is introduced to obtain wavefunctions for any single valence electron Rydberg atom, the hydrogen atom as an important special case with well-known analytical solutions will be reviewed. Unless mentioned otherwise, atomic units as defined in Appendix A will be used from now on.

2.3.1 Hydrogen Atom

The Schrödinger equation for the hydrogen atom is given by [31]

$$\left(-\frac{\nabla^2}{2}-\frac{1}{r}\right)\Psi\left(\mathbf{r}\right)=E\Psi\left(\mathbf{r}\right) \tag{2.9}$$

and can be analytically solved. Whereas solving this equation in parabolic coordinates will turn out to be very useful when dealing with external fields (see Section 2.4), a more convenient solution is possible in spherical polar coordinates where ∇^2 becomes [31]

$$\nabla^2=\frac{\partial^2}{\partial r^2}+\frac{2}{r}\frac{\partial}{\partial r}+\frac{1}{r^2\sin\theta}\frac{\partial}{\partial\theta}\left(\sin\theta\frac{\partial}{\partial\theta}\right)+\frac{1}{r^2\sin^2\theta}\frac{\partial^2}{\partial\phi^2} \tag{2.10}$$

Writing the wavefunction $\Psi\left(\mathbf{r}\right)$ as a product of radial and angular functions

$$\Psi\left(\mathbf{r}\right)=Y\left(\theta,\phi\right)R\left(r\right) \tag{2.11}$$

the Schrödinger equation can be separated into an angular and radial part. The angular equation requires $\lambda=l\left(l+1\right)$ for the separation constant λ with

l being a non-negative integer. In this case, the $2l+1$ solutions of the angular part are the normalized spherical harmonics [31]

$$Y_{lm}(\theta,\phi) = \sqrt{\frac{(l-m)!}{(l+m)!}\frac{2l+1}{4\pi}} P_l^m(\cos\theta)\, e^{im\phi} \tag{2.12}$$

where $P_l^m(\cos\theta)$ are the unnormalized associated Legendre functions and m can assume all integral values between $-l$ and l. Defining $\rho(r) = rR(r)$, the radial equation may be written as [27]

$$\frac{\partial^2}{\partial r^2}\rho(r) + \left[2E + \frac{2}{r} - \frac{l(l+1)}{r^2}\right]\rho(r) = 0 \tag{2.13}$$

The normalized solutions of the radial part can be expressed in terms of the associated Laguerre polynomials L_{n+l}^{2l+1} [31]

$$\rho(r,n,l) \equiv rR_{nl}(r) = -\frac{\sqrt{(n-l-1)!}}{(n+l)!^{3/2}\sqrt{2n}}\left(\frac{2}{n}\right)^{l+3/2} e^{-\frac{r}{n}} r^{l+1} L_{n+l}^{2l+1}\left(\frac{2r}{n}\right) \tag{2.14}$$

Reinserting the solution given by (2.14) into (2.13) yields the energy eigenvalues [31]

$$E_n = -\frac{R_y}{n^2} \tag{2.15}$$

This result (compare Equation (2.7) for SI units) shows that the energy is only dependent on the principal qunatum number n, but independent of the other quantum numbers l and m. Whereas the independence of m holds for all atoms because it arises from the fact that there is no preferred direction in space in the absence of external fields (directional degeneracy), the degeneracy in l does only occur for the hydrogen atom as a direct consequence of the exact Coulomb potential $\frac{1}{r}$. For non-hydrogenic atoms, the theory of quantum defect [32] has to be introduced.

2.3.2 Non-hydrogenic Atoms - Quantum Defect

For atoms other than hydrogen, the Schrödinger equation is no longer separable, because the Rydberg electron does not just interact with the nucleus, but also with the other electrons (usually termed core electrons). In high angular momentum Rydberg states, the excited electron is most likely found far away from the ionic core which is seen as a point charge by the Rydberg electron due to the screening of the core charge by the core electrons. For low l states, however, the finite size of the core comes into play, and the electron can both penetrate and polarize the core resulting in a depression of the energy levels of the low angular momentum states with respect to their hydrogenic counterparts. The energy shifts for non-penetrating orbits are similar, but smaller. In general, Equation (2.15) has to be modified for non-hydrogenic atoms [32]

$$E_n = -\frac{R_y}{(n-\delta_l)^2} \tag{2.16}$$

where δ_l is the so-called quantum defect [32]. δ_l decreases rapidly for increasing angular quantum number l and generally also depends on the principal quantum number n. The Rydberg-Ritz formula for the quantum defect is given by [33]

$$\delta_l = a + \frac{b}{(n-a)^2} + \frac{c}{(n-a)^4} + \frac{d}{(n-a)^6} + \dots \tag{2.17}$$

where $a, b, c, d, \dots$ are the empirically obtained Rydberg-Ritz coefficients for the calculation of the quantum defect with a being the limit value of the quantum defect for high series members. The Rydberg-Ritz coefficients for helium are listed in Table 2.2 [34]. Considering the deviation of the non-

$l-value$	a	b	c	d
0	0.296609	-0.038840	0.004960	0.000000
1	0.068320	0.017870	-0.017190	0.000000
2	0.002869	0.006220	0.000000	0.000000
3	0.000240	-0.002090	0.000000	0.000000

Table 2.2 Rydberg-Ritz coefficients for the calculation of the quantum defect of triplet helium atoms [34].

hydrogenic energy levels from their hydrogenic counterparts

$$\Delta E(\delta) = -R_y \left[\frac{1}{n^{*2}} - \frac{1}{n^2}\right] \approx -R_y \frac{\delta}{n^3} \tag{2.18}$$

it is obvious that the precision to which the quantum defect is known determines the precision of the energy level calculations.

In general, the potential of a non-hydrogenic atom can be written as $-\frac{1}{r} + V_d(r)$, where $V_d(r)$ accounts for the deviations from the pure Coulomb potential and can include the atomic fine structure as well as core-polarization effects. Since $V_d(r)$ vanishes for large r, in many practical cases, a good approximation for the wavefunction of the valence electron far from the core can be obtained by using the hydrogenic wavefunctions in a perturbative approach. However, there are many different variation and perturbation methods tailored for specific problems so that the choice of approximation strongly varies under different circumstances, depending, for example, on whether accurate energy eigenvalues or comparably simple wavefunctions shall be obtained [31]. Moreover, approximation results are usually also critically dependent on the

quantum numbers n and l, and an approximation such as the unsymmetric perturbation theory proposed by Heisenberg for atomic helium with one electron in a fairly excited state will give satisfactory results for $l \geq 1$, but fail for states with $l = 0$ [31].

An extensive review of quantum defect theory is given in [32], whereas a specific treatment of all kinds of approximation methods for the helium atom can be found in [31].

2.4 Stark Effect

The effect of external electric fields on highly excited atoms, the so-called Stark effect, is of considerable importance for understanding the behavior of Rydberg atoms. Since the binding energy decreases with the principal quantum number as n^{-2}, whereas the coupling of the electron with an external electric field scales with the dipole moment ($\propto n^2$, see Table 2.1), the Stark shift even for moderate electric fields can dominate the energy level structure of the atom [35]. Therefore, the dependence of the energy levels on the applied electric field, whose graphical plot is known as Stark map, will be discussed in this chapter. After the Stark structure of the hydrogen atom has been derived, helium will serve as an example of how the deviations from a pure Coulomb potential cause a significantly different result.

2.4.1 Hydrogen

Neglecting the spin of both electron and nucleus, the Schrödinger equation for the hydrogen atom in a static electric field is given by [35]

$$\left(-\frac{1}{2}\nabla^2 - \frac{1}{r} + H_F\right)\Psi(\mathbf{r}) = E\Psi(\mathbf{r}) \tag{2.19}$$

The Hamiltonian H_F for the interaction of the atom with the applied electric field can be simplified if the field is taken to lie along the z-axis

$$H_F = -\mathbf{P}\cdot\mathbf{E} = E_z z \tag{2.20}$$

where $\mathbf{P}$ and E_z are the electric-dipole operator and the magnitude of the electric field, respectively. Symmetry considerations yield that the expectation value of the perturbation potential H_F vanishes when the field-free eigenfunctions of (2.19) are used [31], because they have definite parity, whereas H_F changes sign under inversion ($z \to -z$). Therefore, the lowest order Stark shift is quadratic in general. However, the degeneracy with respect to l makes the hydrogen atom an exception showing a linear dependence on the field.

For a quantitative treatment of the Stark effect, one can take advantage of the fact that Equation (2.19) is separable in parabolic coordinates ξ, η, φ defined by [31]

$$\begin{aligned} \xi &= r + z, \\ \eta &= r - z, \\ \varphi &= \arctan\left(\frac{y}{x}\right) \end{aligned} \tag{2.21}$$

With (2.21) ∇^2 becomes [31]

$$\nabla^2 = \frac{4}{\xi+\eta}\frac{d}{d\xi}\left(\xi\frac{d}{d\xi}\right) + \frac{4}{\xi+\eta}\frac{d}{d\eta}\left(\eta\frac{d}{d\eta}\right) + \frac{1}{\xi\eta}\frac{d^2}{d\varphi^2} \tag{2.22}$$

Assuming that a solution of Equation (2.19) is given by [31]

$$\Psi(\xi,\eta,\varphi) = \Phi_1(\xi)\,\Phi_2(\eta)\,e^{\pm im\varphi} \tag{2.23}$$

where m is an integer or zero and Z_1 and Z_2 are separation constants related by $Z_1 + Z_2 = 1$, the Schrödinger equation can be separated into two ordinary differential equations for $\Phi_1(\xi)$ and $\Phi_2(\eta)$ [31]

$$\begin{aligned}
\frac{d}{d\xi}\left(\xi\frac{d\Phi_1}{d\xi}\right) + \left(\frac{1}{2}E\xi + Z_1 - \frac{m^2}{4\xi} - \frac{1}{4}E_z\xi^2\right)\Phi_1 &= 0, \\
\frac{d}{d\eta}\left(\eta\frac{d\Phi_2}{d\eta}\right) + \left(\frac{1}{2}E\eta + Z_2 - \frac{m^2}{4\eta} + \frac{1}{4}E_z\eta^2\right)\Phi_2 &= 0,
\end{aligned} \tag{2.24}$$

Z_1 and Z_2 effectively act as positive charges binding the electron in the ξ and η coordinates. Although (2.24) can be directly integrated, the usual way to obtain the hydrogenic energy levels in the presence of a weak electric field is to determine the zero-field wavefunctions in parabolic coordinates and then treat the field as a perturbation [27]. The unperturbed eigenfunctions are given by [31]

$$\begin{aligned}
\Phi_1(\xi) &= \frac{\sqrt{n_1!}}{(n_1+m)!^{3/2}} e^{-\frac{1}{2}\varepsilon\xi}\xi^{\frac{1}{2}m}\varepsilon^{\frac{1}{2}(m+1)} L^m_{n_1+m}(\varepsilon\xi), \\
\Phi_2(\eta) &= \frac{\sqrt{n_2!}}{(n_2+m)!^{3/2}} e^{-\frac{1}{2}\varepsilon\eta}\eta^{\frac{1}{2}m}\varepsilon^{\frac{1}{2}(m+1)} L^m_{n_2+m}(\varepsilon\eta),
\end{aligned} \tag{2.25}$$

where $\varepsilon = \sqrt{-2E}$ and $L^m_{n_i+m}(x)$ are the Laguerre functions with $x = \varepsilon\xi$ or $x = \varepsilon\eta$ and $i = 1, 2$ [31]. The parabolic quantum numbers n_i are nonnegative integers representing the number of nodes in the wavefunctions given by (2.25).

They are related to the effective charges Z_i by

$$n_i = Z_i n - (m+1)/2 \tag{2.26}$$

and to the quantum numbers $n, |m|$ through

$$n = n_1 + n_2 + |m| + 1 \tag{2.27}$$

The perturbative treatment of the electric field differs from the usual approach in that the separation parameters Z_i instead of the energy E are the eigenvalues of the problem. The zeroth order ($E_z = 0$) eigenvalue is given by [31]

$$Z_i^{(0)} = \left(n_i + \frac{m+1}{2}\right)\varepsilon \tag{2.28}$$

The expectation value of the perturbation potential H_F with the unperturbed eigenfunctions given by (2.25) yields the first order eigenvalue $Z_i^{(1)}$ produced by the field $E_z \neq 0$

$$Z_i^{(1)} = \pm\frac{1}{4}E_z\varepsilon^{-2}\left(6n_i^2 + 6n_i m + m^2 + 6n_1 + 3m + 2\right) \tag{2.29}$$

where the signs + and − apply for $i = 1, 2$, respectively. Recalling $Z_1 + Z_2 = 1$, the total energy including the first order perturbation becomes [31]

$$E = -\frac{1}{2}\varepsilon^2 = -\frac{1}{2n^2} + \frac{3}{2}E_z n\left(n_1 - n_2\right) \tag{2.30}$$

which is linearly dependent on the external field E_z, the principal quantum number n and the term $(n_1 - n_2)$ which is often referred to as "electric quantum number". Although transitions involving a change of sign in this electric quantum number are weak in most cases, there are no selection rules for n_1, n_2

[31]. Note that due to (2.27), the first order energy implicitly depends on the magnetic quantum number m [27].

The energy separation between the energetically highest and lowest Stark component of the same principal quantum number n is given by

$$\Delta E = 3E_z n\,(n-1) \tag{2.31}$$

For higher electric fields, the next order of perturbation theory becomes relevant resulting both in a quadratic field dependence of the energy and a mixing of energy levels with different principal quantum number n. The total energy in second order approximation is given by [31]

$$\begin{aligned} E &= E^{(0)} + E^{(1)} + E^{(2)} \\ &= -\frac{1}{2n^2} + \frac{3}{2}E_z n\,(n_1 - n_2) \\ &\quad -\frac{1}{16}E_z^2 n^4 \left[17n^2 - 3\,(n_1 - n_2)^2 - 9m^2 + 19\right] \end{aligned} \tag{2.32}$$

In contrast to the linear Stark effect, the quadratic term explicitly depends on the magnetic quantum number m. Furthermore, it can be shown that the quadratic Stark effect always leads to a depression of the energy levels.

Although the Stark energy levels can be calculated to arbitrarily high order [36], second order approximations are sufficient in most cases. For hydrogen, the Stark shift can be considered linear in the electric field until field ionization occurs [37]. However, precision measurements [38] require higher orders of perturbation theory for a satisfactory agreement of experiment and theory.

2.4.2 Helium

Although helium has the simplest atomic structure apart from hydrogen and thus exhibits a considerable resemblance to it [39], the Schrödinger equation for He is no longer separable due to the finite size of the ionic core so that analytic solutions do not exist. However, highly accurate calculations are available [40].

One of the most striking differences compared to the hydrogenic case is that for weak fields, the lowest order Stark effect for helium is quadratic in the intensity of the electric field. In order to obtain the dependence of the He energy levels on an external electric field, the Hamiltonian

$$H = H_0 + H_F + H_{fs} \tag{2.33}$$

has to be diagonalized. Here, $H_0 = -\frac{\nabla^2}{2} + V(r)$ and H_{fs} are the Hamiltonians of the unperturbed system and the fine structure, respectively, and H_F is given by Equation (2.20). The fine structure term matters for heavier atoms [35] and can be neglected for helium (see Figure 2.1 and Figure 2.2). Since perturbation theory is fundamentally inapplicable to any potential $V(r)$ deviating from the pure Coulombic case [35], precise approximations have to be used. The method proposed by Zimmerman *et al.* [35] relies on the Coulomb approximation [41] which takes the potential to be essentially Coulombic outside the core and makes it possible to find zero-field wavefunctions. Deviations from the pure Coulomb potential introduced by core polarization ($\propto r^{-4}$) and fine structure ($\propto r^{-3}$) can then be treated by means of perturbation theory [35].

For the diagonalization of the complete Hamiltonian H in the presence of the electric field, the most suitable basis of zero-field helium wavefunctions is

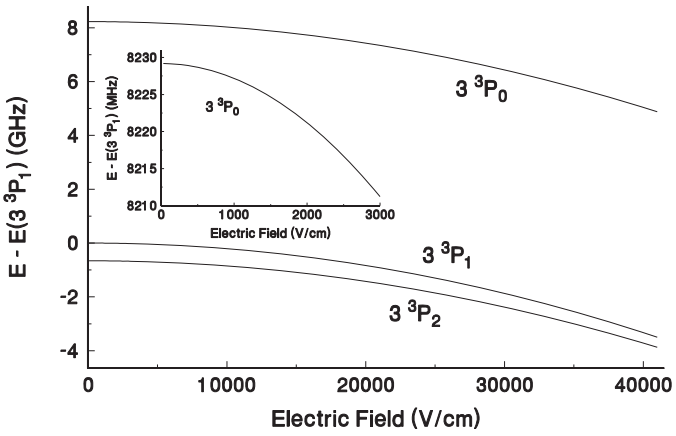

Figure 2.1 Dependence of the $3\,^3\mathrm{P}_J$ states of He on the strength of an applied external electric field [34]

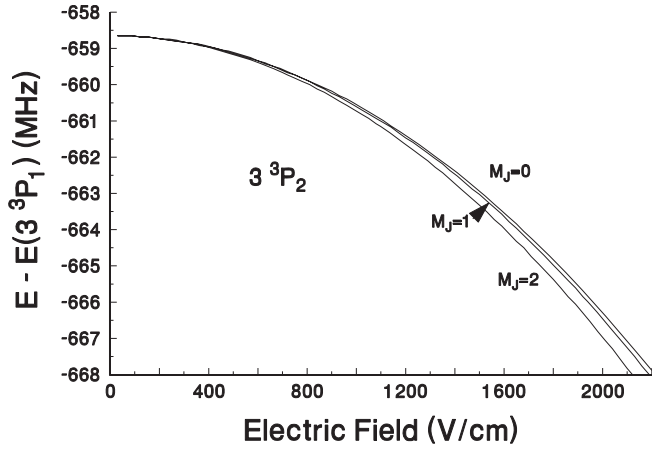

Figure 2.2 Electric field dependence of the sublevels of the $3\,^3\mathrm{P}_2$ state of He [34]

the spherical representation $|nlm\rangle$, because neither the unperturbed energies nor the Stark effect are diagonal in the parabolic basis that proved to be useful for hydrogen (see Section 2.4.1) so that most of the advantage of using the parabolic basis is lost [39]. The diagonal elements of the Hamiltonian matrix are the zero-field energies given by (2.16) that can be calculated if the quantum defects are known [34; 42], whereas the off-diagonal elements [35]

$$\langle n'l'm'\,|E_z z|\,nlm\rangle = \delta_{m,m'}\delta_{l,l\pm1}E_z\,\langle l'm'\,|\cos\theta|\,lm\rangle\,\langle n'l'\,|r|\,nl\rangle \tag{2.34}$$

contain the electric field contribution. Here, $\delta_{i,j}$ is the usual Kronecker delta. The angular matrix elements in Equation (2.34) can be evaluated analytically exploiting the properties of the spherical harmonics and become [35]

$$\begin{aligned}\langle l,m'\,|\cos\theta|\,l-1,m\rangle &= \sqrt{\frac{l^2-m'^{\,2}}{(2l+1)\,(2l-1)}}\\ \langle l,m'\,|\cos\theta|\,l+1,m\rangle &= \sqrt{\frac{(l+1)^2-m'^{\,2}}{(2l+3)\,(2l+1)}}\end{aligned} \tag{2.35}$$

The remaining radial matrix elements $\langle n'l'\,|r|\,nl\rangle$ pose the main computational challenge and are most satisfactorily calculated via numerical integration employing a Numerov algorithm with logarithmic scaling variables [35]. Once all matrix elements have been determined, the Hamiltonian matrix can be diagonalized.

The graphical plot of the energy levels as a function of field strength, the so-called Stark map, illustrates the differences to the hydrogenic case. A Stark map for the $n = 26$ state of triplet helium is shown for $m = 0$ in Figure 2.3.

The first remarkable feature is that the degeneracy with respect to l at zero-field is broken and the low l energy levels are depressed as a result of their

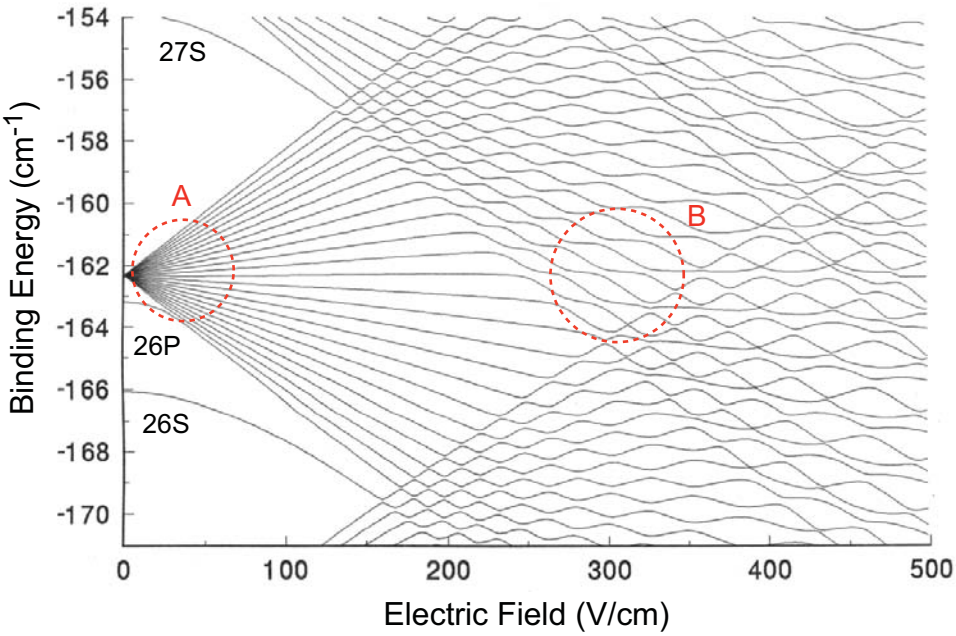

Figure 2.3 Stark map for triplet He in the energy range of the n=26 states [34]. The electric field lifts the zero-field degeneracy of the n=26 manifold (A). Levels of different n show avoided crossings (B).

non-vanishing quantum defects. For the states with higher l (here $l > 1$) which are essentially degenerate at zero-field, the external field lifts the degeneracy resulting in a manifold of energy levels (denoted by **A** in Figure 2.3).

Another phenomenon typical of non-hydrogenic atoms is depicted in region **B** of Figure 2.3: Stark states of different principal quantum number n that approach each other for increasing field strength do not cross, but exhibit distinct anti-crossings. These avoided level crossings originate from the finite core size which breaks the dynamical symmetry of the Coulomb potential [35]. Although there is no selection rule for n, manifolds of different n are

not completely independent because of a small dipole coupling between levels of adjacent n. The number of n-levels required for an accurate calculation increases with field strength [39]. As the crossings observed for levels with identical m are a unique feature of the non-relativistic hydrogen atom, the level separation at an anti-crossing is a sensitive function of the quantum defect, and therefore avoided level crossings provide a meaningful test for the accuracy of calculations [35].

2.5 Oscillator Strengths and Lifetimes

The strength of a transition from an initial state $|nlm\rangle$ to a final state $|n'l'm'\rangle$ can be expressed in terms of the so-called oscillator strength, a dimensionless quantity given by [31; 27]

$$f_{n'l'm',nlm} = 2\frac{m_e}{\hbar}\omega_{n'l',nl}\left|\langle n'l'm'\left|z\right|nlm\rangle\right|^2 \tag{2.36}$$

where $\omega_{n'l',nl} = (E_{n'l'} - E_{nl})/\hbar$ is the angular transition frequency. For any atom or molecule, with or without external fields, and for any polarization direction, the Thomas-Reiche-Kuhn sum rule holds for the oscillator strengths for all transitions from a specific state $|nlm\rangle$ [31]. Hence

$$\sum_{n'l'm'} f_{n'l'm',nlm} = Z \tag{2.37}$$

with Z being the total number of electrons in the system. According to the definition given in (2.36), the oscillator strength depends on the magnetic quantum number m. As there is no preferred direction in free space, the radiative decay of an atom cannot depend on m [27]. Therefore, an average

oscillator strength for transitions $|nl\rangle \rightarrow |n'l'\rangle$ which is independent of polarization and m is defined by [31; 27; 43]

$$\bar{f}_{n'l',nl} = \frac{2}{3}\frac{m_e}{\hbar}\omega_{n'l',nl}\frac{l_{\max}}{2l+1}\left|\langle n'l'\left|r\right|nl\rangle\right|^2 \tag{2.38}$$

where $l_{\max}$ is the larger of l and l' and $2l+1$ is the degree of degeneracy of the initial state. Exchanging initial and final state in (2.38) reveals that $\bar{f}_{n'l',nl}$ and $\bar{f}_{nl,n'l'}$ are not equal but obey [31]

$$\bar{f}_{n'l',nl} = -\frac{2l'+1}{2l+1}\bar{f}_{nl,n'l'} \tag{2.39}$$

Stronger sum rules than (2.37) hold for the average oscillator strengths. Summing over all transitions from a certain level $|nl\rangle$ to levels of adjacent orbital quantum numbers $l \pm 1$ yields [31]

$$\begin{aligned}\sum_{n'}\bar{f}_{n'l-1,nl} &= -\frac{1}{3}\frac{l(2l-1)}{2l+1}\\ \sum_{n'}\bar{f}_{n'l+1,nl} &= \frac{1}{3}\frac{(l+1)(2l+3)}{2l+1}\end{aligned} \tag{2.40}$$

Adding these two equations reproduces the sum rule (2.37) for the oscillator strengths $f_{n'l',nl}$. Equation (2.40) shows that emission ($n' < n$) prevails among the transitions $|nl\rangle \rightarrow |n'l-1\rangle$, whereas the transitions $|nl\rangle \rightarrow |n'l+1\rangle$ are predominated by absorption ($n' > n$). Moreover, a change of n and m in the same sense is found to be more probable than a change in opposite sense [31].

For effective focusing (see Chapter 4), it is desirable to use the Stark state with the highest transition probability which can be evaluated from the distribution of the average oscillator strengths of the transitions to a manifold

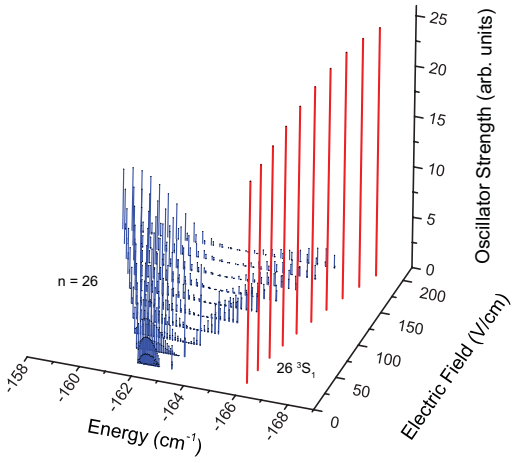

Figure 2.4 Average oscillator strengths for the transitions from the $3\,^3P_2$ state to the $|26l'\rangle$ Rydberg states in triplet He. Data obtained from [34]

of Stark states. A plot of the results of a numerical calculation for the transitions from the $3\,^3P_2$ state to the $|26\ l'\rangle$ Rydberg states is shown in Figure 2.4.

The spontaneous decay rate of a state $|nl\rangle$ to an energetically lower state $|n'l'\rangle$ defined by the Einstein A coefficient can be related to the average oscillator strength by [31; 27]

$$A_{n'l',nl} = -\frac{2e^2\omega^2_{n'l',nl}}{m_e c^3}\bar{f}_{n'l',nl} \tag{2.41}$$

where the minus-sign arises because $\bar{f}_{n'l',nl} < 0$ in that case.

The radiative lifetime τ_{nl} of the state $|n\rangle$ is defined as the inverse of the total spontaneous decay rate which is simply the sum of $A_{n'l',nl}$ over all final states $|n'l'\rangle$. Therefore [27]

$$\tau_{nl} = \left[\sum_{n'l'} A_{n'l',nl}\right]^{-1} \tag{2.42}$$

Equations (2.41) and (2.42) reveal that the transitions with the highest frequencies make the largest contribution to the lifetime. For $n \to \infty$, the highest transition frequencies are basically constant. Therefore, the liftetime of a Rydberg state is determined solely by the transition matrix element resulting in the n^3 dependence listed in Table 2.1. However, the states with $l \approx n$ are an exception and scale as n^5 [27] so that the average lifetime of the n-th state can be estimated by $\bar{\tau}_n \propto n^{4.5}$ [31].

The probability of a state $|nl\rangle$ decaying to a particular state $|n'l'\rangle$ is defined by the branching ratio [44]

$$b_{n'l',nl} = \frac{A_{n'l',nl}}{\sum\limits_{n'l'} A_{n'l',nl}} = \tau_{nl} A_{n'l',nl} \tag{2.43}$$

Chapter 3

Coherent Excitation of Atoms

Experimental frontiers in both atomic physics and physical chemistry as well as the ubiquitous quest for higher resolution in existing experiments aroused an increased interest in suitable methods for selective and efficient population transfer to a particular excited atomic or molecular level. As optical excitation proves to be the most adequate technique in terms of selectivity, the remaining question of how to achieve the maximal excitation efficiency has to be addressed.

Until lasers were available as sources of coherent light, excitation processes were described by radiative rate equations [45]. In the ideal case of a two-level system with the same level degeneracy and initially in its ground state, the differential equations for the changes in populations when exposed to an intense near-resonant radiation field where stimulated emission dominates spontaneous emission lead to an exited state population of

$$P_{ex}(t) = \frac{1}{2}\left\{1 - \exp\left[-B\int_{-\infty}^{t} I(t')dt'\right]\right\} \tag{3.1}$$

where B and I are the Einstein-Milne coefficient for absorption (units of

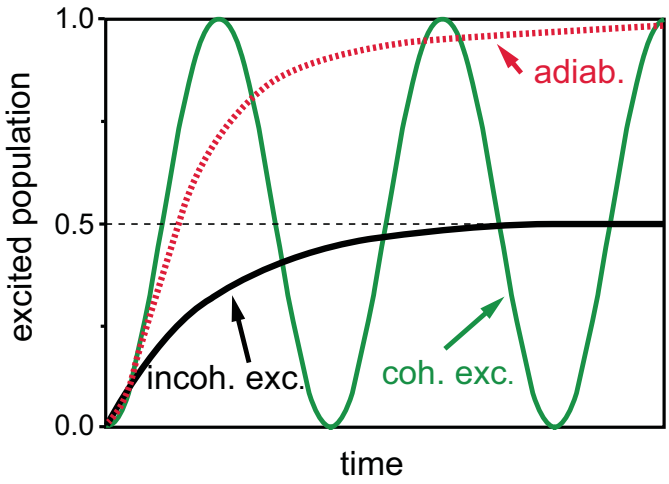

Figure 3.1 Evolution of the excited state population in a two-level system for coherent and incoherent excitation and adiabatic passage [46]

m^2J^{-1}) and the instantaneous radiation intensity (power per unit area), respectively. It is obvious from (3.1) that at most 50% of the population can be transferred to the excited state. For incoherent excitation, this is the saturation limit which can only be reached if the excitation is maintained by radiation (see *incoh. exc.* line in Figure 3.1). In a system with more than two levels, complete population transfer by incoherent excitation is generally possible. The process of optical pumping is one example which, however, even in the ideal case of complete transfer suffers from a lack of selectivity, whereas the gain of selectivity in the process of stimulated emission pumping is vitiated by the low efficiency of maximal 25% [47].

Since a large number of highly excited helium Rydberg atoms is required to get meaningful results from our focusing experiments (see Chapter 4), we take advantage of a coherent process which relies on a counter-intuitive se-

quence of excitations and theoretically allows a transfer efficiency of 100%. The basic theoretical principles of this method were mapped out by Oreg *et al.* [48], whereas the first experimental realization along with an approximate analytical description were achieved in the laboratory of Bergmann [2; 3; 4], which also proposed the name *stimulated Raman adiabatic passage* (STIRAP) for the novel technique [4], because it combines features of stimulated Raman scattering [49; 50] and adiabatic passage [7; 51; 52].

In this chapter, after presenting a brief overview of the different excitation techniques, the theory and experimental implementation of STIRAP will be discussed as well as the Autler-Townes effect which can be readily observed as a byproduct in our experiment.

3.1 Atom-Photon Interaction

Since laser light is primarily used to excite atoms in our experiment, it is instructive to prefix the theory of coherent excitation with a semi-classical description of the interaction between atom and radiation field. For light resonant or nearly resonant with only two atomic levels, the discussion can be simplified to the ideal case of a single quantum mechanical two-level atom interacting with a classical single mode radiation field, for which the Hamiltonian is given by

$$H = H_A + H_I \tag{3.2}$$

where H_A and H_I represent the unperturbed atomic part and the interaction part of the Hamiltonian, respectively. The radiation part has been explicitly

omitted for the sake of simplicity. A description of the atom-photon interaction starting from the total Hamiltonian including the light field will be given in 3.5.1. In Equation (3.2), the unperturbed atomic Hamiltonian can be written as [6; 53]

$$H_A = \frac{\mathbf{p}^2}{2M} + \sum_k E_k \left|k\right\rangle \left\langle k\right| \tag{3.3}$$

with the two terms being the center-of-mass kinetic energy and the internal energy of the atom, respectively. Restricting the discussion to two-level atoms, the set of atomic eigenstates $|k\rangle$ reduces to the ground state $|g\rangle$ and the excited state $|e\rangle$. For optical frequencies, the so-called long-wavelength or *dipole approximation* holds, because optical wavelengths (typically $\sim 10^{-7}$ m) are much bigger than the size of an atom ($\sim 10^{-10}$ m) so that the electromagnetic field can be considered essentially uniform over the size of an atom. Hence, the interaction Hamiltonian becomes

$$H_I = -\mathbf{P} \cdot \mathbf{E}(\mathbf{R}, t) \tag{3.4}$$

Taking advantage of the completeness relation $|g\rangle \langle g| + |e\rangle \langle e| = \mathbb{1}$, the electric dipole moment $\mathbf{P}$ can be expressed as [53]

$$\mathbf{P} = e\mathbf{r} = e\left(\langle e|\,\mathbf{r}\,|g\rangle\,|e\rangle\langle g| + \langle g|\,\mathbf{r}\,|e\rangle\,|g\rangle\langle e|\right) \tag{3.5}$$

For further evaluation of (3.4), it turns out to be useful to switch from cartesian coordinates to a spherical coordinate system in whose unit vectors are connected to the cartesian ones via $\mathbf{e}_0 = \mathbf{e}_z$ and $\mathbf{e}_\pm = \mp\frac{1}{\sqrt{2}}(\mathbf{e}_x \pm i\mathbf{e}_y)$ [54]. In this representation, the general form of a classic electromagnetic field with

frequency ω, amplitude $E_0(\mathbf{R})$, and phase $\phi(\mathbf{R})$ becomes [43; 6]

$$\mathbf{E}(\mathbf{R},t) = \epsilon(\mathbf{R})E_0(\mathbf{R})\cos\left[\omega t + \phi(\mathbf{R})\right] \tag{3.6}$$

where the polarization vector $\epsilon(\mathbf{R})$ takes the simple form $\epsilon(\mathbf{R}) = \mathbf{e}_q(\mathbf{R})$ for pure linearly ($q = 0$) and pure circularly ($q = \pm 1$, usually denoted by $\sigma^{\pm}$) polarized light. In the pure case, (3.4) thus becomes

$$H_I = \hbar\cos(\omega t + \phi)\left(\Omega_q \left|e\right\rangle\left\langle g\right| + \Omega_q^* \left|g\right\rangle\left\langle e\right|\right) \tag{3.7}$$

Here, the coupling between the ground state $|g\rangle$ and the excited state $|e\rangle$ caused by the atom-field interaction is parameterized by the *Rabi frequency* [55; 7; 56; 53]

$$\Omega_q = -\frac{eE_0}{\hbar}\left\langle e\right|\mathbf{e_q}\cdot\mathbf{r}\left|g\right\rangle = -\frac{eE_0}{\hbar}\left\langle e\right|r_q\left|g\right\rangle \tag{3.8}$$

The strength of the coupling depends both on the intensity I of the light via $E_0 = \sqrt{\frac{2I}{\varepsilon_0 c}}$ and the electronic wavefunctions of the atom through the dipole or transition matrix element $\langle e|\, r_q\, |g\rangle$, whose evaluation is greatly facilitated by the Wigner-Eckart theorem [57; 58], which for a tensor of rank 1, that is, a vector like $\mathbf{r}$, and an atom without hyperfine structure like helium reads

$$\begin{aligned}\left\langle e\right|r_q\left|g\right\rangle &= \left\langle n'S'L'J'M_J'\right|r_q\left|nSLJM_J\right\rangle \\ &= (-1)^{J'-M_J'}\begin{pmatrix} J' & 1 & J \\ -M_J' & q & M_J\end{pmatrix}\left\langle n'S'L'J'\right\|r\left\|nSLJ\right\rangle\end{aligned} \tag{3.9}$$

where $(\cdots)$ is a Wigner 3j symbol. The selection rules $\Delta J = J' - J = 0, \pm 1$ for $J + J' \geq 1$ and $\Delta M_J = M_J' - M_J = q$ immediately follow from the properties of the 3j-symbols [56]. All physical information is contained in the reduced

matrix element $\langle n'S'L'J' \| \, r \, \| nSLJ \rangle$, which can be transformed into a reduced matrix element in L representation via [56; 54]

$$\begin{aligned} \langle n'S'L'J' \| \, r \, \| nSLJ \rangle &= \delta_{S,S'} \, (-1)^{S'+L+J'+1} \sqrt{(2J+1)(2J'+1)} \\ &\times \left\{ \begin{array}{ccc} L' & J' & S' \\ -J & L & 1 \end{array} \right\} \langle n'L' \| \, r \, \| nL \rangle \end{aligned} \tag{3.10}$$

with the Wigner 6j symbol $\{\cdots\}$. The Kronecker delta $\delta_{S,S'}$ in (3.10) gives rise to the selection rule $\Delta S = 0$, which simply states that an electric dipole interaction cannot couple different S-multiplets. With (3.10), Equation (3.9) becomes

$$\begin{aligned} \langle e | \, r_q \, | g \rangle &= (-1)^{2J'+S'+L-M'_J+1} \sqrt{(2J+1)(2J'+1)} \left(\begin{array}{ccc} J' & 1 & J \\ -M'_J & q & M_J \end{array} \right) \\ &\times \left\{ \begin{array}{ccc} L' & J' & S' \\ -J & L & 1 \end{array} \right\} \delta_{S,S'} \, \langle n'L' \| \, r \, \| nL \rangle \end{aligned} \tag{3.11}$$

The explicit evaluation of the 3j and 6j symbols is rather cumbersome, but fortunately there are copious references with tabulated formulae and values (e.g. [56]). In order to calculate the Rabi frequency for a given transition between a lower state $|nL\rangle$ and an upper state $|n'L'\rangle$ and the liftime of the upper state, the fact that [54; 56]

$$\langle n'L' \| \, r \, \| nL \rangle = \sqrt{2L'+1} \left(\frac{3\lambda^3 \Gamma'_n}{32\pi^3 c\alpha} \right)^{1/2} \delta_{L,L'\pm 1} \tag{3.12}$$

relates the decay rate $\Gamma_{n'}$ to the reduced matrix element in L-representation has to be exploited. Here, $\alpha = \frac{1}{4\pi\varepsilon_0} \frac{e^2}{\hbar c}$ and c are the fine structure constant and the speed of light, respectively. Combining Equations (3.8), (3.11), and the

on-resonance saturation parameter s_0 of the transition $|nL\rangle \rightarrow |n'L'\rangle$ defined as [7]

$$s_0 = \frac{I}{I_s} = \frac{2\Omega_q^2}{\Gamma_{n'}^2} \tag{3.13}$$

the saturation intensity I_s of the transition becomes [7]

$$I_s = \frac{\pi hc}{3\lambda^3}\Gamma_{n'} \tag{3.14}$$

3.2 Two-level Atom

In the theory of coherent excitation [59], a system is described by its time dependent state vector $|\Psi(t)\rangle$ expressed in the basis of atomic bare states $|\varphi_n(t)\rangle$

$$|\Psi(t)\rangle = \sum_n C_n(t)\,|\varphi_n(t)\rangle \tag{3.15}$$

where the probability of finding the system in state $|\varphi_n\rangle$ is given by

$$P_n(t) = |\langle\varphi_n|\,\Psi\rangle|^2 = |C_n|^2 \tag{3.16}$$

The state vector $|\Psi(t)\rangle$ obeys the time-dependent Schrödinger equation which can be expressed in terms of the expansion coefficients from (3.15) [47]

$$\frac{d}{dt}C_n(t) = -\frac{i}{\hbar}\sum_m H_{mn}(t)\,C_m(t) \tag{3.17}$$

where the Hamiltonian matrix $H_{mn}(t)$ is explicitly time-dependent due to the electric dipole interaction between atoms and radiation field. The actual appearance of its matrix elements depends on the choice of phases in the state vector expansion (3.15). At this point, it should be noted that any

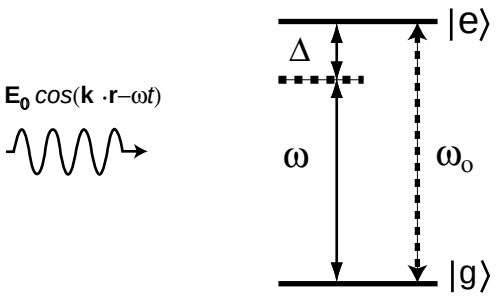

Figure 3.2 Atom-field interaction in a two-level atom. The frequency ω of the incident plane wave is detuned by Δ from the atomic resonance between the excited state $|e\rangle$ and the ground state $|g\rangle$ which is given by the Bohr frequency ω_0

excitation process which is not purely coherent due to irreversible changes such as collisions or spontaneous emission that take atoms out of the system has to be treated by a density matrix formalism [47; 59]. Therefore, the following discussions assume purely coherent radiation fields.

Consider the idealized case depicted in Figure 3.2: A monochromatic plane wave $\mathbf{E}(\mathbf{r},t) = \mathbf{E}_0 \cos(\mathbf{k}\cdot\mathbf{r} - \omega t)$ with frequency ω and amplitude $|\mathbf{E}_0|$ is incident on a single stationary two-level system consisting of ground and excited state $|g\rangle$ and $|e\rangle$ with energies $\hbar\omega_e$ and $\hbar\omega_g$, respectively, whose energy separation is given by the Bohr frequency $\omega_0 = \omega_e - \omega_g$. The Hamiltonian matrix for this atom-field interaction under the rotating wave approximation can be expressed as [47]

$$H = \frac{\hbar}{2}\begin{pmatrix} 0 & \Omega \\ \Omega & 2\Delta \end{pmatrix} \tag{3.18}$$

where the detuning $\Delta = \omega - \omega_0$ is the difference between the frequency of the

incident light and the Bohr frequency, and the atom-field interaction appearing in the off-diagonal elements is parameterized by the Rabi frequency [55]. The rotating wave approximation neglects terms oscillating at 2ω and requires that both the Rabi frequency Ω and the detuning Δ be much smaller than the frequency ω of the radiation. The analytic solution of the time-dependent Schrödinger equation with the Hamiltonian matrix from Equation (3.18) yields [47]

$$P_{ex}(t) = \frac{1}{2}\left(\frac{\Omega}{\Omega_{\text{eff}}}\right)^2 [1 - \cos(\Omega_{\text{eff}} t)] \tag{3.19}$$

for the excitation probability of the excited state. Here, the effective Rabi frequency Ω_{eff} is defined as [47]

$$\Omega_{\text{eff}} \equiv \sqrt{\Omega^2 + \Delta^2} \tag{3.20}$$

If the radiation intensity varies during the excitation process, the substitution $\Omega_{\text{eff}} t \rightarrow A(t) = \int_{-\infty}^{t} \Omega_{\text{eff}}(t')\, dt'$, where $A(t)$ is termed pulse area, becomes necessary.

Equation (3.19) illustrates the striking difference between coherent and incoherent excitation: Whereas suddenly applied incoherent radiation leads to a monotonic approach of the excited state population to its equilibrium value of 50% (see Equation (3.1)), the coherent case is characterized by oscillations in the excited state population, the so-called *Rabi oscillations* [55]. For resonant excitation ($\Delta = 0$), the population transfer will be complete for a so-called π-*pulse*, namely if the pulse area $A(t)$ equals odd multiples of π, while for $A(t) = 2j\pi$ ($j \in \mathbb{N}$) all population will reside in the ground state (see *coh. exc.* line in Figure 3.1). Off resonance ($\Delta \neq 0$), the Rabi oscillations become more

rapid, and the transfer efficiency is always less than 100%.

Experimental reality requires an extension of the previous considerations for single stationary systems to an inhomogeneously broadened ensemble of atoms or molecules. A thermal beam of atoms moving across a laser beam, for example, has a certain velocity distribution so that different velocity groups of atoms will be on resonance with the laser light at different Doppler-shifted frequencies and experience different pulse areas due to their different transit times, let alone fluctuations in laser intensity. To account for these inhomogeneous interactions, the theoretical excitation probabilities have to be averaged resulting in diminished transfer efficiencies that can be as low as 50% [47].

Complete population transfer can also be achieved with a mechanism called *adiabatic rapid passage* (ARP). In contrast to the π-pulse model, where the frequency of the radiation field is kept constant, ARP is based on sweeping the frequency of the external field through a resonance. The somewhat contradictory name of the process originates from the fact, that the frequency chirp has to be sufficiently slow to guarantee adiabatic evolution of the system (therefore, a general rule of thumb for the pulse area is $A(t) \gg 1$), but yet faster than the radiative lifetime of the excited state (sweep time $\Delta\tau \ll \Gamma^{-1}$ with Γ being the decay rate of the excited state).

The discussion of adiabatic time evolution is greatly alleviated through the introduction of the instantaneous eigenstates of the time-dependent Hamilto-

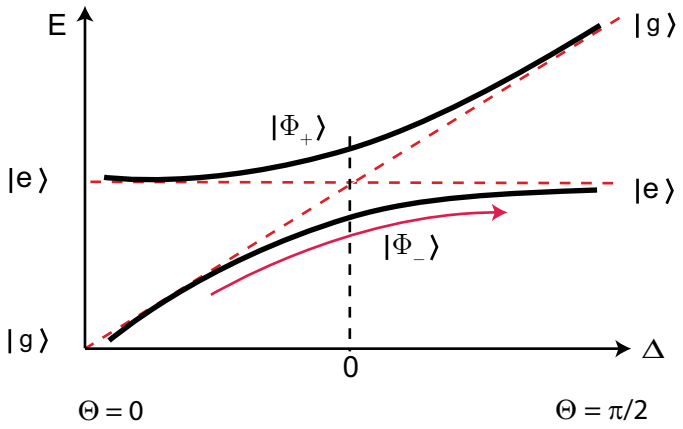

Figure 3.3 Eigenenergies of the adiabatic states as a function of detuning Δ

nian in Equation (3.18) [59; 43]

$$\begin{aligned} |\Phi_+(t)\rangle &= |g\rangle \sin\Theta(t) + |e\rangle \cos\Theta(t) \\ |\Phi_-(t)\rangle &= |g\rangle \cos\Theta(t) - |e\rangle \sin\Theta(t) \end{aligned} \tag{3.21}$$

with the mixing angle $\Theta(t)$ defined as [47]

$$\Theta(t) = \frac{1}{2} \arctan\left(\frac{\Omega(t)}{\Delta(t)}\right) \tag{3.22}$$

The *adiabatic states* $|\Phi_\pm(t)\rangle$ in (3.21) are given as a time-dependent superposition of the unperturbed atomic or *diabatic* states. The two eigenvalues of the Hamiltonian yield the energies of the adiabatic states [47]

$$E_\pm = \frac{\hbar}{2}\left(\Delta \pm \sqrt{\Omega^2 + \Delta^2}\right) \tag{3.23}$$

which differ by the effective Rabi frequency Ω_{eff} defined in Equation (3.20). Figure 3.3 shows these energies as a function of the detuning $\Delta(t)$. For $\dot{\Delta} \neq 0$, the energy levels exhibit an avoided crossing.

If the detuning $\Delta(t)$ is initially far below resonance ($|\Delta(-\infty)| \gg \Omega$, $\Delta < 0$), the initially populated diabatic state can be unambiguously identified with one distinct adiabatic state [47]

$$\begin{aligned} |\Phi_+(-\infty)\rangle &= |g\rangle \\ |\Phi_-(-\infty)\rangle &= |e\rangle \end{aligned} \tag{3.24}$$

At intermediate times, when the frequency is slowly swept from large detunings through resonance ($\Delta = 0$), the composition of both adiabatic states changes into a mixture of the diabatic states as described by Equation 3.21. Once the frequency chirp is completed ($|\Delta(+\infty)| \gg \Omega$, $\Delta > 0$), the diabatic states become uniquely identified with a single diabatic state again [47]

$$\begin{aligned} |\Phi_+(+\infty)\rangle &= |e, n\rangle \\ |\Phi_-(+\infty)\rangle &= |g, n+1\rangle \end{aligned} \tag{3.25}$$

It is obvious from (3.24) and (3.25) that complete population transfer to the excited state will be possible, if the state vector $|\Psi(t)\rangle$ of a system starting in its ground state adiabatically follows the adiabatic state $|\Phi_+(t)\rangle$ which is therefore also called *adiabatic transfer state*.

Adiabaticity requires the coupling between the two adiabatic states to be negligible compared to the difference of their eigenfrequencies [59; 47]

$$\frac{1}{\hbar}\left|E_+ - E_-\right| \gg \left|\left\langle \dot{\Phi}_+ \middle| \, \Phi_- \right\rangle\right| \tag{3.26}$$

which explicitly becomes [51; 52]

$$\Omega_{\text{eff}} = \sqrt{\Omega^2 + \Delta^2(t)} \gg \left|\frac{d}{dt}\Theta\left(t\right)\right| \tag{3.27}$$

Adiabatic passage in a two-level system is independent of the direction in which the detuning is swept through resonance [47]. The only difference between the case discussed above ($\dot{\Delta} > 0$) and chirping from large positive to large negative detuning is that the mixing angle Θ rotates counterclockwise from 0 to $\frac{\pi}{2}$ so that $|\Phi_-(t)\rangle$ instead of $|\Phi_+(t)\rangle$ is the adiabatic transfer state. This case is illustrated in Figure 3.3.

Another instructive description of ARP is possible in the Bloch vector model [7] and shall be reviewed briefly. The two poles of the Bloch sphere in Figure 3.4 correspond to ground and excited state of a two-level atom, respectively. For strongly red-detuned radiation, that is $|\Delta| \gg \Omega$, $\Delta < 0$, the vector associated with the effective Rabi frequency, $\mathbf{\Omega}_{\text{eff}}$, is almost antiparallel to the z-axis. The Bloch vector $\mathbf{R}$ precesses around $\mathbf{\Omega}_{\text{eff}}$ at frequency Δ. Slowly sweeping the detuning to the blue-detuned side through resonance will change the direction of $\mathbf{\Omega}_{\text{eff}}$ so that it is finally lined up parallel to the z-axis. If the chirp is slow enough, the Bloch vector will adiabatically follow this movement and continue its precessions around $\mathbf{\Omega}_{\text{eff}}$ until it reaches the north pole of the Bloch sphere, which leaves the atom in its excited state.

One major advantage of ARP is its robustness against small variations in laser intensity, detuning [47], pulse area and shape, and the precise location of the resonance [60]. Thus, even inhomogeneously broadened ensembles of atoms can be completely transferred to a selected state. However, meeting the adiabatic condition (3.27) can be difficult for a two-level system in the presence of spontaneous emission [60].

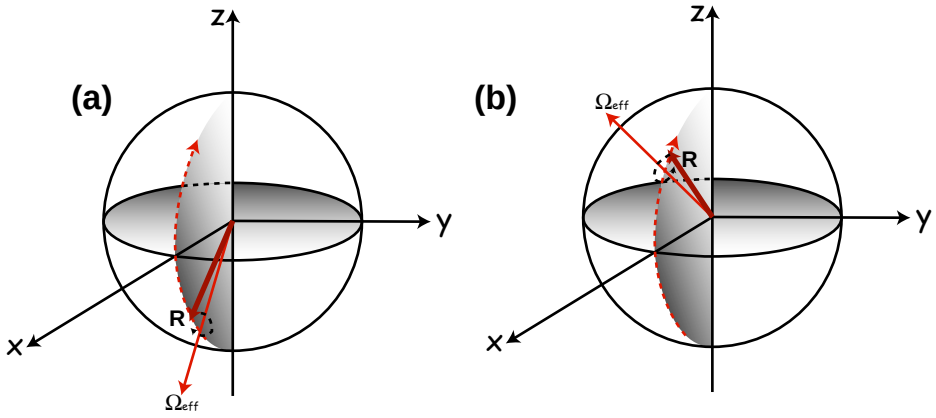

Figure 3.4 Bloch sphere description of adiabatic rapid passage. Sweeping the frequency from red detuning (a) to blue detuning (b) through resonance causes adiabatic population transfer from the ground state to the excited state

Although both π-pulses and adiabatic rapid passage have only been discussed for two-level systems, they can be generalized to multi-level systems and multiphoton transitions under some constraints [60]. Yet, the disadvantages are transferred as well. The π-pulse method, for example, requires resonant light and precise control of the pulse area and thus brings along numerous difficulties when dealing with an atomic ensemble.

Therefore, stimulated Raman adiabatic passage (STIRAP) as another highly efficient coherent excitation technique, for which less limiting restrictions apply, will be discussed in the text section.

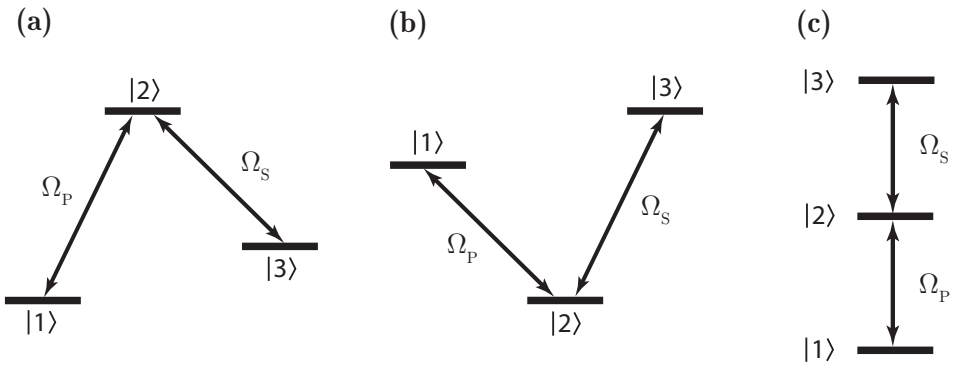

Figure 3.5 Λ (a) V (b) and ladder (c) excitation scheme for a three-level system. The different states are linked by a pump (P) and a Stokes (S) laser.

3.3 STIRAP

The simplest form of a multi-level system involves only three states, denoted $|1\rangle$, $|2\rangle$, and $|3\rangle$, of which one, here always taken to be $|2\rangle$, is coupled to the other two states by two separate coherent radiation fields, while there is no radiative coupling between $|1\rangle$ and $|3\rangle$. Figure 3.5 shows the different possible linkages between the three states, that are classified in terms of their appearance into Λ, V, and ladder scheme. The Λ configuration (Figure 3.5(a)) exemplifies a typical two-photon Raman [49] or stimulated Raman process [50], which is why the radiation fields acting on the initial state and linking the intermediate state with the final state are termed *pump* and *Stokes* fields, respectively. Quantum-beat interferences can be studied in the V scheme (3.5(b)) because of the two possible excitation branches, whereas the ladder configuration (3.5(c)) is especially suitable for the production of highly excited Rydberg atoms and can easily generalized to multiple levels [47]. Therefore,

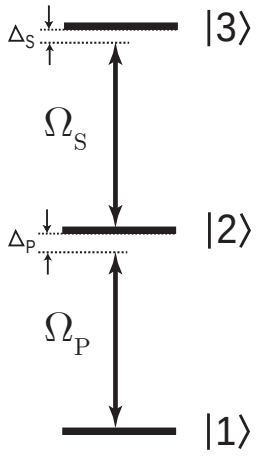

Figure 3.6 Three-level ladder excitation scheme with detunings Δ_P and Δ_S of pump and Stokes laser

the following discussion will be based on the generic ladder scheme shown in Figure 3.6.

Using steady fields for excitation will result in population oscillations (see 3.2), while applying sequences of pulse pairs in different orders makes durable and complete population transfer possible. Basically, there are two options: The intuitive model of population transfer suggests that the pump field precedes the Stokes field so that the applied fields always act on populated states. However, it turns out that reversing this intuitive order to a counter-intuitive pulse sequence with partially overlapping pulses will lead to a more efficient and complete population transfer in a process that is now known as stimulated Raman adiabatic passage (STIRAP). There are two options for the experimental implementation of the two different sequences: When pulsed laser radiation is used, the time delay between the pulses has to be controlled, while spatially

shifting the axes of the pump and Stokes lasers relative to each other is the choice to manipulate the timing of the pulses for continuous laser light traversing the laser beams at a right angle.

A quantitative analysis of the three-level problem starts with the time-dependent Schrödinger equation (3.17). For the rotating wave approximation to be justified, each of the two inolved lasers is required to couple only one pair of states. Therefore, $E_3 - E_1 \gg \hbar\Omega_k$ with $k = S, P$ has to hold unless the coupling given by the Rabi frequencies Ω_k is restricted by optical selection rules anyway due to the polarization of the laser beams [46]. Neglecting terms oscillating at sums or differences of the frequencies ω_P and ω_S of the pump and the Stokes laser, respectively, the Hamiltonian for purely coherent excitation can be expressed as [47]

$$H(t) = \frac{\hbar}{2} \begin{pmatrix} 0 & \Omega_P(t) & 0 \\ \Omega_P(t) & 2\Delta_P & \Omega_S(t) \\ 0 & \Omega_S(t) & 2\left(\Delta_P - \Delta_S\right) \end{pmatrix} \tag{3.28}$$

where the single-photon detunings Δ_k of the pump and Stokes lasers from their respective transitions in the ladder system of Figure 3.6 are defined by [47]

$$\begin{aligned} \hbar\Delta_P &= (E_2 - E_1) - \hbar\omega_P \\ \hbar\Delta_S &= (E_3 - E_2) - \hbar\omega_S \end{aligned} \tag{3.29}$$

For the process of stimulated Raman adiabatic passage, the single-photon detuning Δ_k does not crucially matter. However, two-photon resonance between

states $|1\rangle$ and $|3\rangle$ is an essential condition for STIRAP [47], and hence

$$\delta \equiv \Delta_P - \Delta_S = 0 \tag{3.30}$$

should always hold to conserve energy. In this case, the eigenvalues of (3.28) yield the energies $\hbar\omega_k$ corresponding to the instantaneous eigenstates $|\Phi_k(t)\rangle$ of the time-dependent Hamiltonian, where [47]

$$\begin{aligned} \omega_+(t) &= \Delta + \sqrt{\Delta^2 + \Omega_P^2(t) + \Omega_S^2(t)} \\ \omega_0(t) &= 0 \\ \omega_-(t) &= \Delta - \sqrt{\Delta^2 + \Omega_P^2(t) + \Omega_S^2(t)} \end{aligned} \tag{3.31}$$

The adiabatic states $|\Phi_k(t)\rangle$ are given as a superposition of the bare atomic states by the relations [47]

$$\begin{aligned} |\Phi_+(t)\rangle &= \sin\theta \sin\varphi\, |1\rangle + \cos\varphi\, |2\rangle + \cos\theta \sin\varphi\, |3\rangle \\ |\Phi_0(t)\rangle &= \cos\theta\, |1\rangle - \sin\theta\, |3\rangle \\ |\Phi_-(t)\rangle &= \sin\theta \cos\varphi\, |1\rangle - \sin\varphi\, |2\rangle + \cos\theta \cos\varphi\, |3\rangle \end{aligned} \tag{3.32}$$

with the time-dependent mixing angles $\theta(t)$ and $\varphi(t)$ defined by [47]

$$\tan\theta(t) = \frac{\Omega_P(t)}{\Omega_S(t)} \tag{3.33}$$

$$\tan 2\varphi(t) = \frac{\sqrt{\Omega_P^2(t) + \Omega_S^2(t)}}{\Delta} \tag{3.34}$$

The important thing to realize from Equation (3.32) is that the adiabatic state $|\Phi_0\rangle$ does not contain any contribution from the intermediate level $|2\rangle$. Assuming that the lifetime of the final state $|3\rangle$ is much longer than both

the lifetime of the intermediate state and the interaction time so that decay due to spontanteous emission will mostly occur from the intermediate level $|2\rangle$, population losses can be avoided or at least minimized if the population is confined to state $|\Phi_0\rangle$, being a coherent superposition of the initial state $|1\rangle$ and the final state $|3\rangle$ only, during the interaction. This extraordinary property makes the so-called *trapped state* $|\Phi_0\rangle$ an ideal transfer state for an efficient excitation process [47]. The assumption made above can indeed be justified for real experiments: In our case, for example, the lifetime of the $26S$ state in triplet helium ($\sim 40\ \mu$s) is much longer than the lifetime of the intermediate $3\ ^3\mathrm{P}_2$ level (~ 107 ns, see Appendix B).

Hence, as long as the state vector $|\Psi(t)\rangle$ of the system, which can be expanded in both the diabatic basis $\{|1\rangle, |2\rangle, |3\rangle\}$ and the adiabatic basis $\{|\Phi_+\rangle, |\Phi_0\rangle, |\Phi_-\rangle\}$, is tied to the trapped state $|\Phi_0\rangle$ during the interaction, complete population transfer becomes possible, because the lossy intermediate state remains unpopulated throughout the excitation process [47].

Since the mixing angle $\theta(t)$ determines the time evolution of the trapped state, it is possible to make $|\Phi_0\rangle$ evolve from the ground state $|1\rangle$ to the target state $|3\rangle$ via a superposition of these two levels at intermediate times during the interaction by controlling the Rabi frequencies of the pump and the Stokes laser in a suitable way. For the counterintuitive pulse ordering in STIRAP, the ratio of the two Rabi frequencies becomes [47]

$$\begin{aligned} \frac{\Omega_P(t \to -\infty)}{\Omega_S(t \to -\infty)} &\to 0 \\ \frac{\Omega_S(t \to \infty)}{\Omega_P(t \to \infty)} &\to 0 \end{aligned} \tag{3.35}$$

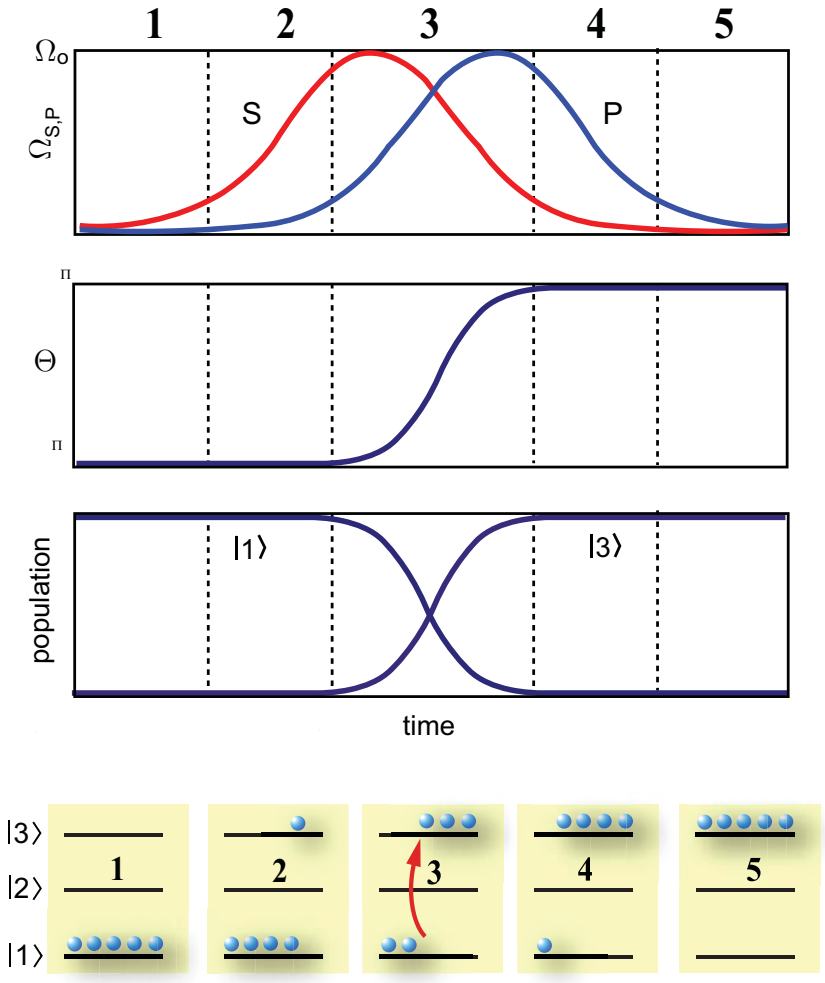

Figure 3.7 Five-step description of STIRAP displaying the time evolution of the Rabi frequencies $\Omega_{S,P}$, the mixing angle Θ, and the populations in states $|1\rangle$ and $|3\rangle$ [47]

Therefore, the mixing angle (3.33) rises from its initial value $\theta(t \to -\infty) = 0$ to $\theta(t \to +\infty) = \frac{\pi}{2}$ which is exactly what is needed for the desired time evolution of $|\Phi_0\rangle$.

At this point it should be noted that complete population transfer is also possible with the intuitive pulse order when the two-photon resonance is maintained ($\delta = 0$) whereas the single-photon detuning of the lasers deviates from resonance ($\Delta_k \neq 0$). In that case, $|\Phi_-\rangle$ shows the desired asymptotic behavior and serves as the adiabatic transfer state providing the connection between the ground state $|1\rangle$ and the final state $|3\rangle$. In contrast to STIRAP, however, the intermediate state participates in the transfer process so that even for ideal adiabatic evolution, population losses are inevitable as soon as the lifetime of the intermediate state $|2\rangle$ becomes comparable to the time scale of the excitation process [47].

The STIRAP process can be subdivided into five stages parameterized by the mixing angle $\theta(t)$, that is, the variation of the relative strengths of the pump and the Stokes field in time. Figure 3.7 depicts the time evolution of the two Rabi frequencies Ω_P and Ω_S, respectively, the resulting mixing angle, and the populations in the ground state and the target state [47].

In phase 1, all the population is assumed to reside in the ground state. As only the Stokes laser is present with continuously increasing intensity, the mixing angle θ remains zero so that the state vector $|\Psi\rangle$ is lined up parallel to $|\Phi_0\rangle$. The interaction of the Stokes light with the two upper levels results in the

so-called Autler-Townes splitting (see Section 3.5) of the dressed eigenstates of Equation (3.32) which is a prerequisite for the lossless transfer process starting in phase 2. This phase is therefore denoted *Stokes-induced Autler-Townes phase*.

In phase 2, the intensity of the pump pulse starts increasing, while the Stokes pulse has nearly reached its peak intensity. Hence, the mixing angle θ is still close to zero, and the state vector does not deviate too much from $|1\rangle$. Furthermore, the Autler-Townes effect induced by the Stokes pulse causes the transition rates from the ground state to the two Autler-Townes states to cancel. Since the same mechanism also leads to electromagnetically-induced transparency (EIT), phase 2 is called *Stokes-induced EIT phase*.

Phase 3 is the *adiabatic passage phase* in which the essential population dynamics takes place. As the Stokes pulse decreases after reaching its maximum intensity, it overlaps with the pump pulse whose intensity is approaching its peak value. Therefore, the mixing angle θ rises from ~ 0 to $\sim \frac{\pi}{2}$ and forces the state vector $|\Psi\rangle$ to follow the evolution of $|\Phi_0\rangle$ from the ground state $|1\rangle$ to the excited state $|3\rangle$. Ideally, the intermediate state $|2\rangle$ is completely bypassed by STIRAP.

In phase 4 (*pump-induced EIT phase*), the still relatively strong pump pulse induces Autler-Townes splitting of the two lower levels leading to the cancellation of the transition rates from the excited state to these levels. Hence, there is no loss due to optical pumping by the weak Stokes radiation out of the excited state in which almost the complete population can be found

($|\Psi\rangle \approx -|3\rangle$).

In phase 5, denoted *pump-induced Autler-Townes phase*, the time evolution of the mixing angle ends at a value of $\theta = \frac{\pi}{2}$, ideally leaving the complete initial population in the excited state $|3\rangle$.

Figure 3.8 gives a vector picture of the STIRAP process in Hilbert space to further illustrate the previous argumentation: If the trapped state $|\Phi_0\rangle$ is rotated from $|1\rangle$ to $-|3\rangle$ under adiabatic conditions, the state vector $|\Psi\rangle$ will follow the evolution of $|\Phi_0\rangle$ in the plane spanned by $|1\rangle$ and $|3\rangle$, thereby avoiding any contribution of the intermediate state $|2\rangle$.

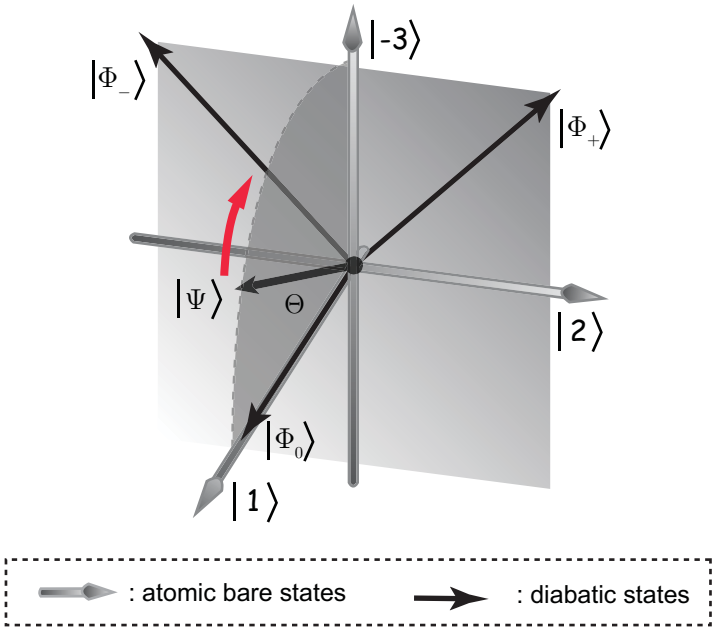

Figure 3.8 Vector picture of STIRAP in Hilbert space [46; 47]. The state vector $|\Psi\rangle$ adiabatically follows the evolution of the trapped state $|\Phi_0\rangle$ in the plane spanned by the atomic bare states $|1\rangle$ and $|3\rangle$. Θ represents the mixing angle.

As should be obvious from the previous discussions, STIRAP is mostly independent of the properties of the intermediate state $|2\rangle$. Under adiabatic conditions, the time scale of the interaction can thus exceed the lifetime of the lossy state. However, STIRAP critically depends on the coherence of the radiation, because any kind of phase fluctuation will cause deviations from adiabaticity and thus lead to population loss. The following section discusses the prerequisites for adiabatic evolution and the sensitivity of STIRAP to the parameters of the interaction in more detail.

3.4 Limitations

3.4.1 Decay from Intermediate and Excited State

As mentioned above, STIRAP ideally does not depend on the lifetime of the intermediate state $|2\rangle$, which is completely bypassed by the population transfer process in the adiabatic limit, and decay from the excited state $|3\rangle$ due to spontaneous emission is negligible as long as its lifetime is much bigger than the lifetime of the intermediate state and the time scale of the interaction. In reality, however, the effects of these two decay channels have to be accounted for.

Whereas spontaneous emission out of states $|3\rangle$ and $|2\rangle$ into states belonging to the three-level system require a density matrix treatment, the possibility of irreversible losses from state $|j\rangle$ at a decay rate Γ_j out of the system can be modeled by including the substitution $E_j \rightarrow E_j - \frac{i}{2}\Gamma_j$ in the previous dis-

cussion based on the Schrödinger equation so that on two-photon resonance ($\delta = 0$) the Hamiltonian in Equation (3.28) becomes [47; 43]

$$H(t) = \frac{\hbar}{2} \begin{pmatrix} 0 & \Omega_P(t) & 0 \\ \Omega_P(t) & 2\Delta - i\Gamma_2 & \Omega_S(t) \\ 0 & \Omega_S(t) & -i\Gamma_3 \end{pmatrix} \tag{3.36}$$

For small to medium decay rates, population losses from the intermediate state occur because of imperfect adiabaticity resulting in nonadiabatic coupling between the trapped state and the other adiabatic states. The dominating process at large decay rates is quantum overdamping which effectively decouples the three-level system from the laser fields [47].

Figure 3.9 shows the results of a numerical calculation for the time evolution of the population in the excited state of a three-level system described by the Hamiltonian (3.36).

A Gaussian pulse shape, namely $\Omega_P(t) = \frac{\Omega_P(0)}{2} e^{\left[-(10^6 t - 6)^2\right]}$ for the pump laser and $\Omega_S(t) = \frac{\Omega_S(0)}{2} e^{\left[-(10^6 t - 4.6)^2\right]}$ for the Stokes laser was assumed with peak Rabi frequencies $\Omega_P(0) = 35$ MHz and $\Omega_S(0) = 40$ MHz, respectively. The other parameters in the calculation were taken to be 1500 $\frac{\text{m}}{\text{s}}$ for the mean velocity of the atomic beam, 1 mm for the beam waist of both lasers, and 1.4 μs for the delay time between the pump and the Stokes pulse. The effect of decay is clearly observable: Not the entire population is transferred to the excited state during the interaction, and population loss occurs as time evolves further.

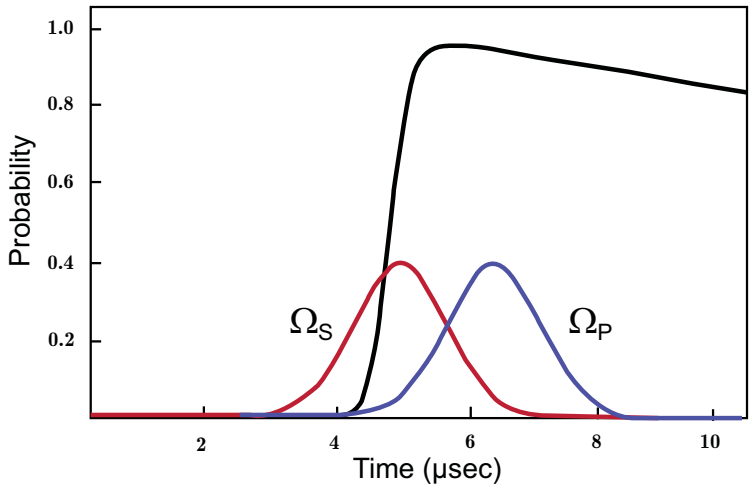

Figure 3.9 Numerically calculated time evolution of the population in a Rydberg state. The curves labelled Ω_P and Ω_S represent the time order of the pump and the Stokes laser, respectively. [43]

3.4.2 Adiabaticity

For the state vector $|\Psi(t)\rangle$ to undergo an adiabatic time evolution, nonadiabatic transfer from the trapped state $|\Phi_0\rangle$ to the two other adiabatic states $|\Phi_\pm\rangle$ has to be avoided or at least minimized. General quantum mechanical considerations yield that the Hamiltonian matrix element for nonadiabatic coupling $\left\langle \dot{\Phi}_0 \middle| \Phi_\pm \right\rangle$ should be small compared to the difference between the energies of the adiabatic states [46]

$$\left| \left\langle \dot{\Phi}_0 \middle| \Phi_\pm \right\rangle \right| \ll |\omega_0 - \omega_\pm| \tag{3.37}$$

Using the expansions (3.32) of the adiabatic states in the diabatic basis, the strengths of the nonadiabatic couplings in (3.37) become

$$\begin{aligned} \left\langle \dot{\Phi}_0 \middle| \, \Phi_+ \right\rangle &= -\dot{\theta} \sin\varphi \\ \left\langle \dot{\Phi}_0 \middle| \, \Phi_- \right\rangle &= -\dot{\theta} \cos\varphi \end{aligned} \tag{3.38}$$

On one-photon resonance ($\Delta_k = 0$), the adiabatic constraint simplifies to [4]

$$\left|\dot{\theta}\right| \ll |\omega_0 - \omega_\pm| = \Omega_{\text{eff}} \tag{3.39}$$

with the effective Rabi frequency given by $\Omega_{\text{eff}} = \sqrt{\Omega_P^2 + \Omega_S^2}$. A local adiabaticity criterion in terms of the Rabi frequencies can be derived from the definition of the mixing angle $\theta(t)$ in Equation (3.33) [46]

$$\left|\dot{\theta}\right| = \left| \frac{\dot{\Omega}_P \Omega_S - \Omega_S \dot{\Omega}_P}{\Omega_P^2 + \Omega_S^2} \right| \ll \Omega_{\text{eff}} \tag{3.40}$$

If the shape of the laser pulses is known, an evaluation of Equation (3.40) is possible at any time, and nonadiabatic couplings between $|\Phi_0\rangle$ and $|\Phi_\pm\rangle$ are negligible as long as (3.40) holds throughout the interaction [46]. Under the assumption that the pump and Stokes pulses are sufficiently smooth, a global adiabatic constraint can be obtained from (3.39) by time-averaging the left-hand side. If the pump and the Stokes pulse overlap in a time interval $\Delta\tau$, substituting $\left\langle \dot{\theta} \right\rangle = \frac{\pi}{2\Delta\tau}$ into (3.39) yields [46]

$$\Omega_{\text{eff}} \Delta\tau \gg 1 \tag{3.41}$$

where the left-hand side is essentially the pulse area. Experimental experience and numerical simulation suggest that efficient population transfer demands $\Omega_{\text{eff}} \Delta\tau > 10$ [47; 46].

3.4.3 Sensitivity to Interaction Parameters

Most of the various factors that affect adiabaticity are also accessible parameters in experimental reality. Hence, in order to maximize the experimental transfer efficiency of STIRAP, these parameters have to be optimized.

As far as the delay between the pump and the Stokes pulse is concerned, STIRAP turns out to be rather robust against small deviations from the optimal delay which is usually obtained for the case where the mixing angle $\theta(t)$ changes slowly and smoothly in time. The particular optimal value depends on the pulse shape, however, and was determined to be about equal to the pulse width for Gaussian pulses [4].

The Rabi frequencies of the pump and the Stokes beam are adjustable by changing the intensities of the laser beams (see Table 3.1). The transfer efficiency will be best, if the two peak Rabi frequencies are nearly equal. However, if the coupling between the atom and the radiation fields is too small, that is, the Rabi frequencies are not strong enough, the state vector $|\Psi(t)\rangle$ will lag behind the time evolution of the adiabatic transfer state and therefore precess around $|\Phi_0(t)\rangle$ [46]. Therefore, the peak Rabi frequencies should be comparable and sufficiently strong. If the pulse widths are about equal, too, the pulse area required for the population transfer can be reduced [47].

For atoms traversing laser beams, the interaction time is determined by the geometry of the beams. Although the optimal beam geometry also depends on the particular application, meaning, for example, whether a low required excitation intensity or a high flux of excited atoms or molecules is preferred, as

Transitions	$2^3S_1 \rightarrow 3^3P_2$	$3^3P_2 \rightarrow 26^3S_1$
$m = 0$	$\Omega_P(0) = 1.78 \times 10^2\sqrt{I_P}$ MHz	$\Omega_S(0) = 0.117 \times 10^2\sqrt{I_S}$ MHz
$m = \pm 1$	$\Omega_P(1) = 1.54 \times 10^2\sqrt{I_P}$ MHz	$\Omega_S(1) = 0.1 \times 10^2\sqrt{I_S}$ MHz

Table 3.1 Formulae to convert the laser beam intensities $I_{P,S}$ (given in W cm^{-2}) into Rabi frequencies $\Omega_{P,S}$ for the two transitions used in the experiment.[43]

a general rule of thumb, the transit time through the region where pump and Stokes pulse overlap (phase 3 in the five-step description of STIRAP) should be small with respect to the inverse of the laser linewidth [47].

As mentioned above, STIRAP does not depend on the single-photon detuning Δ_k in so far that the existence of the trapped state $|\Phi_0\rangle$ and its composition are independent of Δ_k. However, the mixing angle φ depends on Δ_k and thus affects the adiabatic condition given by Equation (3.38). Increasing Δ_k introduces nonadiabatic couplings and population loss [47]. Consequently, the optimum transfer efficiency is obtained on single-photon resonance. This is exemplified in Figure 3.10 which shows the results of a numerical calculation of the excitation probability for different Δ_k.

The sensitivity to the two-photon detuning δ is a crucial property of STIRAP. For non-zero δ, diagonalizing the Hamiltonian (3.28) yields different eigenstates than the ones given in Equation (3.32). Particularly, none of these eigenstates can serve as an adiabatic transfer state because all of them connect the same diabatic states asymptotically. Thus, highly efficient population transfer with STIRAP is only possible on two-photon resonance. This condi-

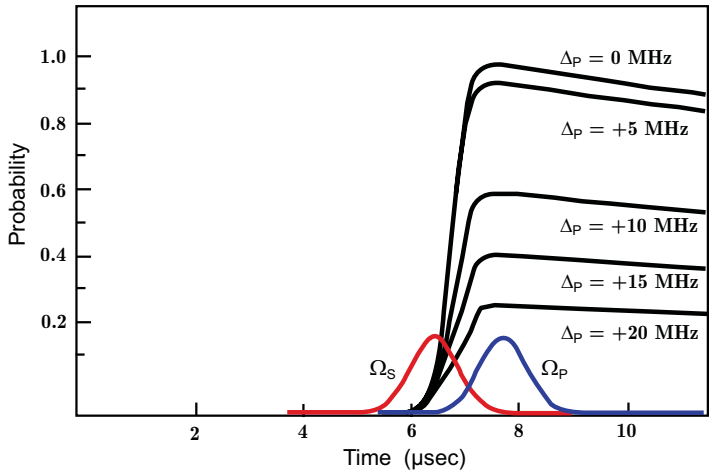

Figure 3.10 Numerical calculation of Rydberg state population as a function of single-photon detuning Δ_P [43]

tion also follows intuitively from energy conservation.

3.5 Autler-Townes Effect

3.5.1 Dressed Atom Picture

The theory of coherent excitation presented above can be extended by explicitly including the energy of the radiation field in the total Hamiltonian of the system. When doing so, an instructive picture of the effects of the atom-photon interaction in an atomic system interacting with a monochromatic resonant or near-resonant laser field, the so-called *dressed atom picture*, arises [61]. The total Hamiltonian of atom and field can be written as [59]

$$H = H_A + H_F + H_I \tag{3.42}$$

where H_A is the atomic part which yields the atomic energy levels E_k, the field part H_F gives the energy $E_n = \left(n + \frac{1}{2}\right)\hbar\omega$ of the single mode radiation field of frequency ω, and the atom-field interaction part $H_I = -\mathbf{P} \cdot \mathbf{E}$ is taken to be the electric dipole interaction between the electric dipole moment $\mathbf{P}$ of the atom and the radiation field $\mathbf{E}$.

The eigenstates of the interaction-free Hamiltonian $H_0 = H_A + H_F$ can be labeled $|k, n\rangle$, if k and n denote the atomic state and the photon number, respectively. Neglecting the vacuum energy of the radiation field, the energy eigenvalues of H_0 become $E_{k,n} = E_k + n\hbar\omega$. Therefore, the energy level diagram for the atom-field system shows an infinite sequence of atomic energy level columns shifted by one photon energy $\hbar\omega$ with respect to each other. Consider the states **A**, **B**, and **C** in Figure 3.11. If the frequency of the field is close to the Bohr frequency ω_{21} of the transition between the atomic levels $|2\rangle$ and $|1\rangle$, states **B** and **C**, or $|2, n-1\rangle$ and $|1, n\rangle$ in the notation introduced above, will be nearly degenerate without atom-field interaction [59].

$$\begin{aligned} E_{1,n} &= E_1 + n\hbar\omega \\ E_{2,n-1} &= E_{1,n} + \hbar\Delta_{st} \end{aligned} \tag{3.43}$$

The remaining energy separation between the levels is determined by the detuning $\Delta_{st} = \omega_{21} - \omega$ (see Figure 3.12 (b)).

In the presence of the interaction H_I, the coupling between atom and field mixes the states $|1, n\rangle$ and $|2, n-1\rangle$ so that the states $|k, n\rangle$ are no longer eigenstates of the total Hamiltonian H. The new eigenbasis is given by the

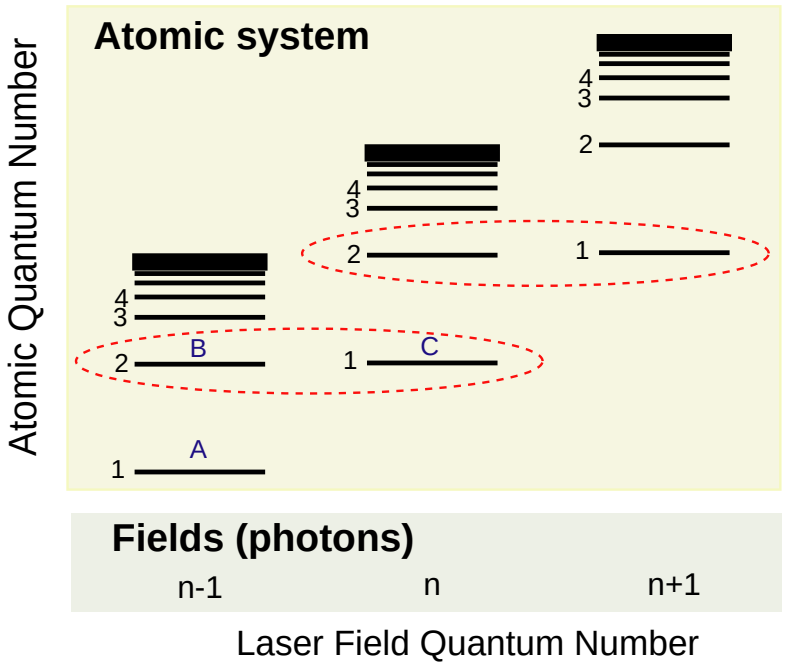

Figure 3.11 Energy level diagram for the atom-field Hamiltonian. Adjacent columns representing a typical atomic energy level scheme are vertically displaced by $\hbar\omega$. Nearly degenerate pairs of levels are indicated.[7; 43]

so-called *dressed states* [59] (see Figure 3.12 (c))

$$\begin{aligned} |\Phi_1\rangle &= \cos\theta\,|1,n\rangle - \sin\theta\,|2,n-1\rangle \\ |\Phi_2\rangle &= \sin\theta\,|1,n\rangle + \cos\theta\,|2,n-1\rangle \end{aligned} \tag{3.44}$$

with the mixing angle θ defined in (3.22). If the energy of the unperturbed $|2,n-1\rangle$ level marks the energy origin, the corresponding eigenenergies of the dressed states become [59; 62]

$$\begin{aligned} E_{\Phi_1} &= -\frac{\hbar}{2}\left(\Delta_{st} + \Omega_{\text{eff}}\right) \\ E_{\Phi_2} &= -\frac{\hbar}{2}\left(\Delta_{st} - \Omega_{\text{eff}}\right) \end{aligned} \tag{3.45}$$

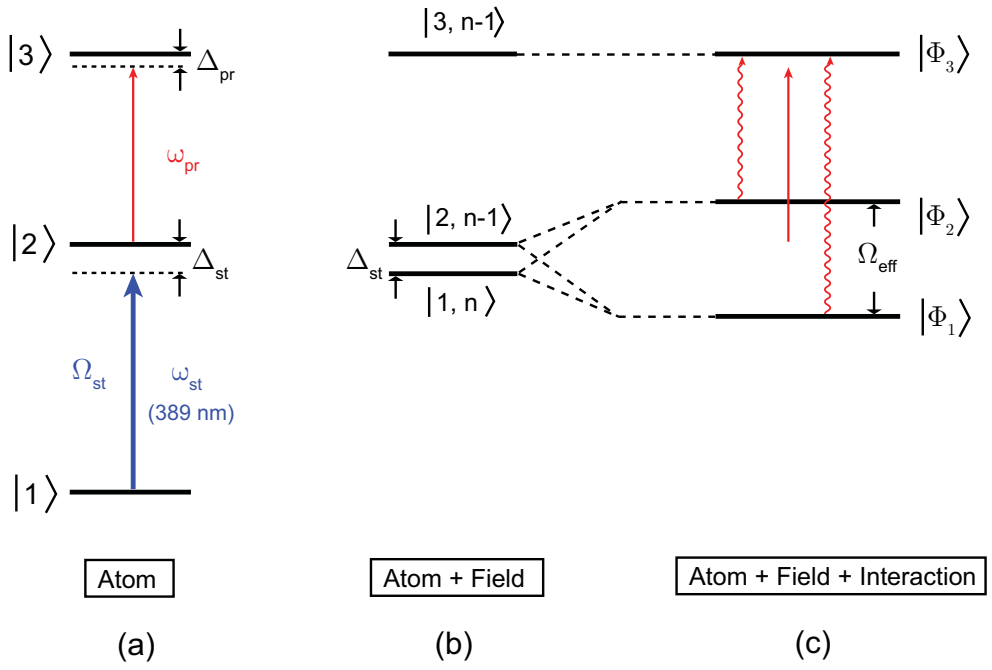

Figure 3.12 Energy level diagram for (a) pure atomic (b) atom-field (c) atom-field-interaction Hamiltonian (modified from [43]). The formation of the dressed states $|\Phi_k\rangle$ in (c) gives rise to the observation of the Autler-Townes effect.

where the effective Rabi frequency $\Omega_{\text{eff}} = \sqrt{\Omega_{st}^2 + \Delta_{st}^2}$ parameterizes the coupling strength through the Rabi frequency Ω_{st} defined in (3.8). Similarly to the unperturbed states, the dressed states form an infinite sequence of pairs with regard to n. The energy difference between pairs amounts to one laser photon $\hbar\omega$. However, Equation (3.45) indicates that the dressed states exhibit an energy separation of $\hbar\Omega_{\text{eff}}$ in contrast to the unperturbed states which differ in energy by $\hbar\Delta_{st}$. In the limit of weak excitation ($\Omega_{st} \to 0$), the dressed states asymptotically turn into the unperturbed states as $\theta \to 0$.

3.5.2 Autler-Townes Effect

One of the advantages of the dressed atom picture is that the theory of some elementary processes such as resonance fluorescence or absorbtion takes a particularly simple form when expressed in dressed states [59]. The Autler-Townes effect, which was first observed in the microwave regime by Autler and Townes who did a pump-probe-spectroscopy experiment on carbonyl sulfide (OCS) [5], represents an important example that can be studied in the course of our experiment.

Consider the three-level system shown in Figure 3.12 (a). The system can undergo two transitions $|3\rangle \leftrightarrow |2\rangle$ and $|2\rangle \leftrightarrow |1\rangle$, which share the intermediate state $|2\rangle$ as a common level. Shining a nearly resonant laser (frequency ω_{st}) of high intensity on the transition between the levels $|1\rangle$ and $|2\rangle$ strongly couples these states and thus creates the dressed states $|\Phi_1\rangle$ and $|\Phi_2\rangle$ given by (3.45). If the Bohr frequency ω_{32} corresponding to the transition between the third level $|3\rangle$ and the intermediate level $|2\rangle$ is sufficiently different from the Bohr frequency ω_{21} of the strongly coupled transition, the upper level will not be perturbed by the strong dressing laser (see Figure 3.12 (c)). Hence, the eigenstates of the system are given by [62]

$$\begin{aligned} |\Phi_1\rangle &= \cos\theta\,|1,n\rangle - \sin\theta\,|2,n-1\rangle \\ |\Phi_2\rangle &= \sin\theta\,|1,n\rangle + \cos\theta\,|2,n-1\rangle \\ |\Phi_3\rangle &= |3,n-1\rangle \end{aligned} \tag{3.46}$$

Using the same energy origin as in (3.45), the corresponding eigenenergies

become

$$\begin{aligned} E_{\Phi_1} &= -\frac{\hbar}{2}\left(\Delta_{st} + \Omega_{\text{eff}}\right) \\ E_{\Phi_2} &= -\frac{\hbar}{2}\left(\Delta_{st} - \Omega_{\text{eff}}\right) \\ E_{\Phi_3} &= \hbar\omega_{32} \end{aligned} \tag{3.47}$$

The absorption spectrum of a low intensity laser (frequency ω_{pr}) whose detuning $\Delta_{pr} = \omega_{32} - \omega_{pr}$ from resonance with the upper transition $|3\rangle \leftrightarrow |2\rangle$ is scanned around its unperturbed resonance with a sufficiently large scan amplitude will therefore show two absorption peaks in the presence of the strong dressing laser. These two peaks are often called Autler-Townes doublet. The resonances corresponding to the transistions $|\Phi_i\rangle \rightarrow |\Phi_3\rangle$ $(i = 1, 2)$ occur for the detunings

$$\begin{aligned} \Delta_{pr}^{\Phi_{32}} &= -\frac{\hbar}{2}\left(\Delta_{st} - \Omega_{\text{eff}}\right) &&= E_{\Phi_2} \\ \Delta_{pr}^{\Phi_{31}} &= -\frac{\hbar}{2}\left(\Delta_{st} + \Omega_{\text{eff}}\right) &&= E_{\Phi_1} \end{aligned} \tag{3.48}$$

This shows that the unperturbed absorption peak at ω_{32} splits into two components $\omega_{32} + \frac{\hbar}{2}\left(\Delta_{st} \pm \Omega_{\text{eff}}\right)$ separated by Ω_{eff} in the dressed system. Since $E_{\Phi_2} > E_{\Phi_1}$ holds at all times, the resonance with $|\Phi_2\rangle$ occurs on the red side of the absorption spectrum, whereas the resonance with $|\Phi_1\rangle$ is blue-detuned.

When the dressing laser is on resonance ($\Delta_{st} = 0$), the separation of the doublet reduces to Ω_{st} and thus provides an opportunity to experimentally determine the Rabi frequency of a laser (see Figure 3.13 (a)). For large negative detunings Δ_{st} of the strong laser (see Figure 3.13 (b)), the resonance with $|\Phi_1\rangle$, which due to $\theta \approx \frac{\pi}{2}$ mostly contains contributions from $|2, n-1\rangle$ in that

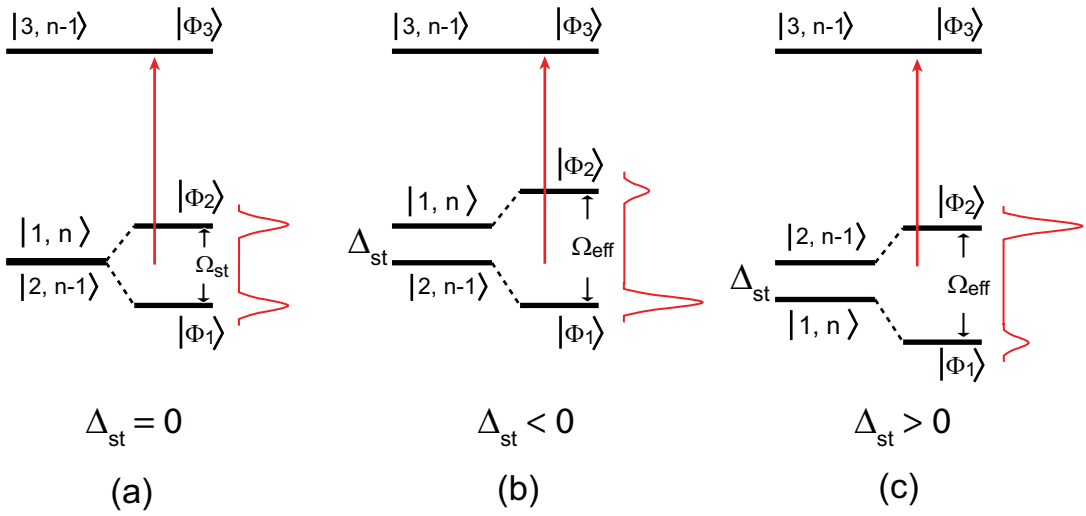

Figure 3.13 Dependence of the Autler-Townes splitting on the detuning Δ_{st} of the strong laser: (a) resonance (b) red-detuning (c) blue-detuning [43]

case, occurs for $\Delta_{pr} \approx 0$. When $\Delta_{pr} \approx \Delta_{st}$, the probe laser is resonant with $|\Phi_2\rangle$ (predominantly $|1, n\rangle$. For $\Delta_{st} \gg 0$ (see Figure 3.13 (c)), the inverse is true because of $\theta \approx 0$, and thus the resonances at $\Delta_{pr} \approx 0$ and $\Delta_{pr} \approx \Delta_{st}$ can be associated with $|\Phi_2\rangle$ and $|\Phi_1\rangle$, respectively.

The intensities of the components generally depend both on the steady state population of the levels $|\Phi_i\rangle$ and on the transition rates to $|\Phi_3\rangle$ [61].

Chapter 4

Atom Optical Manipulation of He Atoms

4.1 Focusing Neutral Atoms

Among the various atom optical elements such as mirrors, beamsplitters, and waveguides, lenses play a crucial role. The basic requirements for a focusing lens for an atomic beam are a restoring force on the atoms for small transverse displacements from the trajectoy through the center of the lens and that this force vanishes on the symmetry axis of the lens [63]. Electrostatic lenses are not only favorable because of their simple construction, but also because their successful operation is essentially independent from the atom species [64]. The dipole force experienced by an atom in an inhomogeneous electric field can be written as [64]

$$\mathbf{F} = \nabla \left(\mathbf{P} \cdot \mathbf{E} \right) = \frac{\alpha}{2} \nabla \left| \mathbf{E} \right|^2 \tag{4.1}$$

with $\mathbf{P} = \alpha \, \mathbf{E}$ where $\mathbf{P}$ and α are the dipole moment and the polarizability ($\alpha > 0$ for atoms in a stable state) of the atom, respectively. Note that the force does not depend on the direction of the elecric field. With $\mathbf{F} = -\nabla W$,

the dipole force can be derived from a Stark potential

$$W = -\frac{\alpha}{2} |\mathbf{E}|^2 \tag{4.2}$$

For the force to be restoring, $\nabla \mathbf{F} < 0$ is required [63; 65]. However, for ground state atoms in static electric fields $\nabla \mathbf{F} \geq 0$ [65] as a consequence of what is today known as the Earnshaw theorem [66] which states that there can be no local maximum of a static electric field in a space devoid of charges and currents [67]. Therefore, it is impossible to focus ground-state atoms with a single axially symmetric thin lens [65], because the force exerted on ground-state atoms by an electric field gradient is always directed towards the stronger field (strong-field seeking).

To focus a beam of ground state atoms in both transverse directions, a combination of at least two lenses in an alternating gradient configuration has to be used. Although each lens focuses in one and defocuses in the other transverse direction, a net focusing effect is achieved if the gradients created by the lenses alternate such that the focusing/defocusing is opposite for each transverse direction [68]. This is the case, as atoms that are defocused in the first lens are further away from the center of the second lens and thus experience a stronger restoring force. Vice versa, atoms focused by the first lens are less defocused by the second lens. Since the magnifications of both lenses are generally unequal, a third lens can be used to control the magnification [68; 69].

Whereas electric field gradient focusing is a standard technique for polar molecules [63], the small polarizabilities α of neutral atoms (on the order of

10^{-39} Fm^2) make it more difficult to focus them because of the weak interaction of the field gradient and the dipole moment induced by the external field. This is one reason why first successful experiments have only been carried out recently [69].

Since the polarizability of Rydberg atoms scales with the principal quantum number as n^7 (see Table 2.1), moderate electric field gradients are sufficient to focus our beam of He Rydberg atoms with an electrostatic field lens which will be described in the follwing section.

4.2 Electrostatic Hexapole Lens

For best focusing results, the restoring forces exerted by the field lens have to be linear in displacement from the beam axis in any direction and independent from simultaneous displacement in other directions (uncoupled motion). Strong non-linearities will cause unwanted effects such as a larger beam size or loss of beam flux [70], and thus the shape of the electrodes have to be carefully chosen to produce the least non-linearities. For such an aberration-free lens, the most general form of a potential Φ that is consistent with Laplace's equation $\nabla^2\Phi = 0$ can be expressed as a multipole expansion in cylindrical coordinates ($r = \sqrt{x^2+y^2}$ and $\theta = \tan^{-1}\left(\frac{y}{x}\right)$) [63]

$$\Phi(r,\theta) = \Phi_0 \left[\sum_{n=1}^{\infty} \frac{a_n}{n} \left(\frac{r}{r_0}\right)^n \cos(n\theta) + \sum_{n=1}^{\infty} \frac{b_n}{n} \left(\frac{r}{r_0}\right)^n \sin(n\theta) \right] \tag{4.3}$$

where r_0 and Φ_0 are scaling factors characterizing the size of the electrode structure and the applied voltages, respectively, and a_n and b_n are the dimen-

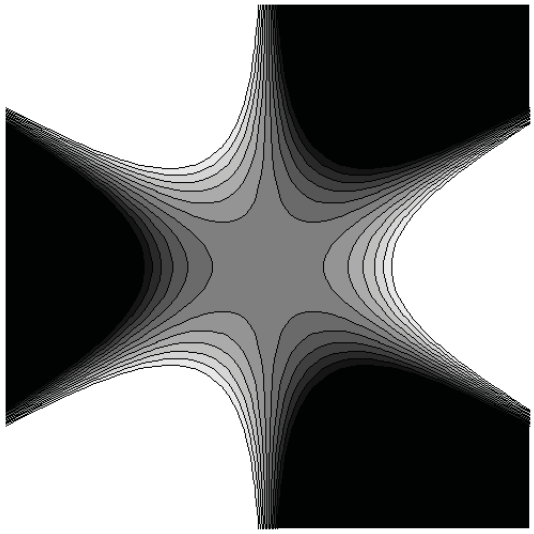

Figure 4.1 Equipotential lines for an electric hexapole potential [43]

sionless expansion coefficients. The $n = 1, 2, 3, ...$ terms in (4.3) represent the $2n$-pole fields. To obtain an electric field that is symmetric under reflection in the two transverse axes, we can set $b_n = 0$ [63]. The best electric field to focus neutral atoms is the one derived from a hexapole potential ($n = 3$), because it provides the desired linearity in the displacement from the beam axis. For a pure hexapole potential, (4.3) becomes

$$\Phi(r, \theta) = \frac{\Phi_0 a_3}{3} \left(\frac{r}{r_0}\right)^3 \cos 3\theta \tag{4.4}$$

A plot of this hexapole potential is shown in Figure 4.1, and instead of using separate electrode pairs in alternating gradient configuration (as for example in [69]), six electrodes matching the equipotential lines were machined to constitute the field lens in our experiment (Figure 4.2). However, apart from the fact that a real lens is always a truncated equipotential and thus suffers from

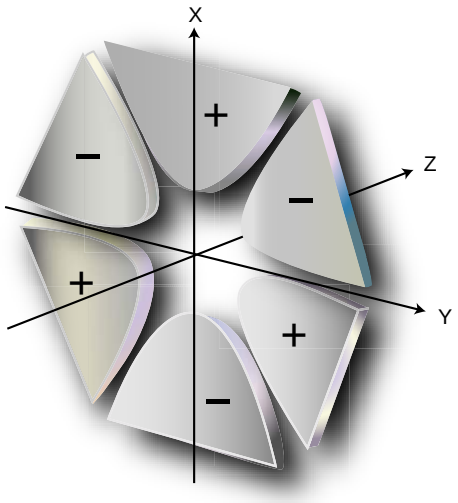

Figure 4.2 Geometry of the electrostatic hexapole lens. The atomic beam is propagating along the z-axis. [43]

non-linearities due to residual higher order multipoles, the finite lens length introduces undesired end effects [70]: The axial component of the electric field gradient affects both the transverse motion and the longitudinal velocity, and fringe fields extend the physical length of the lens.

The radial force exerted on the atomic beam by the hexapole lens can be calculated under the assumption that the induced dipole moment P of the atoms is parallel to the electric field and of equal magnitude for all the atoms in the beam. Combining $\mathbf{E} = -\nabla\Phi$, (4.4), and (4.1) yields

$$\mathbf{F} = -\frac{2P\Phi_0 a_3}{r_0^3}\mathbf{r} \tag{4.5}$$

which is the differential equation of a harmonic oscillator with spring constant $k = \frac{2P\Phi_0 a_3}{r_0^3}$ and thus fulfills the requirement of linearity in displacement from the beam axis.

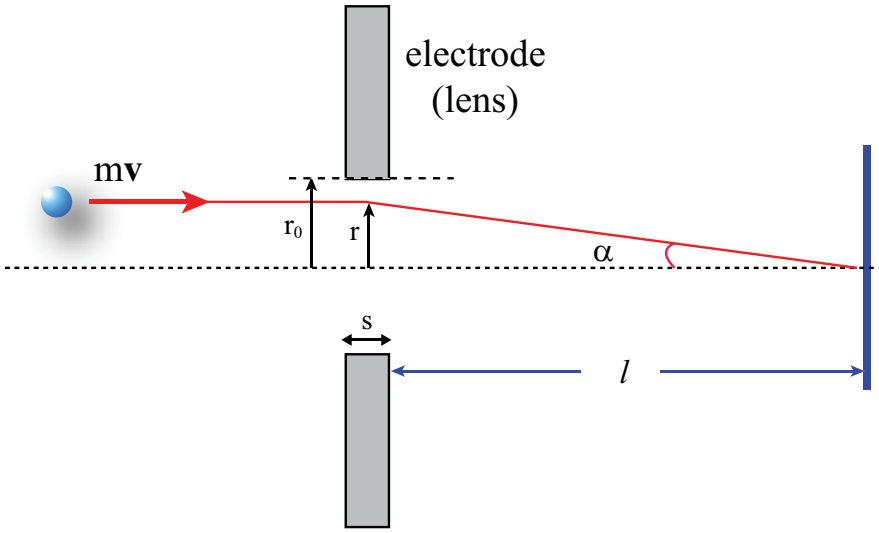

Figure 4.3 Trajectory of an atom passing through the hexapole lens [43]

To derive a formula for the focal length of the hexapole lens, consider Figure 4.3: An atom of mass M is traversing the lens (internal radius r_0, physical length s) at velocity v on a trajectory that is r away from the center of the lens in a time interval $\Delta t = \frac{s}{v}$. For small angles α, conservation of momentum yields

$$\sin\alpha = \frac{r}{\sqrt{r^2 + \left(l + \frac{s}{2}\right)^2}} \approx \frac{F\Delta t}{Mv} \tag{4.6}$$

Assuming $l \gg r, s$ (thin lens approximation) and using (4.5), the focal length of the field lens can be calculated from (4.6) to be

$$l = \frac{Mv^2 r_0^3}{3sP\Phi_0 a_3}, \tag{4.7}$$

Therefore, the position of the focal plane depends on both atomic properties (M, v, P) and the geometry and operation of the lens (s, r_0, Φ_0). However, Equation 4.7 is only a simple zeroth order approximation, and the higher order

solutions of (4.6) show that the focal length approximately depends on the distance of the atomic trajectory from the symmetry axis of the lens as $l \propto r$. In addition to the chromatic aberrations arising from $l \propto v^2$, the lens therefore also suffers from spherical aberrations.

Chapter 5

Helium

The physics of helium (chemical symbol He) comprises very interesting phenomena and applications, of which superfluidity, superconductivity, and low temperature physics in general are only three striking examples. Due to its structural simplicity, the helium atom provides an excellent opportunity of confronting high precision theory [40] with the results obtained from highly accurate experiments. Moreover, taking advantage of the internal atomic structure of helium, unique experiments like the first realization of a Bose-Einstein condensate with a metastable noble gas [71; 72] become possible.

This chapter briefly reviews some basic properties of helium atoms and presents the relevant energy levels along with the excitation scheme that was used in the experiment.

5.1 Basics

Helium atoms consist of two protons, two electrons, and a certain number of neutrons, where two of the eight known isotopes are stable: ^{4}He with a natural abundance of 99.99986% and the lighter ^{3}He with a natural abundance of 1.4×10^{-6} [73]. As the nuclear spin of $I = \frac{1}{2}$ for ^{3}He gives rise to a hyperfinestructure, while ^{4}He does not have nuclear spin (i.e. $I = 0$), the energy level structures for these isotopes exhibit pronounced differences [44].

This experiment was carried out with high-purity grade ^{4}He so that just He can be written in the following chapters without ambiguities. Electronic configurations will henceforth be expressed using the term symbol $n\,^{2S+1}\mathrm{L}_J$, where n and L are the principal and the angular quantum number, respectively. The fine structure arising from the spin-orbit coupling requires introducing the total angular quantum number J, while $2S+1$ describes the spin multiplicity. Since the selection rules forbid transitions between different spin-multiplets, the energy level diagram for He can be split in a singlet (total electron spin $S = 0$) and a triplet ($S = 1$) part.

Figure 5.1(a) shows the first levels of the triplet energy level diagram. The ground state $1\,^1\mathrm{S}_0$ of helium is extremely stable. Therefore, the first allowed transition for electric dipole radiation to the $2\,^1\mathrm{P}_1$ state (not shown in Figure 5.1(a)) requires 58 nm radiation and is thus essentially impracticable for optical excitation. However, the first excited state of triplet helium $2\,^3\mathrm{S}_1$ can be populated by means of a DC discharge (see 6.2). As a result of the optical selection rules, this state is metastable with a lifetime of about 7900 s,

the main decay process being a single photon magnetic dipole transition to the ground state [74; 75]. Metastable helium atoms, denoted He^* , carry a very high internal energy of 19.82 eV and can thus collisionally ionize any atom whose ionization energy is smaller than the internal energy of the metastables in a process called Penning ionization [76]

$$He^* + X \rightarrow He + X^+ + e^- \tag{5.1}$$

Only helium (24.59 eV) and neon (21.56 eV) in their ground state have ionization energies larger than the internal energy of He^* atoms.

5.2 Excitation Scheme

The three-level excitation scheme used in this experiment is illustrated in Figure 5.1(b)). On the time scale of the experiment, the metastable state can be considered the effective ground state $|1\rangle$. A frequency-doubled Ti:Sapph laser is used to drive the transition $2\,^3S_1 \rightarrow 3\,^3P_2$ at a vacuum wavelength of 388.9751 nm [40], and a second independent Ti:Sapph laser can be adjusted in its wavelength ($780 - 796$ nm) for the excitation from the intermediate state $|2\rangle$ to selected Rydberg states $n\,L_J$, also denoted $|3\rangle$.

Whereas the target state $|3\rangle$ has a lifetime on the order of μs, the intermediate state is much more short-lived and thus introduces the main losses due to spontaneous emission during the excitation process. There are two decay channels for the $3\,^3P_2$ state that have to be accounted for: Direct decay to the metastable ground state occurs at a rate given by the Einstein coefficient

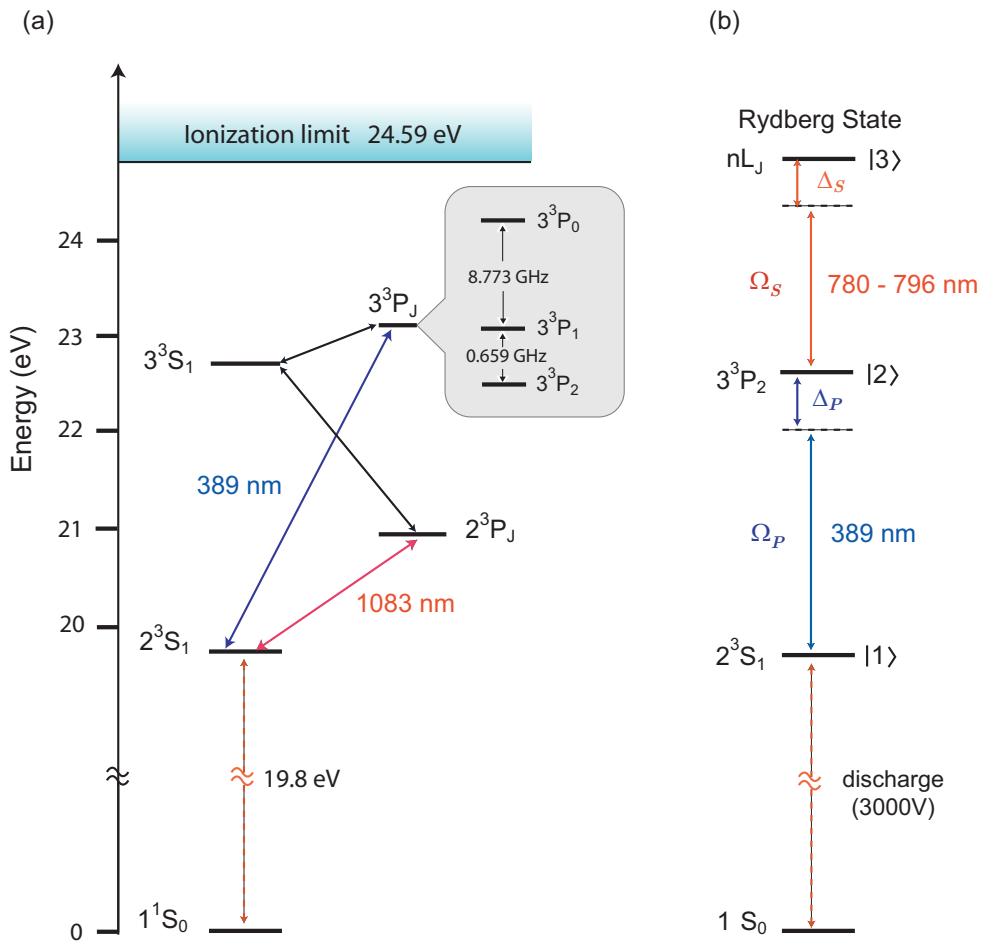

Figure 5.1 Energy level diagram of triplet helium: (a) relevant energy levels for the experiment (b) excitation scheme [43]

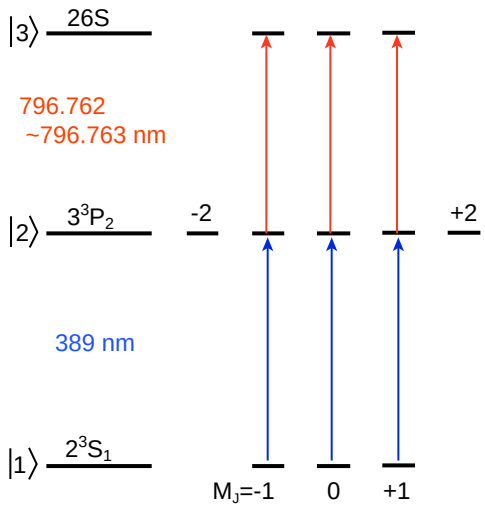

Figure 5.2 Excitation scheme of He^* from the $2\,^3S_1$ metastable ground state to the $26\,^3S_1$ Rydberg state for linearly polarized laser beams [43]

$A\,(3\,^3P_2 \rightarrow 2\,^3S_1) = (105.5\text{ ns})^{-1}$ [44], while the decay to the state 3^3S_1 with subsequent decay to the metastable state via the $2\,^3P_J$ states has an Einstein coefficient $A\,(3\,^3P_2 \rightarrow 3\,^3S_1) = (932.1\text{ ns})^{-1}$ [44]. Therefore, Equation (2.42) yields $\tau_2 = 94.8$ ns [44] as the lifetime of the intermediate state $|2\rangle$, which corresponds to an effective linewidth of $\frac{\Gamma_2}{2\pi} = 1.51$ MHz. With (2.43), the branching ratios become 89.83% and 10.17% for $3\,^3P_2$ and $2\,^3S_1$, respectively.

According to Equation (3.8), the Rabi frequency Ω_q of a transition depends on the polarization of the applied radiation field. Consider the substructure of the excitation scheme as shown in Figure 5.2, where the target state $|3\rangle$ has been specified to the $26\,^3S_1$ state that was used in all our experiments. If the first transition $|1\rangle \rightarrow |2\rangle$ is driven by σ^+-circularly polarized light ($q = 1$), all atoms will get optically pumped into the ground state sublevel $M_J = 1$ so

that the relevant transition becomes $M_J = 1 \rightarrow M'_J = 2$ whose dipole matrix element can be calculated using (3.11) after explicit evaluation of the 3j and 6j symbols [43; 56].

$$\left\langle 3\,^3P_2, M'_J = 2\right| r_1 \left|2\,^3S_1, M_J = 1\right\rangle = \sqrt{\frac{1}{3}}\ \langle 3P \| \, r \, \| 2S \rangle \tag{5.2}$$

The value of the reduced dipole matrix element is $\langle 3P \| \, r_1 \, \| 2S \rangle = 0.9 a_0$ [43], and hence Equation 5.2 yields both the lifetime of the upper state and the saturation parameter s_0 of the transistion, which are given in Appendix B.

Since both laser beams used for the two-step excitation process in our experiment are linearly polarized ($q = 0$), three possible cases for which $\Delta M_J = 0$ have to be distinguished. The matrix elements (3.11) can be written as [43]

$$\left\langle 3\,^3P_2 M'_J\right| r_0 \left|2\,^3S_1 M_J\right\rangle = \beta \cdot \sqrt{\frac{1}{3}}\ \langle 3P \| \, r \, \| 2S \rangle \tag{5.3}$$

where β takes the values $\beta = \sqrt{\frac{2}{3}}$ for $M_J = 0$ and $\beta = \sqrt{\frac{1}{2}}$ for $M_J = \pm 1$, respectively. Therefore, the relation $\Omega_0 \left(M_J\right) = \beta \left(M_J\right) \Omega_1$ is valid. However, since $\beta \left(M_J\right)$ is approximately the same for all ΔM_J, an average Rabi frequency for the case of linear polarization case can be taken to be $\Omega_0 \approx 0.75\ \Omega_1$. If the intensity I of the applied radiation field is known, the Rabi frequency Ω_q can be determined with (3.13).

A similar treatment of the dipole matrix elements for the second transition $|2\rangle \rightarrow |3\rangle$ together with the reduced matrix element $\langle 26S \| \, r_1 \, \| 3P \rangle = 0.079 a_0$ [43] yields the lifetime of the target Rydberg state $26\,^3S_1$ to be $\sim 40\ \mu$s.

Chapter 6

Vacuum System

6.1 Introduction

Our home-built vacuum system consists of three main chambers: Metastable helium atoms are created in the source chamber, excited to a selected Rydberg state in the interaction chamber, and their spatial distribution is measured in the detection chamber. The basic layout of the vacuum system is shown in Figure 6.1.

The source and the interaction chambers are welded aluminum cubes of 30 cm and 25 cm side length, respectively. The covers of both cubes are made of plexiglass and thus allow the correct operation of the discharge source to be monitored visually. Since both chambers are connected through a slit and a skimmer, they cannot be isolated from each other and must always be brought to air simultaneously. The detection chamber is located approximately 175 cm further downstream the beamline (4" diameter) and mainly created by a six-way-cross (tube diameter 4"). One horizontal end of this six-way-

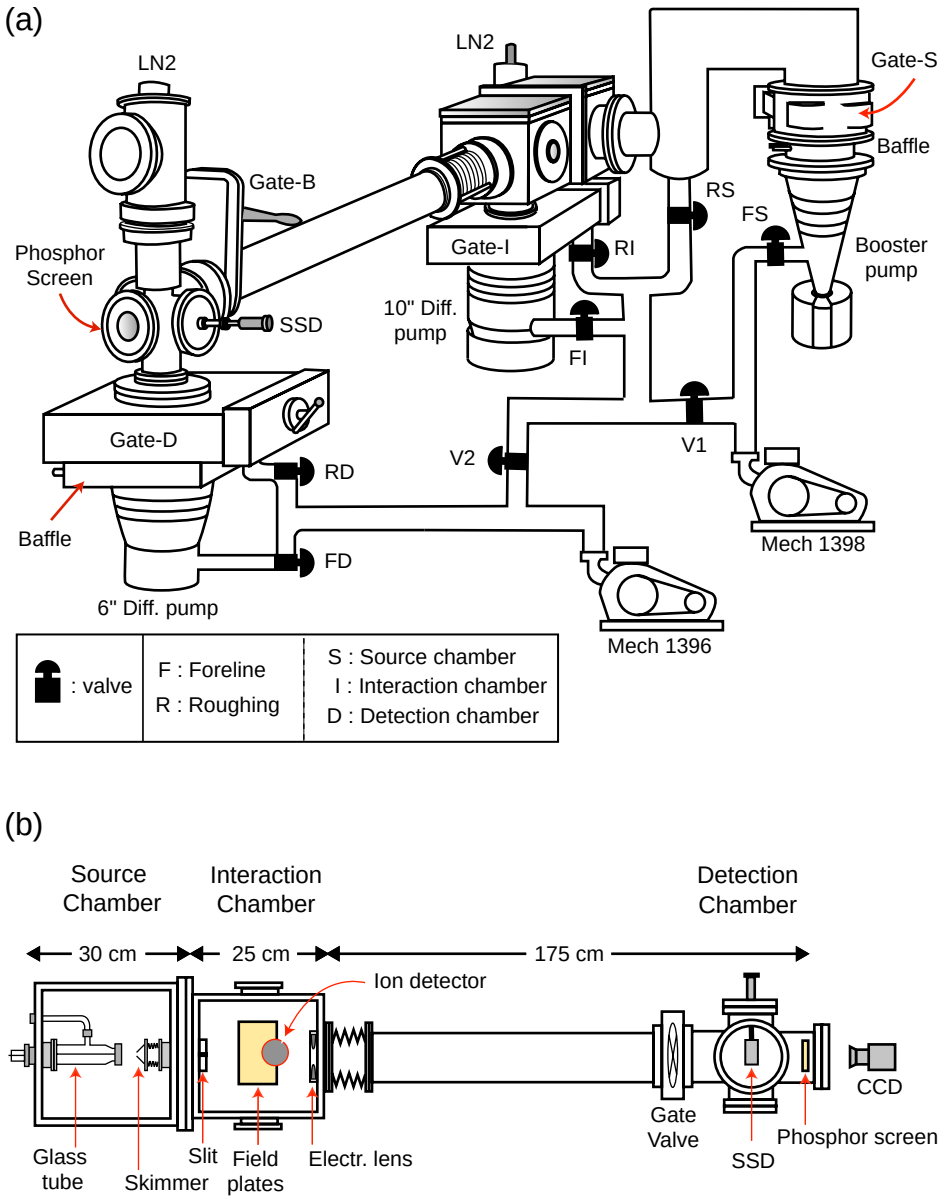

Figure 6.1 Vacuum system : (a) 3D schematic, (b) top view of source, interaction, and detection chamber [43]

cross is occupied by a stainless steel detector (SSD, see 6.4.3) that allows us to spatially profile the atomic beam, whereas the upper end is connected to a liquid nitrogen trap.

Three diffusion pumps constitute a moderate differential pumping system to guarantee a permanent gas flow from the source chamber to the detection chamber: The source chamber is pumped by an Edwards 9B3 booster pump (pumping speed 850 l/s) which was chosen because it operates efficiently at high flow rates and in higher pressures ($\sim 10^{-5}$ Torr) [43]. An NRC/Varian HS-10 10" diffusion pump (4200 l/s) and a CVC/Bendix PBA-100A 6"-diffusion pump (1500 l/s) pump on the interaction and the detection chamber, respectively. During operation, the booster pump is backed by a Welch Duo-Seal 1398 mechanical pump (1500 l/min), while a Welch Duo-Seal 1396 (2800 l/min) mechanical pump acts as a backing pump for the interaction and detection chamber.

The vacuum system was constructed such that the system can be vented with the diffusion pumps still turned on. In order to do so, each diffusion pump can be isolated from the vacuum system by a gate valve: Two CVC/VCSP-61B six inch gate valves are used for the source and the detection chamber, respectively (**Gate-S** and **Gate-D** in Figure 6.1, and a VRC 9457B-301 ten inch gate valve is employed for the interaction chamber (**Gate-I**). An additional gate valve **Gate-B** (Vacuum Research Manufacturing Company, Model unknown) isolates the detection area from the interaction chamber. Between the vacuum chambers and both the 6" pump and the booster pump there are

water baffles that condense oil vapour rising towards the vacuum chamber to prevent contamination by diffusion pump oil. All three pumps and the two baffles are supplied with cooling water. Ion gauges (Kurt J. Lesker, models G100K and G075K) monitor the pressures in the three different vacuum chambers, whereas Veeco and Kurt J. Lesker thermocouple gauges are used to monitor the pressure in the foreline of the vacuum system.

Separate fail safe systems were constructed to protect the whole vacuum system against unwanted perturbations. They automatically shut the diffusion pumps off, if either the foreline pressure increases to more than 50 mTorr, the cooling water flow decreases below the setpoint value, or the temperature of the diffusion pump exceeds the critical value.

Typical pressures in our vacuum system (with no gas flow to the source) are 10^{-5} Torr in the source chamber, 2×10^{-6} Torr in the interaction chamber, and 8×10^{-7} Torr in the detection chamber.

Since any imperfection of the gate valves, e.g. due to aging effects, can cause an oil contamination of the vacuum chamber, we usually turn the pumps off and let them cool down for approximately 3 hours whenever we have to break vacuum. An instructional manual on how to operate the vacuum system can be found in Appendix C.

6.2 Source

Our source for metastable helium atoms belongs to the category of cryogenically cooled supersonic free expansion jet sources and was designed following

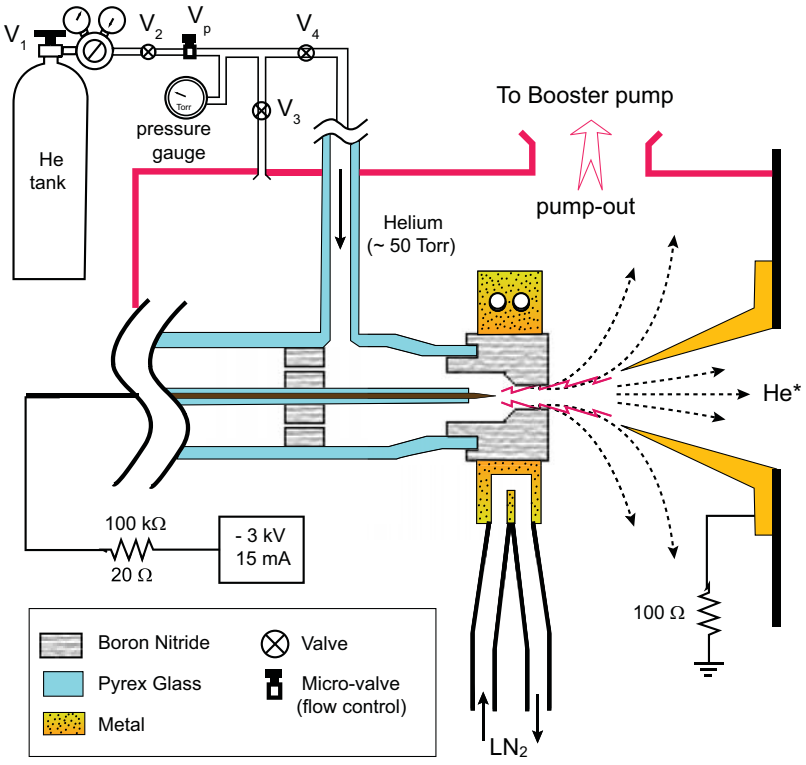

Figure 6.2 Metastable helium source

the proposal of Fahey *et al.* [77]. The general idea is that metastables are created by a DC discharge in moderate pressure He gas and then freely expand into a region of lower pressure through a small size aperture. If the pressure difference is large enough the flow of metastables will be supersonic, and usually a skimmer with a small size hole is used directly downstream to select the atoms out of the region of supersonic flow.

A schematic of our source is shown in Figure 6.2. The main element of the source is a Pyrex glass tube. Both ends of the glass tube (diameter 25 mm, length $\sim$ 135 mm) are sealed with caps made of boron nitride (BN)

that were custom machined out of a 1" diameter rod and then glued to the tube with Aremco Inc. *Ceramabond 503*. A hole of 150 μm diameter and 1 mm length was drilled into the front cap, and a thin glass tube (diameter 5 mm) was fed through the back cap (not shown in Figure 6.2) in order to guide a tungsten needle to the nozzle in the front cap so that the tip of the needle is $\sim$ 1 mm apart from the nozzle. Approximately 2 cm downstream of the nozzle, a skimmer with a 1 mm hole was mounted on a translation stage that can be adjusted in three dimensions from outside the vacuum chamber in order to maximize the metastable efficiency during operation of the source. The skimmer is connected to the wall between source and interaction chamber.

The tungsten needle and the skimmer serve as cathode and anode for the DC discharge, respectively. To start the discharge, -3 kV are supplied to the needle, while the skimmer is at ground potential. The background gas gets field-ionized in the high field regions and forms a discharge plasma consisting of both He ions, He* atoms and other excited states of He. Nearly all metastables are quenched by collisions in the discharge region [78], but secondary electrons that are a by-product of the discharge excite a considerable fraction of He atoms to the metastable state again outside the discharge region where the density is lower and therefore collisions are less likely.

An intrinsic drawback of the discharge source is that the He atoms are heated to $500 - 600$ K, and therefore, both less He* is created because of Penning ionization [76], which mainly depends on the He* collision rate, and the transverse velocity spread of the beam is increased. To compensate for these

effects, the front cap of the discharge glass tube is in thermal contact with a copper jacket cooled by liquid nitrogen. Due to this feature of the source, BN was chosen as the material for the caps, because it combines low electric conductivity ($\sim 10^{-15}\ \Omega^{-1}\ \mathrm{cm}^{-1}$) [79], which is important for the correct operation of the discharge, and high thermal conductivity ($\sim 27 - 31\ \mathrm{Wm}^{-1}\mathrm{K}^{-1}$) [79], which is required for effective cooling. Cooling with liquid nitrogen instead of water reduces the transverse velocity spread by a factor of 2 [80].

Our source runs in a current limiting mode – realized by a 100 kΩ power resistor (20 W, OHMITE B20J100K) in series with the source circuit – to protect the high-voltage power supply for the discharge. The current limit can be altered up to 20 mA to optimize the flux of metastables measured by either the ion or the phosphor screen detector. The best source efficiency is usually achieved for a current limit between $8 - 10$ mA.

With source gas flowing, the pressures in the source and the interaction chamber are 50 Torr and 10^{-5} Torr, respectively, so that the expansion is slightly supersonic. Under the best operating conditions, our source yields $\sim 10^{14}\ \frac{\mathrm{He^*\ atoms}}{sr \cdot s}$ with a metastable ratio of 10^{-5} and a longitudinal velocity in the range of $1440 - 1555\ \frac{\mathrm{m}}{\mathrm{s}}$. Careful measurements [81] show that at least 98% of the metastables are in the triplet $2\ ^3\mathrm{S}_1$ state so that unwanted background effects originating from singlet $2\ ^1\mathrm{S}_1$ metastables are negligible.

6.2.1 Longitudinal Velocity Distribution

The longitudinal velocity distribution of the atomic beam was characterized in a time-of-flight (TOF) measurement by Widmer and Bellanca [81; 82]. Inserted into the beamline directly behind the collimating slit, a mechanical chopper wheel acted as a fast shutter that bunched the atomic beam into groups of atoms that had passed the shutter within a narrow time window. Therefore, measuring the arrival times of these atoms at a fixed distance from the chopper wheel (~ 2 m) yields the longitudinal velocity distribution of the atomic beam.

In the experiment carried out by Bellanca [82], a previous version of the current stainless steel detector (see 6.4.3) was used in a modified configuration where the Keithley 486 picoammeter was replaced by a 10 kΩ resistor in parallel with a Stanford Research Systems SR560 low-noise pre-amplifier whose output signal was monitored on a Tektronix TDK 210 digital oscilloscope. The TOF measurements were triggered by an external Helium-Neon laser incident on a photodiode that was positioned directly behind the chopper wheel. Figure 6.3 shows a typical result of such a measurement: The first peak is caused by UV photons from the source discharge whereas the second peak originates from the metastables. After optimization of the parameters discharge current and inlet pressure, a Gaussian fit of the data (dashed line) yields an average longitudinal velocity of $v_{\text{long}} = 1493\ \frac{\text{m}}{\text{s}}$ and a velocity spread of $\Delta v = 465\ \frac{\text{m}}{\text{s}}$. These values constitute a compromise between a narrow longitudinal velocity distribution and a high He^* count.

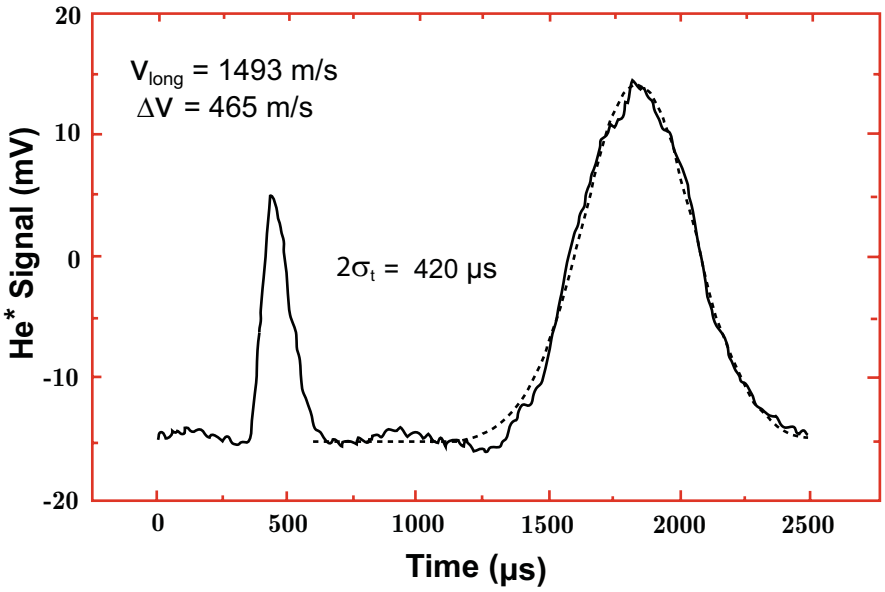

Figure 6.3 Velocity distribution of He^* atoms determined in a time-of-flight (TOF) measurement. The two peaks are caused by UV photons and He^* atoms, respectively. [82; 43].

6.3 Interaction Chamber

The atomic beam enters the interaction chamber through a slit in the wall separating source and interaction chamber. The slit (width: 0.5 mm, height: 2 mm) was mounted on an assembly that can be moved in the direction perpendicular to the atomic beam with with a flexible motion feed-through so that possible reductions in beam intensity as a result a change of the beam direction, which might occur after cleaning or replacing the glass tube, can be compensated for.

Figure 6.4 (a) depicts the interior of the interaction chamber. Two electric field plates, whose dimensions are shown in Figure 6.4 (b), are located in the

center of the chamber with their short side aligned approximately parallel to the atomic beam. Two windows (diameter 3"), anti-reflection coated for both 389 nm and 795 nm light, are embedded in the sides of the interaction chamber so that the laser beams used for the excitation process traverse can the chamber and the field plates perpendicularly to the atomic beam without considerable losses.

An ion detector was placed close to the downstream edge of the upper field plate to monitor the number of created Rydberg atoms during the experiment. Detailed information about the detector can be found in 6.4.1.

Approximately 2 cm further downstream from the field plates, an electrostatic hexapole lens (see Chapter 4) was positioned with its center roughly coinciding with the atomic beam in order to focus the created He Rydberg atoms. During the experiment, the voltages for the lens, the field plates and the MCPs in the ion detector are supplied into the interaction chamber via BNC connectors that are implemented in the vacuum blank-offs. Similarly, the signal from the ion detector is read out to an oscilloscope through a BNC cable.

6.4 Detection Systems

Three different detection systems are used in our system to measure the efficiency of the excitation of He^* atoms to a selected Rydberg state and the spatial distribution of the atomic beam: an ion detector placed at the edge of the upper field plate in the interaction chamber, a stainless steel detector

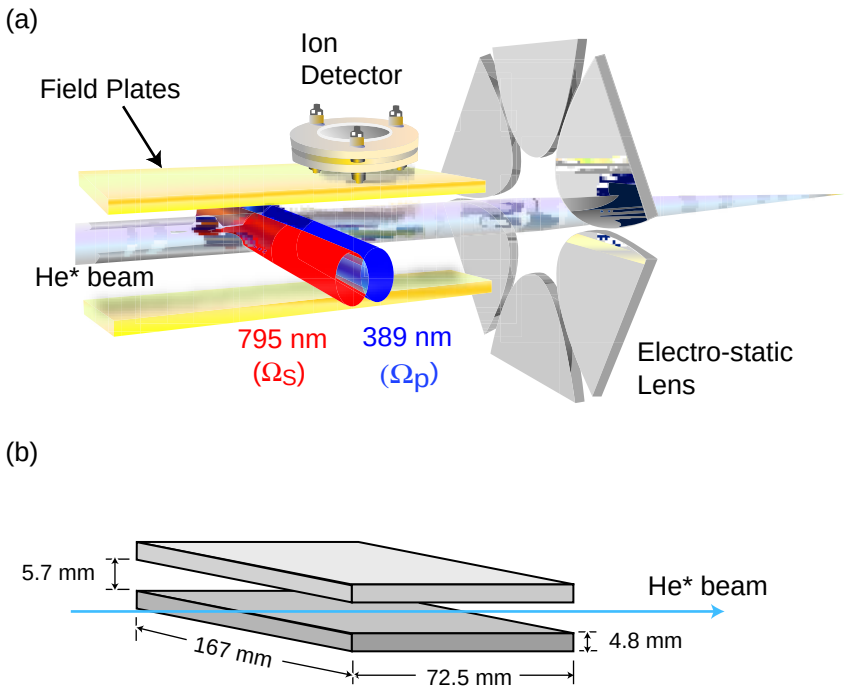

Figure 6.4 Interaction Chamber: (a) configuration of atomic beam, laser beams, field plates, ion detector and electrostatic lens (b) dimensions of field plates [43]

located in the 6-way cross $\sim$ 2 m downstream the beamline, and a phosphor screen detector sitting at the very end of the beamline. All three detectors contain microchannel plates (MCPs) for amplification of the incident signal [83]. Since both the ion detector and the stainless steel detector include two MCPs in Chevron^{TM} configuration, a suitable MCP for this purpose (BURLE Technologies, Inc. MCP 25/25/12 D 40:1) with 25 mm diameter, 10 μm pore size and a bias angle of 12 $^\circ$ was chosen to be used in all detectors. At the maximum bias voltage (1000 V), this MCP provides a maximum gain of 4×10^3.

6.4.1 Ion Detector

Rydberg atoms produced in the interaction area can be ionized by collisions with the background gas. Since the number of ions is related to the number of Rydberg atoms, the excitation efficiency can be monitored with our ion detector whose schematic is shown in Figure 6.5 (a). An acceleration voltage of -2000 V attracts the created ions to the first MCP where their impact creates an electron shower. Due to the potential difference, these secondary electrons are further accelerated to the second MCP -1000 V, which serves as a second amplification stage. The combined gain of the two MCPs in our ion detector amounts to $\sim 10^6$. A metal anode behind the second MCP collects the electrons, and the resulting current is subsequently amplified and transformed into a voltage signal that can be observed with an oscilloscope (Tektronix TDK210) if the excitation frequency is resonant with the atomic transition during the scan of the electric field plates. Figure 6.5 (b) shows the ion signal for the transition to the 26S Stark level at an electric field of 30 $\frac{\text{V}}{\text{cm}}$.

6.4.2 Phosphor Screen Detector (PSD)

Our phosphor screen detector (PSD) provides a real time image of the spatial distribution of He^* atoms. Its schematic is shown in Figure 6.6 (a). Due to their high internal energy (19.8 eV), metastables incident on the MCP produce an electron shower which subsequently strikes a phosphor screen. The electrons cause the phosphor to fluoresce, and since the light emission for the type P-20 phosphor used in our detector is in the visible range ($470 - 670$ nm,

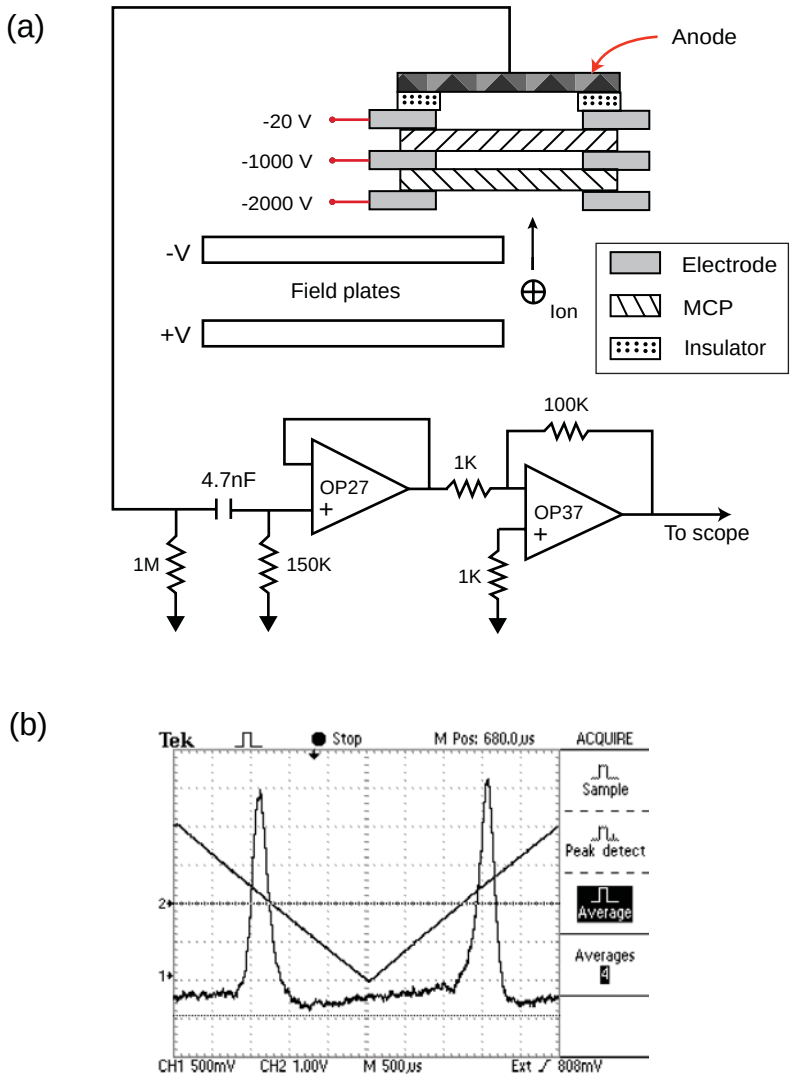

Figure 6.5 Ion detector: (a) schematic including amplification circuit (b) Ion signal (scan amplitude of lower field plate: 5 V, upper field plate potential: −10 V, Rydberg state: 26S, Electric field: 30 Vcm^{-1}) [43]

peaking typically at 550 nm), a real time image of the spatial distribution of the atomic beam can be observed with a regular CCD camera (Dage-MTI CCD100) trough a flanged window. The camera is connected to a computer via a Dage-MTI Investigater and a video card (ASUSTeK Computer, Inc. AGP-7700 Deluxe v6.49), and the ASUSTeK Computer, Inc. Asus Live Version 4.6 software is employed to both provide live images and take snapshots. The major drawback of the PSD is that its sensitivity is non-linear and non-uniform [84] because the parts of the screen that are frequently exposed to the beam age faster, therefore lose efficiency and in some cases even get completely burned. Although quantitative measurements are nearly impossible, however, the PSD still serves as an important tool to optimize the alignment in our system: The effects of adjusting beam height and direction as well as source current and skimmer position can be seen directly. In addition, the PSD enables us to set the frequency of the blue laser to the correct transition, because the strongest radiative pushing effect can be observed for the transition to the $3\,^3P_2$ state. This effect is weaker for the transitions to the other fine structure levels and completely absent when locking the laser to a cross-over peak. Figure 6.6 (b) shows a typical image of the atomic beam taken with the PSD and the CCD camera.

6.4.3 Stainless Steel Detector

A stainless steel detector (SSD) for the detection of He^* usually consists of an assembly of a metal front plate with a small aperture in it and a stainless steel

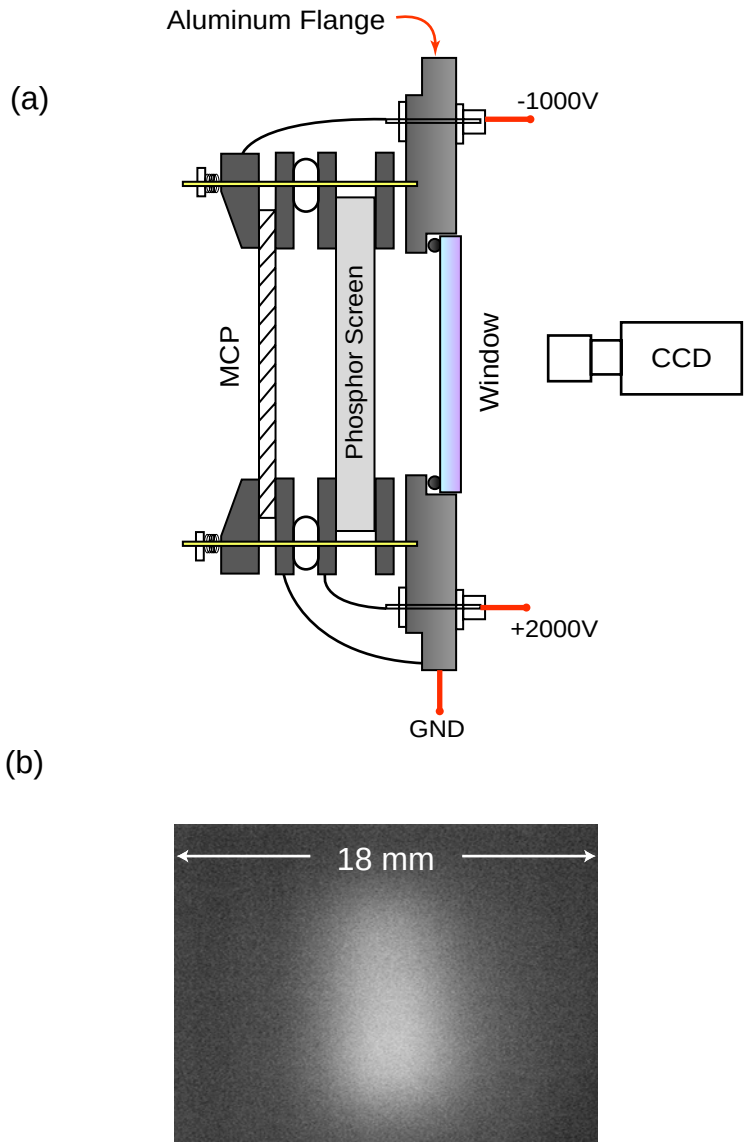

Figure 6.6 Phosphor Screen Detector (PSD): (a) schematic (b) typical image of the atomic beam on the phosphor screen (1700 V) from the CCD camera for an MCP voltage of −900 V and an inlet pressure of 50 Torr [43]

back plate. Metastables passing the aperture in the front plate hit the back plate and release their internal energy in the collisions. As the internal energy of He^* (19.8 eV) is larger than the work function of the metal ($4.7 - 5.6$ eV [85], electrons are liberated and then collected by the front plate which is at a comparatively positive potential. Since the efficiency of 70 % for the liberation of electrons from stainless steel by He^* atoms is known [86], the current signal measured at the front plate is directly proportional to the He^* flux integrated over the area of the aperture of the front plate. Thus, this type of SSD is able to yield absolute numbers for the He^* flux in the beamline.

Figure 6.7 (a) indicates how our SSD differs from this general layout: In order to amplify the resulting current signal, an amplification stage consisting of two MCPs in Chevron^{TM} configuration working exactly the same way as the one used in the ion detector (see subsection 6.4.1) was added. The current signal at the aluminum anode is metered with a Keithley 486 picoammeter. The SSD was reintegrated into the system for quantitative measurements of the horizontal spatial distribution of the atomic beam. Therefore, the whole detector was mounted on a Huntington Mechanical Laboratories, Inc. 2-inch linear motion feedthrough L-2111-2 and attached to one of the side flanges of the 6-way cross in the detection area. The only modification of the SSD in comparison to previous experiments [81; 82] was a change in the slit size (currently fixed at ~ 300 μm).

Although this modified type of SSD does not allow absolute measures of the He^* flux, it does yield a position dependent current signal proportional to

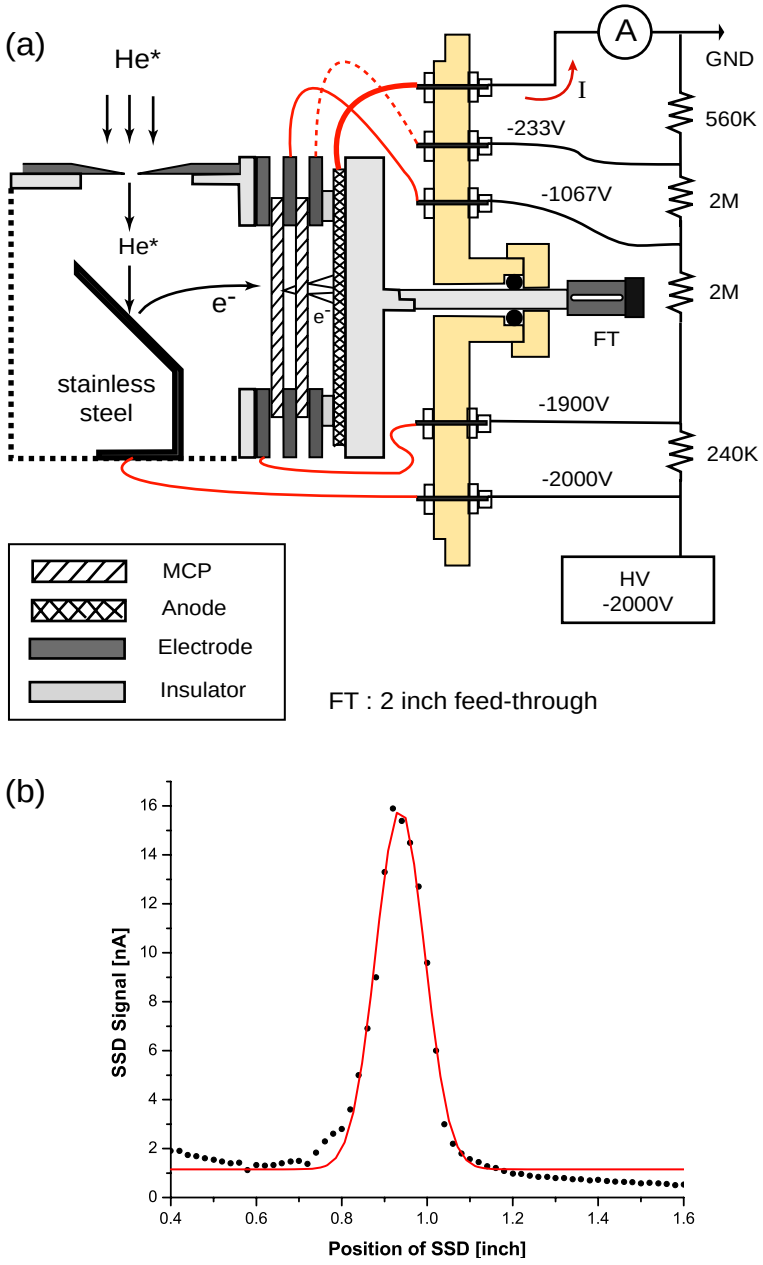

Figure 6.7 Stainless steel detector (SSD): (a) schematic (b) current signal from SSD measured with a Keithley 486 pico-ammeter showing an atomic beam profile [43]

the He^* flux and thus makes quantitative horizontal beam profiles possible. One advantage of the SSD is that it does not suffer from a background due to He ground state atoms, because their kinetic energy ((0.05 eV at 1600 $\frac{m}{s}$ is not sufficient to liberate electrons. However, Figure 6.7 (b) shows that a background of typically $1-2$ nA ($\sim 5-10$ % of the usual peak intensity) due to UV photons as a by-product of the discharge source has to be accounted for.

Chapter 7

Laser Systems

Two independent Titanium-doped Sapphire (Ti:Sapph) laser systems produce the red ($785 - 796$ nm) and the blue (frequency doubled 777.95 nm light at 389 nm) light for the experiment. In order to stabilize both lasers against external vibrations, three different techniques are applied: The Ti:Sapph laser for the creation of the blue light (which will hereafter be referred to as the "blue laser") is first locked to a stable reference cavity employing the Pound-Drever-Hall (PDH) locking scheme [87; 88] (see 7.1.1. Second, to get rid of long term changes, e.g. temperature drifts, the reference cavity itself is stabilized to an atomic transition using Doppler-free saturation absorption spectroscopy (SAS) [89; 90] (see 7.1.2. For the other Ti:Sapph laser ("red laser"), such a precise frequency stability is not coercibly necessary. Yet, the PDH technique was implemented to complement the internal intensity locking system of the laser. Furthermore, the frequency doubling cavity in the blue laser system is independently stabilized employing the modulation-free Hänsch-Couillaud (HC) locking technique [91] (see 7.1.3).

7.1 Blue Laser

The optical scheme of the blue laser system is shown in Figure 7.1. A diode-pumped frequency doubled Nd:YVO_4 solid state laser (Coherent Verdi V10) with a maximum output power of 10.5 W at a wavelength of 532 nm pumps a Schwartz Electro-Optics, Inc. Titan CWR 760 Ti:Sapph laser which currently gives a single mode output power of 2.5 W at 777.95 nm. Under optimized conditions, the maximum output power values reached up to 3.1 W. The laser cavity is set up in ring configuration to avoid spatial hole burning effects that occur for a standing wave configuration, because the active medium does not contribute to the lasing at the nodes of the wave. An optical diode (**OD**) in the ring cavity ensures unidirectional operation and thus prevents the laser from undesired optical feedback. Two mode selective elements inside the cavity both guarantee single mode operation and allow tuning the wavelength: A birefringent filter (**BF**) and a thick etalon are used to adjust the wavelength in the range of $10^{-2} - 10^{1}$ nm and $10^{-4} - 10^{-3}$ nm, respectively (at 778 nm, 10^{-3} nm correspond to 500 MHz). A beam splitter (**BS**) divides two low power beams off the output beam of the Ti:Sapph laser. The first one goes to a stable Fabry-Perot cavity that the laser will be locked to with the PDH technique and that is therefore also referred to as PDH cavity. The second one is split again and guided to a Burleigh WA-1500 wavemeter to coarsely monitor the wavelength and to another Fabry-Perot cavity that is used to observe the mode structure of the Ti:Sapph laser. The main beam is frequency doubled in a resonant frequency doubling cavity, which is independently stabilized using

the HC locking technqiue, and then sent to the interaction chamber through a single mode optical fiber. Part of the created blue light is split off the main beam before the fiber coupler for a Doppler-free saturation absorption spectroscopy setup that provides a stable atomic reference that the PDH cavity can be locked to.

Extensive discussions of second harmonic generation (SHG) can be found in [43; 92; 93; 94]. The following sections will describe the different locking techniques in more detail. Practical guidance for locking the blue laser is given in Section C.3.

7.1.1 Pound-Drever-Hall Locking Technique

To gain short term stability of the Ti:Sapph laser frequency, the Pound-Drever-Hall locking technique, which was originally invented by Pound [87] to lock microwave oscillators to a stable reference cavity and later transferred to the optical regime by Drever and Hall [88], is applied. The crucial point for effective frequency locking to the transmission or reflection peaks of a cavity is to obtain information about the phase of the transmitted or reflected light, because nothing but the phase will tell whether the frequency of the laser is below or above the resonance frequency. The general idea behind the PDH scheme is to extract this phase information from the reflected light of a Fabry-Perot cavity by interfering it with phase modulated light.

The reflection coefficient for a Fabry-Perot cavity with lossy mirrors is [95]

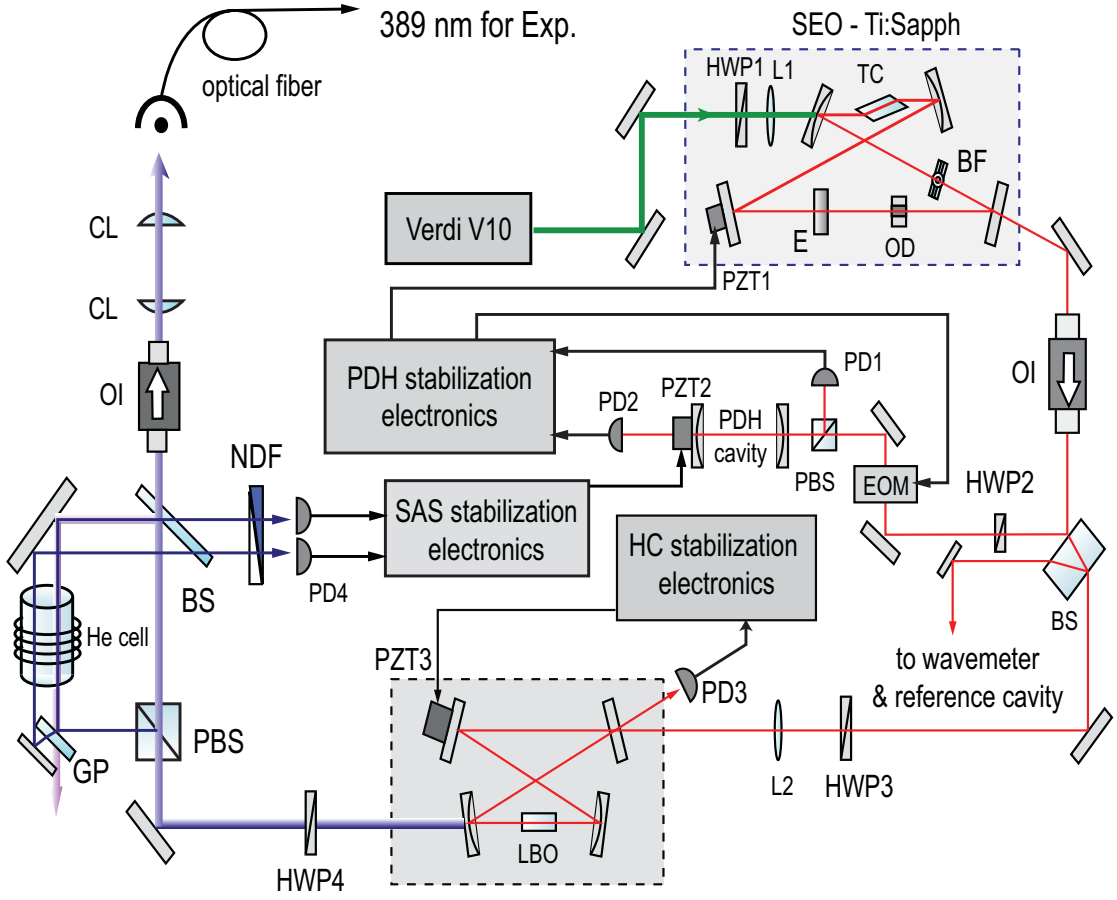

HWP : half-wave plate	BS : beam splitter	HC : Hänsch-Couillaud
L : lens	EOM : electro-optical modulator	LBO : LBO crystal
TC : Ti:Sapphire crystal	PBS : polarizing beam splitter	GP : glass plate
E : etalon	PD : photo diode detector	NDF : neutral density filter
OD : optical diode	PZT : piezo-electric transducer	CL : cylindrical lens
BF : birefringent filter	PDH : Pound-Drever-Hall	
OI : optical isolator	SAS : saturation absorption spectroscopy	

Figure 7.1 Optical schematic of the blue laser system (a schematic of the Hänsch-Couillaud optics is shown in Figure 7.6) [43]

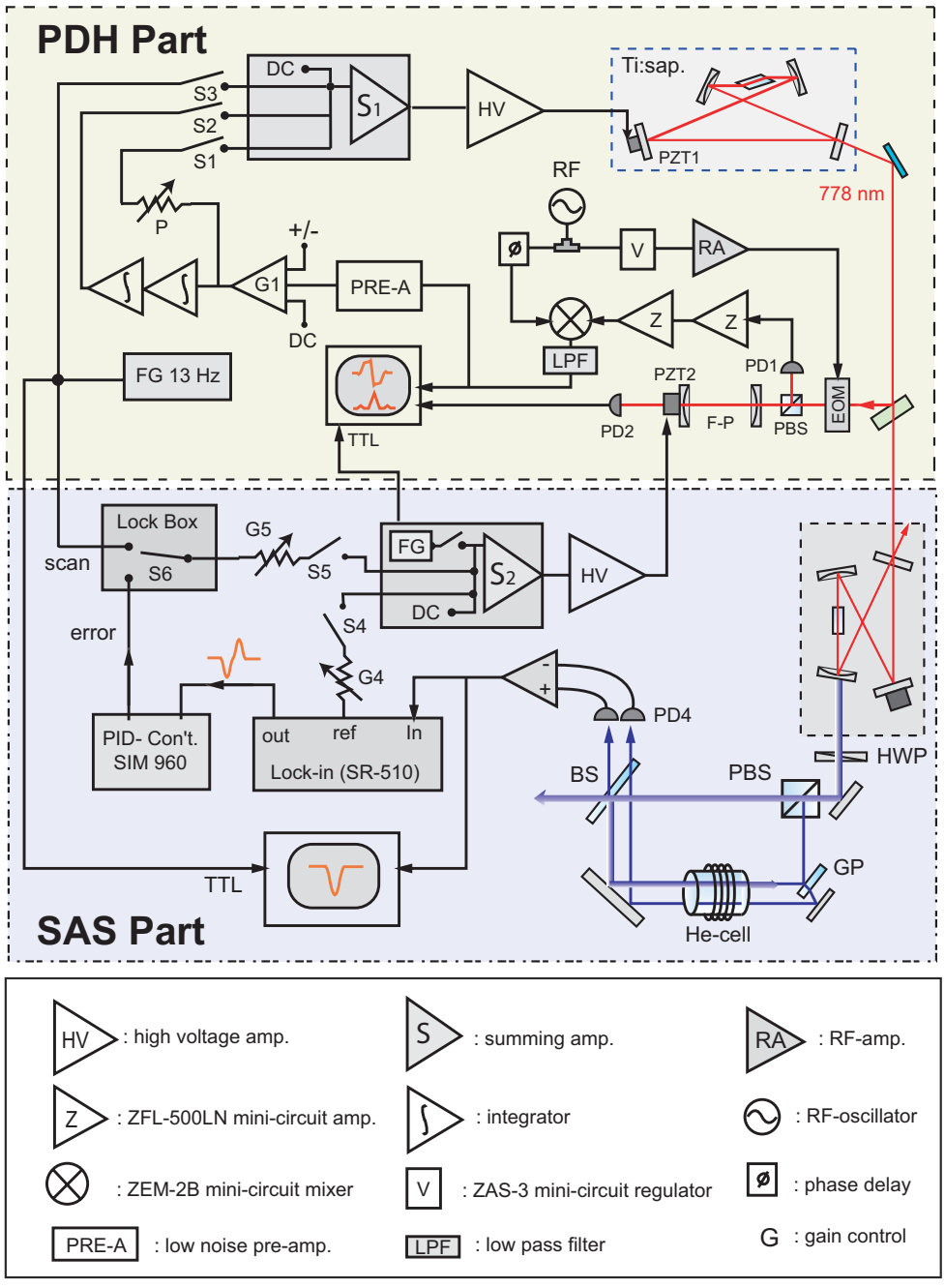

Figure 7.2 Stabilization electronics for the blue laser system (the Hänsch-Couillaud part is shown in Figure 7.7) [43]

$$F(\omega) = \frac{E_{ref}}{E_{inc}} = \frac{-r_1 + r_2 + (r_1^2 + t_1^2)\, e^{i\frac{\omega}{\Delta\nu_{\rm fsr}}}}{1 - r_1 r_2 e^{i\frac{\omega}{\Delta\nu_{\rm fsr}}}} \tag{7.1}$$

where E_{inc} and E_{ref} are the amplitudes of the incident and the reflected light waves at angular frequency ω, respectively, r_1, r_2 are the amplitude reflection coefficients of the front and back mirrors, respectively, t_1 is the amplitude transmission coefficient of the front mirror, and $\Delta\nu_{\rm fsr}$ is the free spectral range of the Fabry-Perot. The reflected beam E_{ref} is the coherent sum of the promptly reflected beam, which is backreflected from the front mirror and never enters the cavity, and the so-called leakage beam, which is the small part of the standing wave inside the cavity that leaks back through the front mirror. Both beams have the same frequency ω, but on resonance their phase differs exactly by π. If the promptly reflected beam and the leakage beam have the same intensity, they will interfere destructively so that the reflected intensity vanishes on resonance. In that case, $r_1\left[1 - r_2^2\left(r_1^2 + r_2^2\right)\right] = t_1^2 r_2$, and the cavity is called *critically coupled* [95]. If the leakage beam is too weak (strong) to cancel the promptly reflected beam, the cavity is *undercoupled* (*overcoupled*). Just off resonance, the phase difference between the two beams is not exactly π so that they will not cancel each other even for a critically coupled cavity. In order to determine the phase of the remaining reflected light, a phase reference is required.

The PDH scheme employs an electro-optic modulator (EOM), whose principle of operation is based on the optical Pockels effect, to create this phase reference. The EOM modulates the incident light at carrier frequency ω_c with

radio frequency (rf) Ω

$$E_{inc}(t) = E_0 e^{i(\omega_c t + \beta \sin \Omega t)} \tag{7.2}$$

which can be expanded into a Fourier series

$$E_{inc}(t) = E_0\, e^{i\omega_c t} \sum_{n=-\infty}^{\infty} J_n(M)\ e^{in\Omega t} \tag{7.3}$$

Here, the $J_n(\beta)$ are the Bessel functions, and β is the so-called modulation depth. For $\beta \ll 1$, all terms except $n = -1,\ 0,\ 1$ can be neglected and (7.3) becomes

$$E_{inc}(t) \approx E_0 \left[J_0(\beta)\, e^{i\omega_c t} + J_1(\beta)\, e^{i(\omega_c+\Omega)t} - J_1(\beta)\, e^{i(\omega_c-\Omega)} \right] \tag{7.4}$$

(7.4) shows that the light incident on the Fabry-Perot cavity contains three different frequency components: the carrier frequency ω_c and two sidebands at $\omega_c \pm \Omega$ (see the bottom of Figure 7.3). If the modulation depth is small enough ($\beta \ll 1$), almost all the power will be in the carrier and in the first order sidebands. These sidebands set a phase standard for measuring the phase of the reflected light from the Fabry-Perot, because interfering the sidebands with the reflected beam will produce a beat pattern at the modulation frequency from which the phase can be determined. Combining (7.1) and (7.4) yields

$$\begin{aligned} E_{ref}(t) = E_0 \big[& F(\omega_c)\, J_0(\beta)\ e^{i\omega_c t} \\ & + F(\omega_c + \Omega)\, J_1(F)\ e^{i(\omega_c+\Omega)t} \\ & - F(\omega_c - \Omega)\, J_{-1}(\beta)\ e^{i(\omega_c-\Omega)t} \big] \end{aligned} \tag{7.5}$$

A photodiode measures the intensity of the reflected light, which is just given

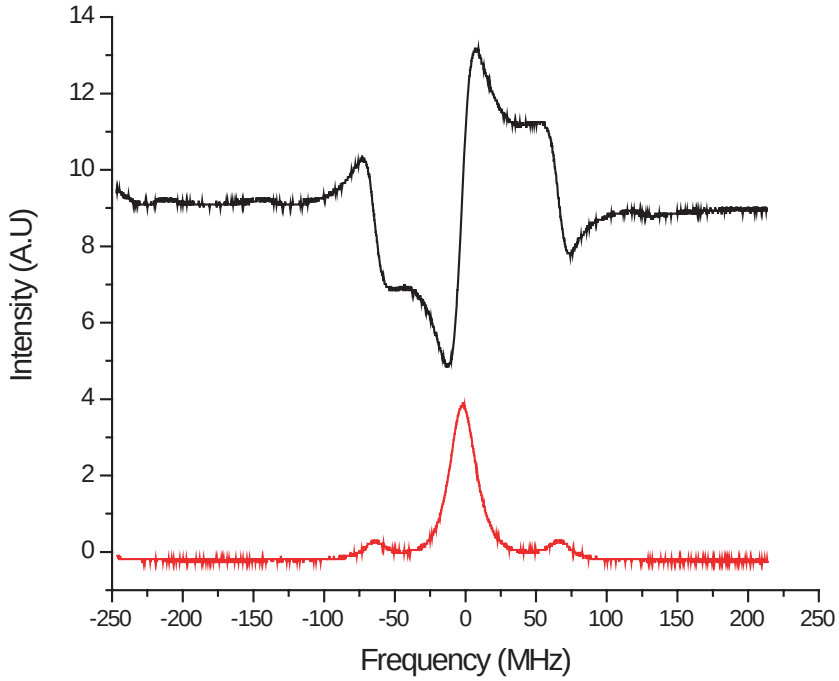

Figure 7.3 Pound-Drever-Hall (PDH) signals: error signal (top) and transmission signal (bottom)

by $P_{ref} = |E_{ref}|^2$, or after some algebra [95]

$$\begin{aligned} P_{ref} = & P_c \left|F\left(\omega_c\right)\right|^2 + P_s \left[\left|F\left(\omega_c + \Omega\right)\right|^2 + \left|F\left(\omega_c - \Omega\right)\right|^2\right] \\ & + 2\sqrt{P_c P_s}\left\{\mathrm{Re}\left[F\left(\omega_c\right) F^*\left(\omega_c + \Omega\right) - F^*\left(\omega_c\right) F\left(\omega_c - \Omega\right)\right]\cos\Omega t\right. \\ & \left. + \mathrm{Im}\left[F\left(\omega_c\right) F^*\left(\omega_c + \Omega\right) - F^*\left(\omega_c\right) F\left(\omega_c - \Omega\right)\right]\sin\Omega t\right\} \\ & + \left(2\Omega \text{ terms}\right) \end{aligned} \tag{7.6}$$

(7.6) can be understood as a wave with a nominal frequency ω_c and an envelope showing a beat pattern with two frequencies. Whereas the 2Ω-terms are a result of the sidebands interfering with each other, the Ω-terms in (7.6) originate from the interference between the carrier and the sidebands and thus

contain the phase information about the reflected carrier. It turns out that depending on the modulation frequency Ω one of the sine and cosine terms always vanishes [95]. Only for slow modulation frequency ($\Omega \ll \frac{\Delta\nu_{\mathrm{fsr}}}{\mathcal{F}}$, where $\mathcal{F}$ is the finesse of the Fabry-Perot), the internal field of the cavity has enough time to build up and to respond.

A phase sensitive lock-in setup consisting of a mixer, a phase shifter and a low-pass filter or integrator can be used to extract the phase information from the 2Ω-terms in (7.6). The mixer multiplies its two inputs so that the output for two incoming sine waves of frequencies Ω and Ω', respectively, becomes

$$\sin\Omega t \cdot \sin\Omega' t = \frac{1}{2}\left[\cos\left(\Omega - \Omega'\right) t - \cos\left(\Omega + \Omega'\right) t\right] \tag{7.7}$$

If the two frequencies are equal, the difference frequency $(\Omega - \Omega')$ will vanish resulting in a dc signal which can easily be isolated from the sum frequency $(\Omega + \Omega')$ with a low-pass filter or integrator. The phase shifter is necessary to compensate for possible additional phase delays due to the different signal paths.

For high enough modulation frequencies Ω the sidebands will be totally reflected ($F\left(\omega_c \pm \Omega\right) \approx -1$) if the carrier is close to resonance with the cavity. In that case, only the imaginary part of (7.6) matters, and the lock-in system produces an output

$$\varepsilon = -2\sqrt{P_c P_s}\mathrm{Im}\left[F\left(\omega_c\right) F^*\left(\omega_c + \Omega\right) - F^*\left(\omega_c\right) F\left(\omega_c - \Omega\right)\right] \tag{7.8}$$

This output signal contains all the phase information about the reflected light and therefore serves as an error signal. The typical shape of this PDH error

signal can be seen in the top part of Figure 7.3. Although the PDH locking technique is very powerful, noise in the error signal itself is indistinguishable from noise in the laser frequency, and the error signal is sensitive to power fluctuations in the sidebands [95].

The upper part of Figure 7.2 shows the setup of the stabilization electronics for the PDH feedback loop in our system. An rf oscillator **RF** supplies an rf frequency of $\Omega = 64$ MHz to an EOM via an rf amplifier **RA**. The modulated light is sent to a Fabry-Perot cavity (PDH cavity), where the intensity of the reflected and the transmitted light is detected by two fast SiPIN photodiodes **PD1** and **PD2**, respectively. Whereas the transmission signal is just sent to an oscilloscope, the reflection signal from **PD1** is processed by a phase sensitive lock-in amplification system. Subsequent to amplification by an rf amplifier (Mini Circuits ZFL-500LN), the signal is sent to a mixer (Mini Circuits ZEM-2B) whose other input is directly connected to the rf oscillator via a phase delay box (Ortec 425 Delay Module). The output of the mixer passes a low-pass filter, and the generated error signal is sent to a Princeton Applied Research low-noise preamplifier (Model 113) whose gain and cut-off frequency are optimized. After the polarity and the DC offset have been adjusted, the signal is separately fed to a two-stage integrator ($f_{3\mathrm{dB}} = 2$ Hz and ($f_{3\mathrm{dB}} = 0.5$ Hz)) and a proportional loop whose outputs are subsequently recombined in a summing junction. Passing through a high voltage amplifier, the PDH error signal is applied to **PZT1** inside the Ti:Sapph laser cavity.

7.1.2 Doppler-free Saturation Absorption Spectroscopy

Since the PDH cavity is subject to temperature drifts, another frequency standard is required to gain long term stability of the Ti:Sapph laser. Doppler-free saturation spectroscopy (SAS) [89; 90] is a technique which is commonly used for that purpose in atomic physics, because it employs atomic transitions as a uniquely stable frequency reference. Therefore, the Doppler-free absorption peak of the $2\ ^3S_1 \rightarrow 3\ ^3P_2$ transition of atomic helium (wavelength ~ 389 nm) provided by SAS (see Figure 7.4) is used to stabilize the PDH cavity and thus the Ti:Sapph laser.

If a laser beam of angular frequency ω traverses through a cell filled with a gas of low density, the transmitted intensity will be significantly lower at a frequency ω_0 corresponding to an electronic transition of the atoms in the gas cell. However, because the atoms are moving at different velocities, the Doppler effect broadens the transistion inhomogeneously. Except for very low temperatures, this Doppler-broadening $\Delta\omega_D$ is much bigger than the natural linewidth Γ of the transition and therefore the dominating feature in an absorption spectrum of an atomic gas.

As the name suggests, the crucial feature of SAS is the saturation of absorption. Consider the ideal case of a two-level atom: A strong laser beam of intensity I (pump beam) excites a considerable fraction of atoms of a certain velocity group and thus depletes the number of ground state atoms in that velocity group, leaving a hole in the ground state velocity distribution of the

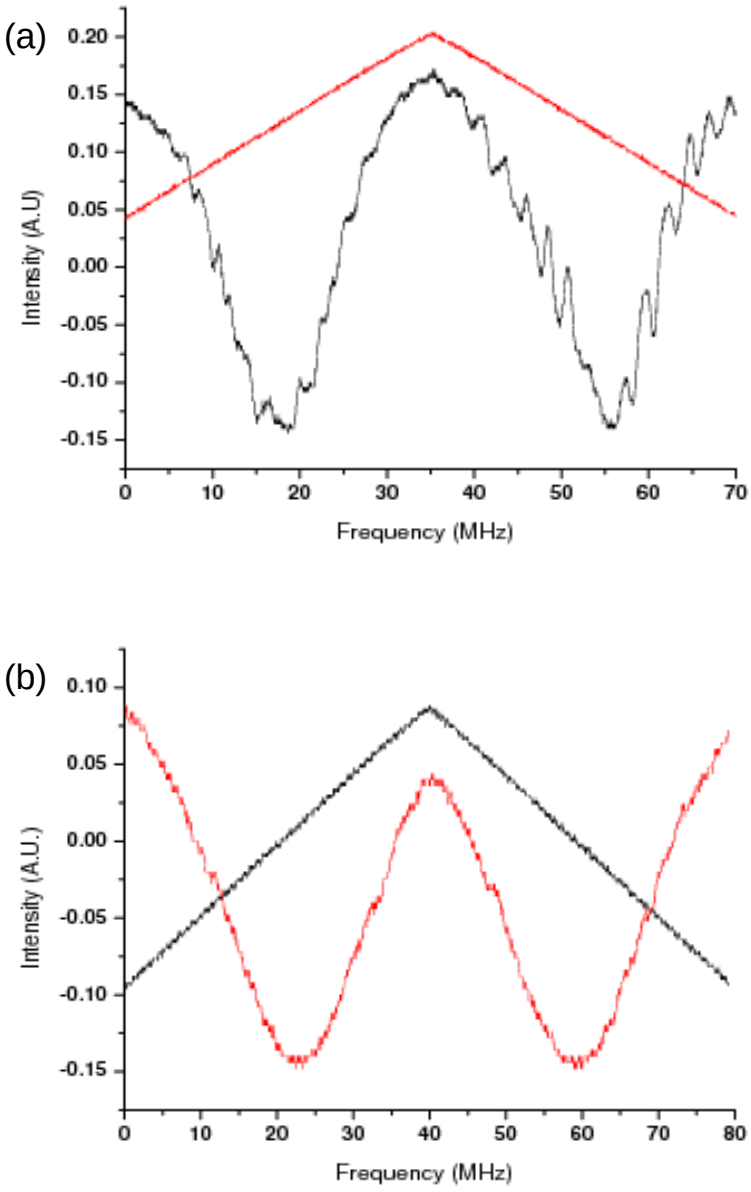

Figure 7.4 Saturation absorption spectroscopy (SAS) signals for $2^3S_1 \rightarrow 3^3P_2$ transition at $\lambda = 389$ nm: (a) Ti:Sapph laser unlocked (b) Ti:Sapph laser locked to PDH error signal

atoms ("hole burning"). The spectral width of that hole

$$\Delta\omega_{hole} = \Gamma\,(1+s)^{\frac{1}{2}} \tag{7.9}$$

is determined only by the natural linewidth Γ and the saturation parameter $s = \frac{I}{I_{Sat}}$, where $I_{Sat} = \frac{\pi hc}{3\lambda^3\tau}$ [7] is the specific saturation intensity of the atom (h: Planck's constant, c: speed of light, τ: atomic lifetime). A weak counterpropagating beam (probe beam) of the same frequency $\omega \neq \omega_0$ as the strong beam will in general be resonant with a different velocity group due to the Doppler-effect and get absorbed by a small fraction of the atoms in that velocity group. For $\omega = \omega_0$, however, both beams interact with the same velocity group, and the saturation of the transition by the pump beam results in a reduced absorption of the probe beam which is visible in the absorption spectrum at the atomic resonance frequency as a narrow peak (called "Lamb dip"). After subtracting the absorption spectra with and without the saturation effect, only the Doppler-free Lamb dip with a linewidth on the order of the natural linewidth remains.

In a saturated absorption spectrum, so-called cross-over resonances occur at frequencies halfway between two transitions that share a common energy level and have a frequency separation of less than $\Delta\omega_D$. This effect arises, when the probe beam absorption on one of the two transitions is reduced by the hole burnt into the velocity distribution by the pump beam acting on the other transition, and vice versa. Figure 7.5 (a) shows the absorption signals for the $2\ ^3\mathrm{S}_1 \rightarrow 3\ ^3\mathrm{P}_2$ transition and the cross-over resonance between $3\ ^3\mathrm{P}_2$ and $3\ ^3\mathrm{P}_1$ in He.

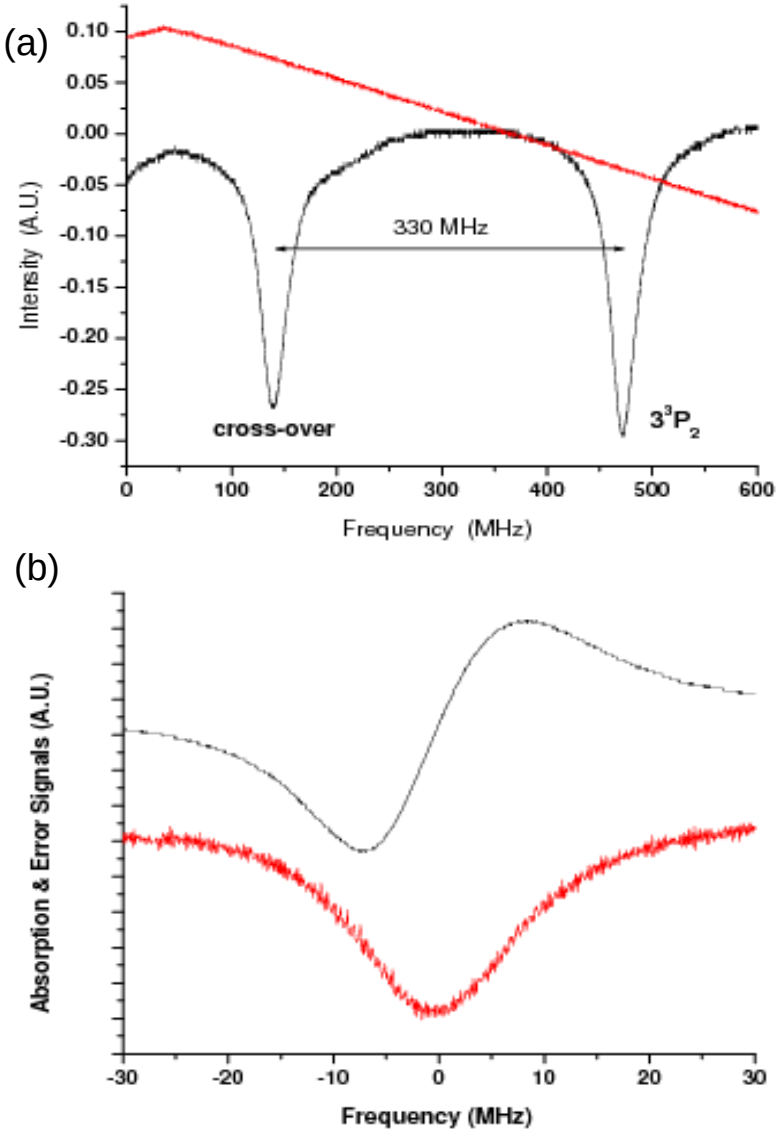

Figure 7.5 SAS signals: (a) $2^3S_1 \rightarrow 3^3P_2$ transition and crossover between 3^3P_2 and 3^3P_1 (b) $2^3S_1 \rightarrow 3^3P_2$ transition (bootom) and resulting error signal (top)

The SAS setup in this experiment can be seen in Figure 7.1 and 7.2: A helium cell is wrapped with a coil which serves as an antenna that induces a discharge in the cell when driven at an rf frequency (here: 59 MHz). Since the absorption cross-section for monochromatic light scales as $\sigma \propto \lambda_0^2$, a higher driving power is required for 389 nm light in comparison with the commonly used 1083 nm transition in helium. A combination of a $\frac{\lambda}{2}$-plate (**HWP4**) and a polarizing beam-splitter (**PBS**) is used to split off a part of the output of the frequency doubling cavity. This beam is then incident on a glass plate (**GP**), and both the weak reflected and the strong transmitted beam subsequently traverse the He cell as probe and reference beam, respectively. The pump beam ($s \sim 10$, $I_S = 3.31\ \frac{\mathrm{mW}}{\mathrm{cm}^2}$ for He [7]) is split off the main beam with a beamsplitter (**BS**) and counterpropagates the probe beam ($s \sim 1$) in the He cell. A photodiode (**PD4**) measures the intensities of the probe and the reference beam and passes the signals to the SAS feedback electronics (see Figure 7.2). By rotating **HWP4** the intensities of the pump, probe, and reference beams can be adjusted, and a variable neutral density filter (**F**) is used to balance the intensities of the probe and reference beam on the photodiode **PD4**. To prevent optical feedback from affecting the SAS setup, an optical isolator was inserted into the main beam directly after splitting off the beams for the SAS setup.

The error signal is produced from the absorption signal measured by **PD4** with a lock-in amplifier (Stanford Research Systems SR 510) operating at a reference frequency of 1 kHz which also modulates the PDH cavity via the

summing box Σ_2 when the switch **S4** is closed. A similar method of generating a DC error signal by the means of lock-in detection has already been described in the previous section (7.1.1), and [96] provides more detailed information on the specific combination of SAS and lock-in amplifier. Figure 7.5 (b) shows the absorption and the error signal which was taken at a slow scan rate ($\leq$ 1 Hz). After passing through a PID controller (Stanford Research Systems SIM 960) and a gain control stage, the error signal is fed to the PZT of the PDH cavity (**PZT2** in Figure 7.2) via Σ_2 and a high voltage amplifier.

7.1.3 Hänsch-Couillaud Locking Technique

The frequency doubling cavity is independently stabilized against perturbations employing the polarization spectroscopy locking technique developed by Hänsch and Couillaud [91]. Originally designed to lock a laser to a stable reference cavity containing an internal polarizer, it is perfectly suitable for the purpose of stabilizing a resonant enhancement cavity for second harmonic generation, because the doubling efficiency of the non-linear crystal is already strongly polarization dependent. The only other prerequisite for the HC scheme is an analyzer for elliptically polarized light that can easily be realized with a quarter waveplate, a polarizing beamsplitter, and two photodiodes.

An incident light beam whose polarization axis is rotated by an angle θ with respect to the transmission axis of the frequency doubling cavity (see [43]) can be decomposed into two orthogonal linearly polarized components. In the plane wave approximation and with the amplitude $E^{(i)}$ of the incident beam,

$E_{\parallel}^{(i)} = E^{(i)}cos\theta$ has its field vector parallel to the transmission axis of the cavity, whereas $E_{\perp}^{(i)} = E^{(i)}sin\theta$ represents the perpendicular component which serves as a reference. To first approximation, the amplitude of the reflected perpendicular component is only determined by the power reflectivity R_1 of the input coupler of the cavity [91]

$$E_{\perp}^{(r)} = E_{\perp}^{(i)}\sqrt{R_1} \tag{7.10}$$

The reflected parallel component, which is the coherent sum of the promptly reflected beam and the cavity leakage beam, experiences a frequency-dependent phase shift, and its complex amplitude becomes [91]

$$E_{\parallel}^{(r)} = E_{\parallel}^{(i)}\left[\sqrt{R_1} - \frac{T_1 R}{\sqrt{R_1}}\frac{\cos\delta - R + i\sin\delta}{(1-R)^2 + 4R\sin^2\left(\frac{\delta}{2}\right)}\right] \tag{7.11}$$

where T_1 is the transmissivity of the input coupler, $R < 1$ is the effective round trip loss of the cavity, and δ is the phase difference between the reflected perpendicular and parallel components.

On resonance, both reflected components remain in phase ($\delta = m \cdot 2\pi$, where m is an integer number), and the reflected beam is still linearly polarized, because both reflection coefficients in (7.10) and (7.11) are real. If the cavity length deviates from resonance, however, $E_{\parallel}^{(r)}$ will be ahead or delayed in phase by $|\delta|$ resulting in a reflected beam of elliptical polarization where the handedness of the ellipticity depends on whether the cavity length is too big or too small. In order to extract this phase information from the reflected beam, a polarization sensitive analyzer assembly is used: A quarter waveplate and a polarizing beamsplitter will decompose elliptically polarized light into two orthogonal linearly polarized components of different amplitude, if the waveplate

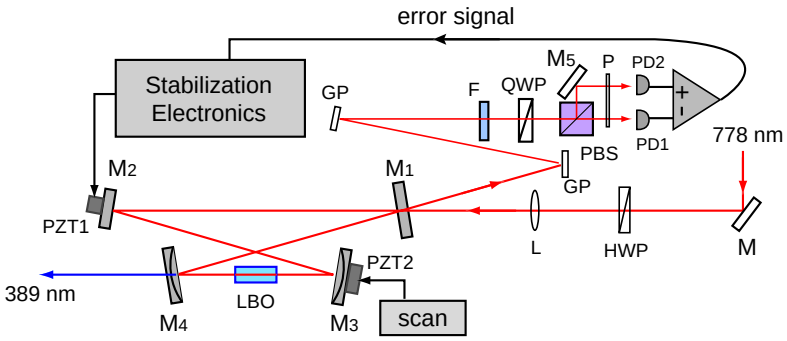

Figure 7.6 Schematic of frequency doubling cavity including optics for Hänsch-Couillaud stabilization (M: mirror, L: mode matching lens, HWP: half wave plate, QWP: quarter wave plate, GP: glass plate, PBS: polarization beam splitter, P: polarizer, F: neutral density filter, PD: photodiode detector)[43]

is oriented at 45° relative to the polarization axis of the beamsplitter. The intensities I_i $(i = 1, 2)$ of the two outputs of the beamsplitter can be measured with a photodiode, and since they will not be equal but on resonance when the reflected beam is linearly polarized, the subtraction of the two outputs [91]

$$I_1 - I_2 = 2I \cos\theta \sin\theta \frac{T_1 R \sin\delta}{(1-R)^2 + 4R\sin^2\left(\frac{\delta}{2}\right)} \tag{7.12}$$

can be used as an error signal ($I^{(i)}$: intensity of incident light). Although (7.12) is maximal for $\theta = 45°$, operation at smaller angles $\theta \sim 0$ will both ensure a higher transmission of the frequency doubling cavity and provide a better signal to noise ratio, if laser fluctuations are the main source of noise [91].

Figure 7.6 shows the HC setup in this experiment. The polarization of the main beam can be adjusted to match the transmission axis of the frequency doubling cavity with a half waveplate **HWP**. The reflected light from the

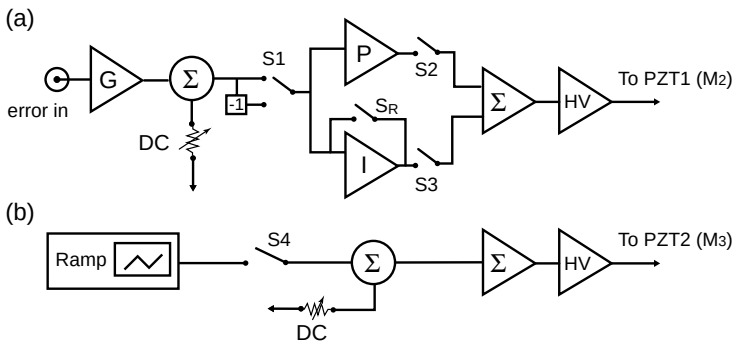

Figure 7.7 Control Electronics for the doubling cavity (G: gain control, S: switch, Σ: summing junction, P: proportional control, I: integral control, HV: high voltage amplifier)[43]

cavity is deflected and attenuated with two glass plates **GP** and a neutral density filter **F**, before it enters the detection assembly consisting of a quarter waveplate **QWP**, a polarizing beamsplitter **PBS**, a polarizer **P**, and two photodiodes **PD1** and **PD2**. The error signal created from the subtraction of the signals from **PD1** and **PD2** is processed by stabilization electronics shown in Figure 7.7. After passing through an integrator **I**, which compensates slow deviations, and a proportional controller **P**, that copes with fast fluctuations, separately, the signals are recombined in a summing junction **Σ** and fed to **PZT1** of the frequency doubling cavity. **PZT2** is used to scan the cavity when the feedback loop is not active. Figure 7.8 shows experimental results for the HC error signal and the transmission signal of the frequency doubling cavity. Since the HC error signal has a large capture range, automatic re-locking is quite common.

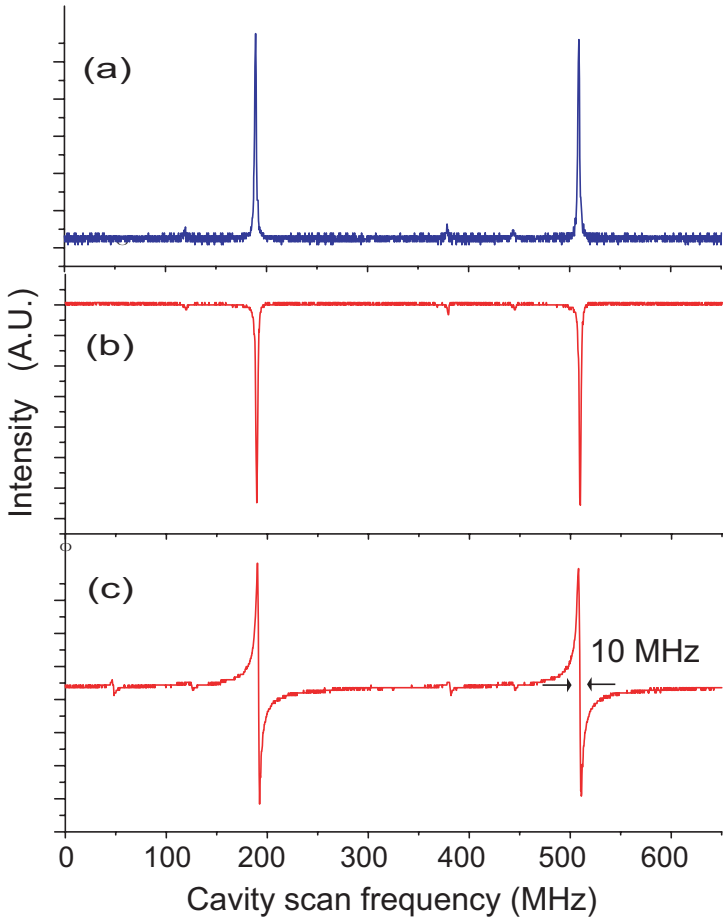

Figure 7.8 Experimental results for the frequency doubling cavity: (a) transmitted blue light (b) reflected red light (c) Hänsch-Couillaud error signal

7.2 Red Laser

The schematic of the red laser system is shown in Figure 7.9. A Coherent Innova 310 Argon-Ion laser with a maximum output power of 10 W in the wavelength range of 457.9 – 514.5 nm pumps a Tekhnoscan TIS-SF07e Ti:Sapph laser which has a single mode output power of ~ 1 W at $\lambda = 780-796$ nm. The low output power compared to the Ti:Sapph laser used to generate the blue

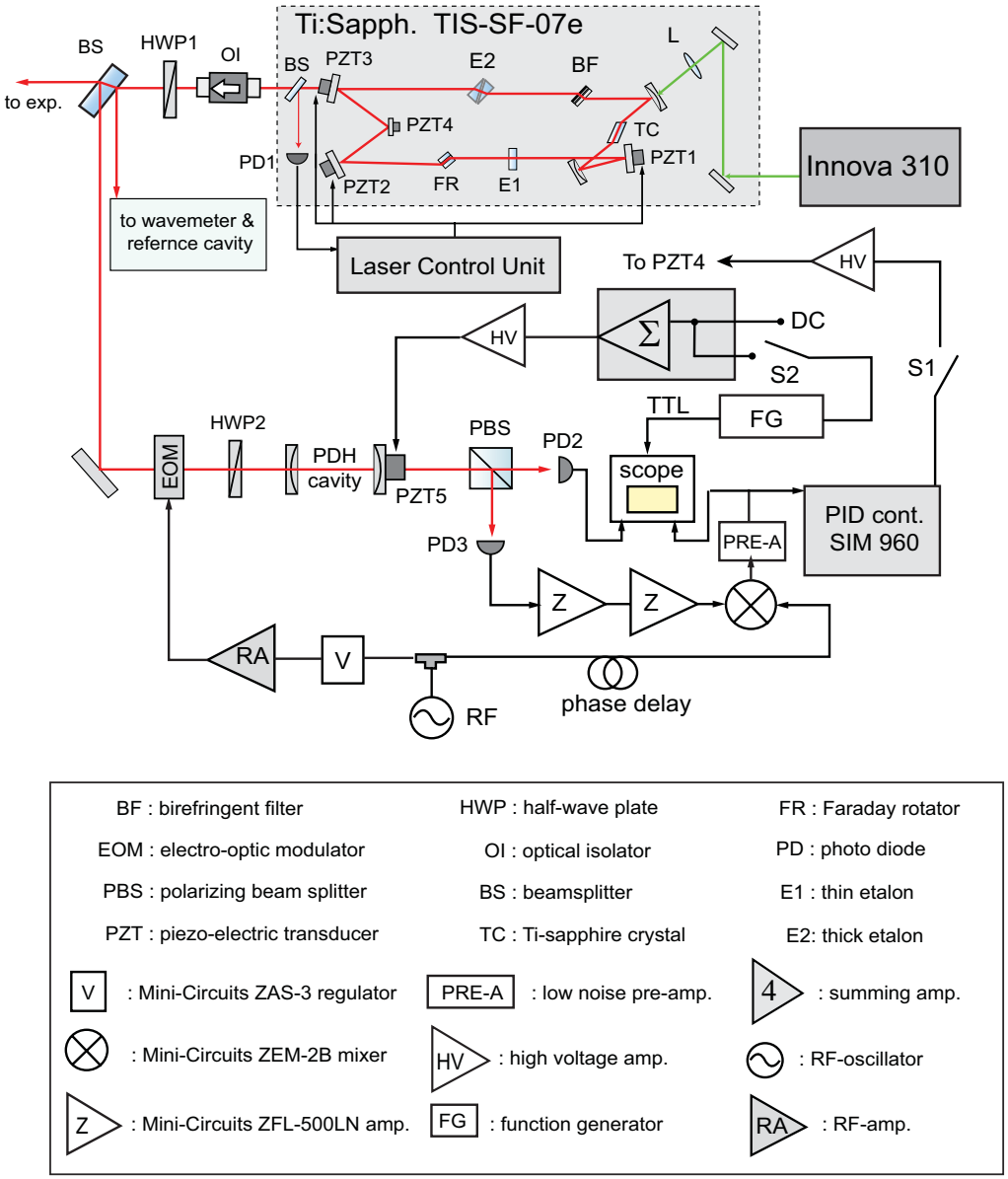

Figure 7.9 Schematic of red laser system [43]

light might result from a combination of factors: Since the Argon-Ion laser has been used for several years without cleaning or replacing the discharge tube, the pumping power is lower than 10 W. The pumping efficiency might also be lower, because the spectral distribution and mode quality of the Innova 310 are worse than those of the Verdi V10. Furthermore, the different ring geometry of the Tekhnoscan Ti:Sapph laser cavity might result in lower output power, since it contains more mirrors and mode selective elements, and the Ti:Sapph crystal itself might be of lower quality than the one in the blue laser. The TIS-SF07e comes with an electronic control unit that allows electronic adjustment of the mode selective elements (etalons **E1** and **E2**, birefringent filter **BF**, and Faraday rotator **FR**) inside the laser cavity. In addition, an intensity locking system is included: A photodiode (**PD1**) monitors intensity fluctuations in the output beam, and the error signal generated from this photodiode signal is fed to the PZTs **PZT1**, **PZT2**, and **PZT3** to stabilize the laser cavity at the length of maximum output power. Although the frequency stability of the red laser is not as critical as that of the blue laser because the Stark energy levels of the He atoms are scanned through their resonances during the experiment, another PZT (**PZT4**) was added to the laser cavity so that the PDH frequency locking technique (see 7.1.1) can be applied. Therefore, the red laser can be stabilized either by intensity or by frequency locking.

Chapter 8

Experimental Results

8.1 Stark Map

The Stark map for the $n = 26$ state ($m = 0$) of triplet helium was determined experimentally and is shown in Figure 8.1. During the experiment, the blue laser was locked to the $2\ ^3S_1 \rightarrow 3\ ^3P_2$ transition, while the red laser was locked at a selected wavelength in the range between 796.42 nm and 796.81 nm which corresponds to the transition to the $n = 26$ Rydberg state. In order to analyze the field-dependence of that state, the lower field plate was scanned with a function generator (Stanford Research Systems SRS DS335) at a frequency of 100 Hz and an amplitude of $U_{PP} = 10$ V, whereas the voltage applied to the upper field plate was carefully altered by hand. Thus, the different Stark energy levels were shifted into resonance with the red laser by changing the strength of the applied electric field. This method was preferred to setting the field strength to a certain value and scanning the frequency of the red laser, because the range in which the laser can be scanned without mode-hops is lim-

ited. After separately recording the ion signals for the transitions to each of the experimentally available Stark energy levels with a Tektronix TDK 210 oscilloscope, the Stark map shown in Figure 8.1 was created by joining the data in one plot. The laser was subsequently locked to fifteen different wavelengths during the experiment, and the field strengths at which resonance occured are indicated as dots. In Figure 8.1, the strongly depressed 26S state in the lower left hand corner and the manifold region denoted by **A** are clearly resolved, whereas it is rather difficult to recognize the avoided level crossings (region **B**).

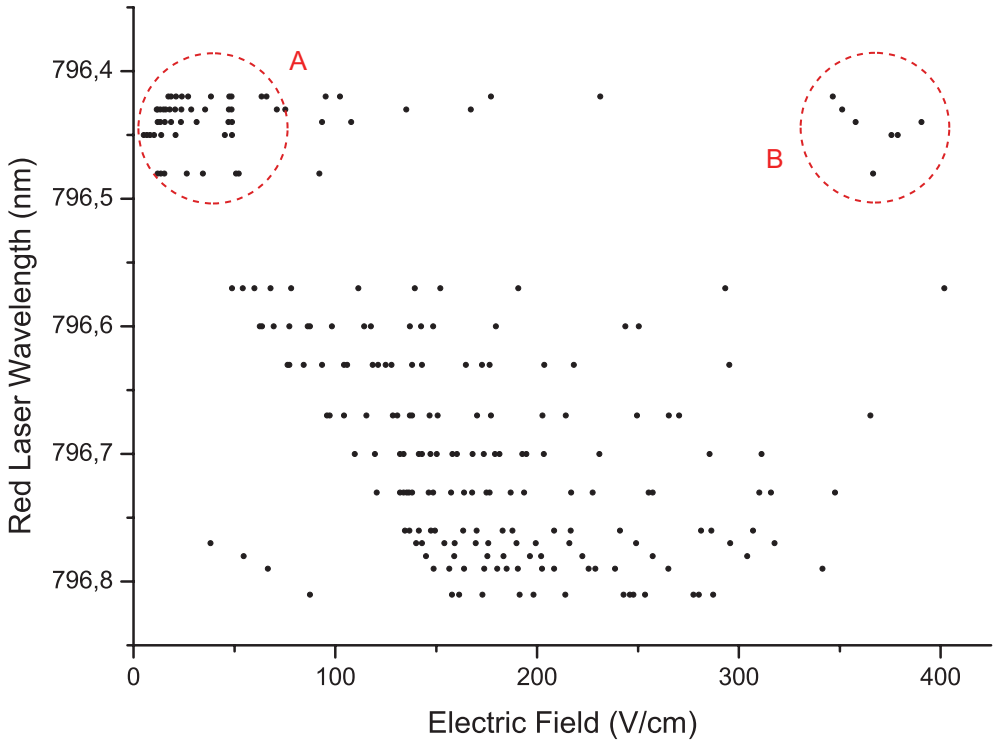

Figure 8.1 Experimentally obtained Stark map for n=26 (compare A and B in Figure 2.3). The $26\,^3S_1$ level is clearly identifiable in the lower left-hand corner.

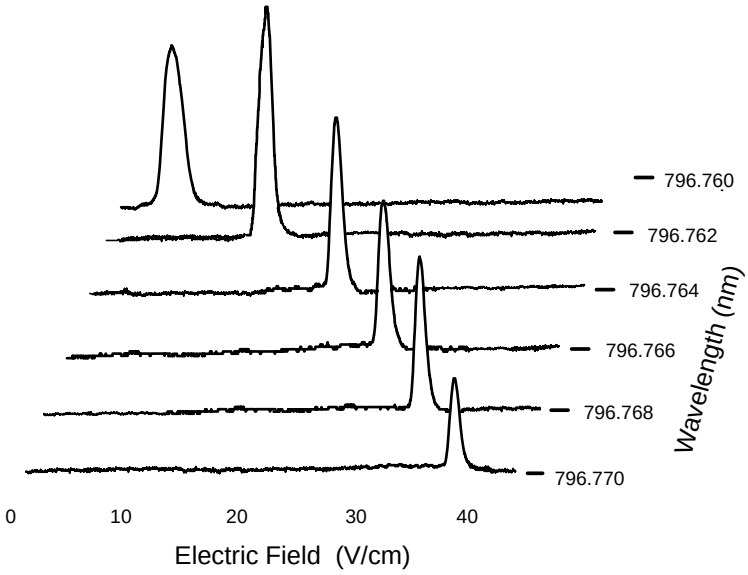

Figure 8.2 Experimentally obtained transition strengths for the $26\,^3S_1$ state as a function of the applied external electric field. See text for a discussion of the reversed trend compared to Figure 2.4.

Figure 8.2 is a large scale plot of the relative intensities of the transitions to the $n = 26$S state that were obtained in the Stark map experiment. In contrast to the theoretical calculations depicted in Figure 2.4, the experimentally observed transition strength is maximal at zero-field and decreases with increasing electric field. We propose that this contradiction might arise from the fact that the absolute number of resonant atoms is lower at higher fields because of inhomogeneities in the electric field produced by the field plates. Furthermore, the range of the electric field, in which the atoms are resonant, is bigger at lower field strengths and decreases as the field increases due to the

quadratic dependence of the 26S level on the electric field. As a result, the ion signals for low fields show a larger width than their counterparts for higher fields [34].

8.2 STIRAP

All our STIRAP experiments were done in the three-level scheme shown in Figure 5.1. The experimental configuration in the interaction chamber has been described in 6.3 and is illustrated in Figure 6.4. During the experiment, a Tektronix TDK210 oscilloscope was used to monitor and record the Rydberg signal which was obtained from the ion detector (see subsection 6.4.1) through scanning the field plates through the atomic resonances.

Aligned co-propagating, the red and the blue laser beams were focused onto the atomic beam with two separate cylindrical lense ($f = 400$ mm and $f = 800$ mm for red and blue, respectively) such that their long axes were oriented perpendicular to the atomic beam and their horizontal Gaussian waists became 400 μm and 600 μm, respectively. Similarly, the lengths of the vertical waists were measured to be 1.5 mm for the pump and 2.0 mm for the Stokes laser, and their Rabi frequencies were approximately matched in a range between $35 \sim 40$ MHz. A dichroic mirror mounted onto a translation stage allowed us to spatially shift the axes of the pump and Stokes lasers relative to each other and thus change the order in which the atoms encounter the two laser beams.

Figure 8.3 shows our experimental results for the transfer efficiency as a function of the separation of the two laser beams. We obtained the maximum

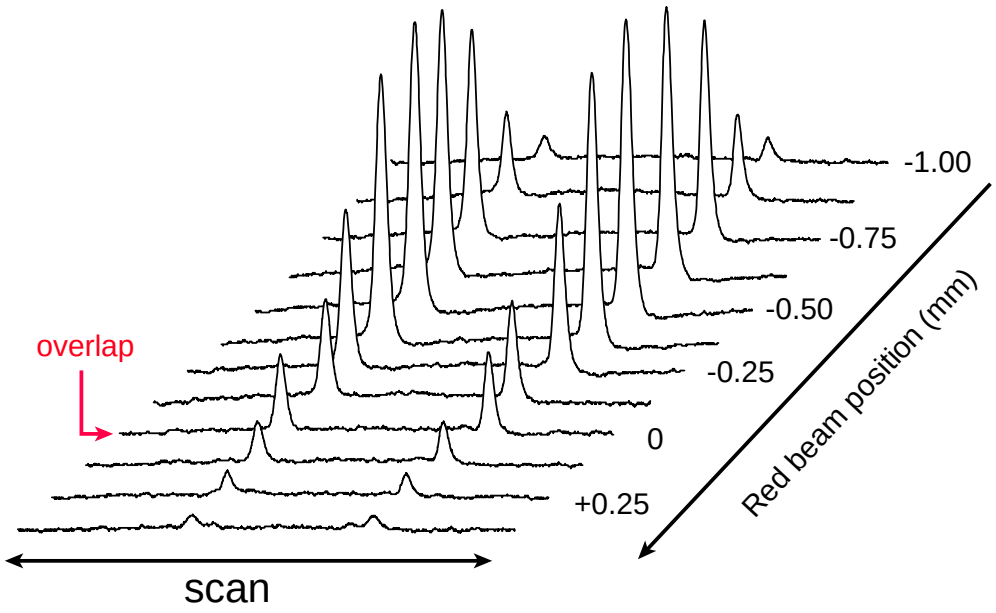

Figure 8.3 Ion signal as a function of the red (Stokes) beam position. Negative (positive) positions correspond to the counter-intuitive (intuitive) pulse order. The origin of the scale corresponds to overlapping pump (blue) and Stokes (red) beams.

transfer efficiency in STIRAP configuration, when the atoms saw the red beam 0.4 mm ahead of the blue beam which corresponds to an interaction time of $\sim 2.5\ \mu$s at an atomic velocity of 1500 $\frac{\mathrm{m}}{\mathrm{s}}$. In that case, the pulse area becomes $\Omega_{\mathrm{eff}}\Delta\tau > 13 \pm 2$ so that the adiabatic condition (3.41) just about holds. It can clearly been seen from Figure 8.3 that the excitation process is much more efficient for the counter-intuitive pulse order of STIRAP than for the intuitive order or overlapping laser beams. The relative efficiency of STIRAP compared to the two-photon transition can be determined from Figure 8.3 to be ~ 3.75.

A measurement of the absolute transfer efficiency of STIRAP is under way.

The proposed experiment will use blue light that has been split off the main beam initially to measure the excitation efficiency with blue detuned optical molasses [7] directly downstream of the STIRAP interaction region. The optical molasses will spread the spatial distribution of He^* atoms that have not been excited by the STIRAP beams but leave Rydberg atoms unaffected. Thus, a comparison of the spatial distribution acquired with STIRAP to the distribution obtained from a mere excitation with the blue laser will yield information about the absolute efficiency of STIRAP. Promising progess towards a first quantitative measurement has been made.

8.3 Autler-Townes Effect

The experiments to observe the Autler-Townes effect were carried out essentially with the same setup and equipment as the STIRAP experiments (see Section 6.3). The main difference was that the axes of the laser beams were fixed in an overlapping configuration with a beam waist of 1 mm and 0.4 mm and a beam height of 2 mm and 1.5 mm for the blue and the red beam, respectively, and that the power of the red beam was drastically reduced to about 50 mW ($\Omega_{pr} \sim 3$ MHz) compared to the STIRAP experiment. During the experiment, the blue laser (40 mW, $\Omega_{st} \sim 35$ MHz) was locked to the $2\ ^3S_1 \rightarrow 3\ ^3P_2$ resonance, whereas the red laser was locked to the $3\ ^3P_2 \rightarrow 26\ ^3S_1$ in He. Tilting the blue laser beam with respect to the atomic beam allowed us to detune the laser while it was locked on resonance which is generally favorable to the stability of the laser frequency. The frequency sweep of the probe was replaced

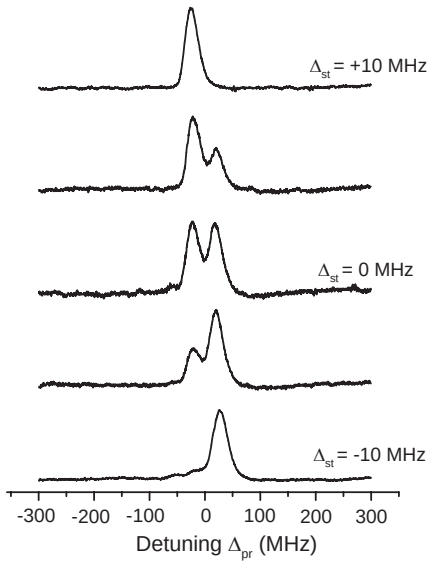

Figure 8.4 Experimentally observed dependence of the Autler-Townes splitting on the single-photon detuning Δ_{st}

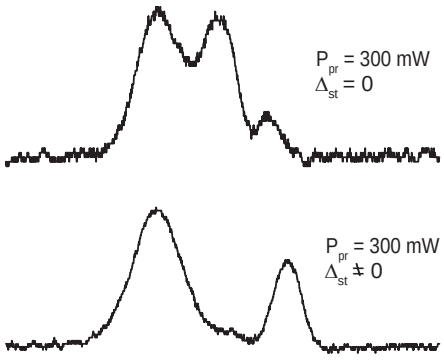

Figure 8.5 Autler-Townes effect for strong probe beam at different single-photon detunings Δ_{st}: A satellite peak appears.

by scanning the field plates and shifting the Stark energy levels through the resonances with the transitions.

Figure 8.4 shows the observed ion signals for different detunings of the blue laser. The Autler-Townes splitting caused by the blue laser is clearly visible. Since the dressed states consist of a mixture of the 2 $^3S_1$ and the 3 $^3P_2$ states, of which only the 3 $^3P_2$ state has a non-vanishing transition matrix element with the 26 $^3S_1$ state due to the optical selection rules for pure electric dipole coupling, the intensities of the two peaks strongly depend on the detuning which controls the composition of the dressed states via the mixing angle θ.

When the power of the red laser was increased to about 300 mW so that the Rabi frequencies of the two lasers became comparable, the red laser was strong enough to dress the transistion to the Rydberg state. In this case, the set of dressed states becomes more complicated. Figure 8.5 shows qualitatively that a third satellite peak could be observed in the ion signal for zero detuning of the blue laser ($\Delta_{st} = 0$). Off-resonance, a third peak is faintly visible between the two pronounced components.

8.4 Focusing

Since the created Rydberg helium atoms only have a specific finite lifetime, the electrostatic lens has to be positioned carefully to obtain the most effective focusing. In our experiment, the He* atoms are excited to the 26S state which has a lifetime of $\tau \sim 40$ μs. Thus, the lens should definitely be located sufficiently closer than 6 cm to the interaction region at an average atomic

longitudinal velocity of 1500 $\frac{\mathrm{m}}{\mathrm{s}}$. The distance between the field plates and the lens was $\sim$ 2 cm in our case. As shown in Figure 4.3(a), the six electrodes of the field lens are alternately supplied with two voltages U_+ and U_- from a Stanford Research Systems PS325 high voltage power supply and a Hewlett Packard 6516 DC power supply. Once the Rydberg signal had been observed with the ion detector, the two lens voltages were adjusted in order to optimize the brightness of the image of the focused beam on the phosphor screen detector. Figure 8.6 shows a result of our focusing experiments: Figure 8.6(a) is just an image from the PSD when the red laser beam was blocked, and thus no Rydberg atoms were created. In Figure 8.6(b), the beam of Rydberg atoms created by the 2-photon transition was focused at lens voltages of $U_+ = 211$ V and $U_- = 0$ V. The evaluation of the horizontal and vertical intensity profiles of Figure 8.6(c) and Figure 8.6(d) gives full widths at half maximum of 3 mm and 0.6 mm, respectively. Figure 8.6(e) depicts that the image of the focused beam is not centered within the atomic beam because the lens is not centered with respect to the slightly tilted atomic beam. The asymmetric shape of the focused beam might result from a combination of factors: The spot size itself depends on the velocity distribution of the atoms. Furthermore, the profile of the atomic beam is determined by the slit dimensions (0.5 $\times$ 2 mm) and also by the dimensions of the field plates. Therefore, it might be favorable for the future to transversely cool the atomic beam to minimize chromatic abberations. A surface plot of the focused atomic beam is shown in Figure 8.7.

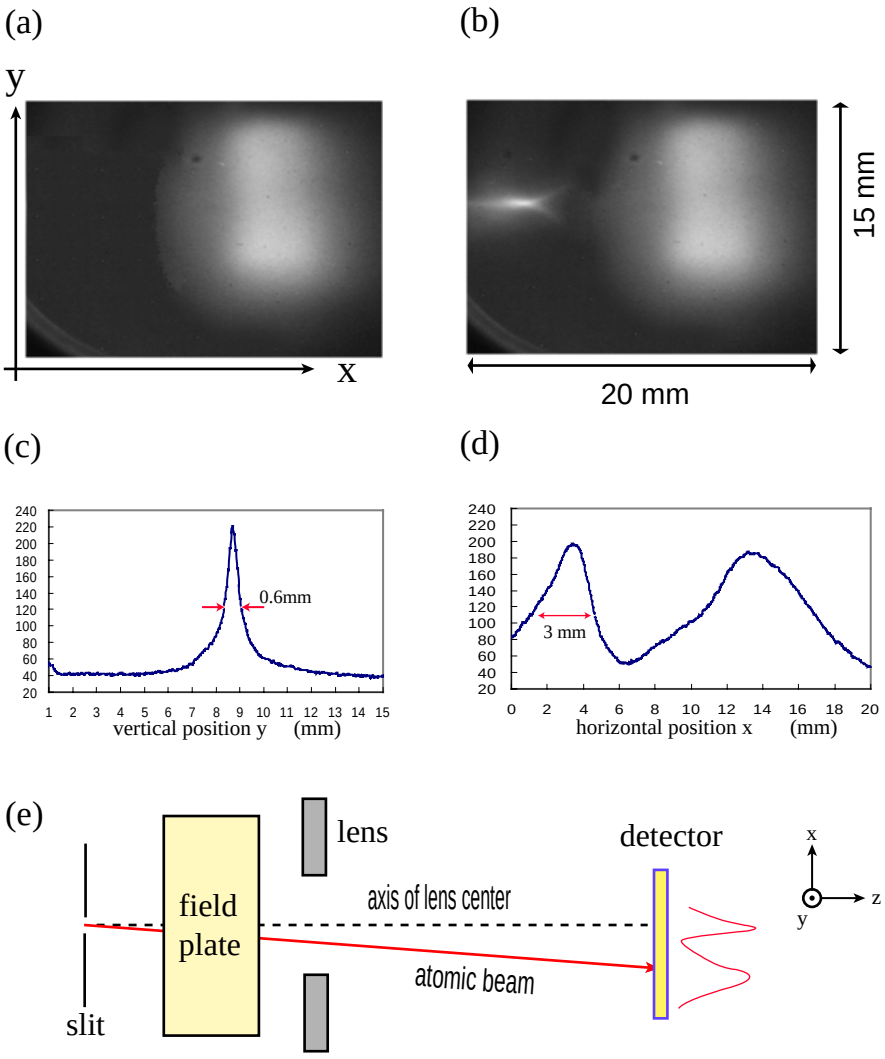

Figure 8.6 Experimental results on focusing the He* atomic beam: (a) PSD signal without laser excitation (b) PSD signal with laser excitation (c) vertical profile of the focused beam (see (b)) (d) horizontal profile of the focused beam (see (b)) (e) atomic beam geometry

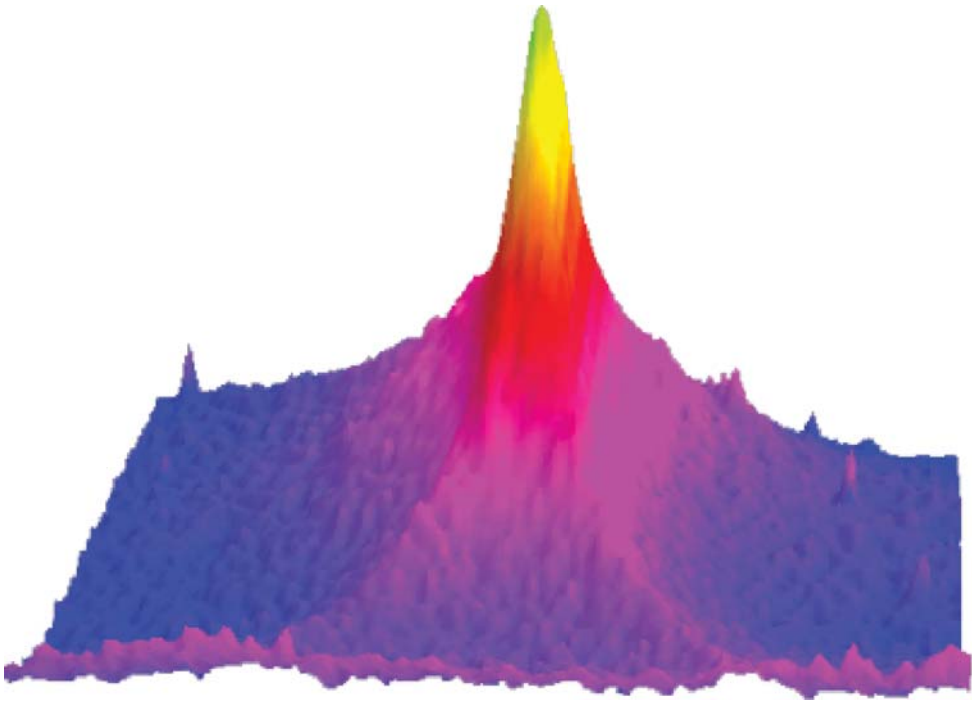

Figure 8.7 Surface plot of focused atomic beam

Chapter 9

Conclusions

Experiments with Rydberg atoms are an exciting subfield of atom optics because of the advantages associated with their unique properties. We have done Stark spectroscopy on the $n = 26$ level of helium and experimentally measured a Stark map and the corresponding oscillator strengths for the transitions from the $3\,^3P_2$ level. Our results for the transition strength of the $3\,^3P_2$ state seem to disagree with the theoretical predictions, but we have proposed a possible explanation for this effect. Since the wavelength of the red laser can easily be tuned to a transition to a different Rydberg state, experimental Stark mapping of different Rydberg He energy levels is at hand for further investigations.

The counter-intuitive STIRAP technique was used to coherently excite He^* atoms to selected Rydberg states. In the course of the experiment, a relative efficiency of ~ 3.75 of STIRAP compared to the intuitive two-photon transition has been measured. Experiments to investigate the absolute excitation efficiency employing a scheme based on blue detuned optical molasses are under way. First qualitative measurements show promising results.

In order to optimize the parameters for a successful application of the STIRAP scheme, the Autler-Townes effect was observed and used to determine the Rabi frequency of the excitation lasers experimentally. Effects in qualitative agreement with the dressed atom picture occured when the intensity of the probe beam was increased.

An electrostatic hexapole lens has been successfully used to manipulate the trajectories of Rydberg helium atoms created by means of the STIRAP excitation technique. Although a focusing effect could be clearly demonstrated, the experiments still provide opportunities for major improvement. The transverse motion of the thermal beam produced by our source could be reduced with a stage of two-dimensional red detuned optical molasses prior to passing through the lens. Due to the higher flux of the precollimated beam, the focusing might be more efficient in that case. Furthermore, if the electrodes of the hexapole lens were adressed separately by computer controlled voltage supplies, the position of the focal point of the lens could be moved easily.

This would be especially suitable for one of the possible applications, neutral atom nanolithography, in which the high internal energy of He^* atoms is exploited to create nanoscale structures either through direct deposition of He^* atoms or by exposing a suitable resist material with the He^* atoms.

In conclusion, this thesis shows experimental progress towards precise control over the spatial and velocity distibutions of Rydberg atoms that might eventually lead to electrostatic trapping of Rydberg atoms in a selected Stark state.

Appendix A

Atomic Units

Quantity	Definition in atomic units	Value
Charge (e)	Charge of the electron	1.60218×10^{-19} C
Mass (m)	Mass of the electron	9.108×10^{-31} kg
Length (a_0)	Radius of Bohr orbit ($\hbar^2/me^2$)	5.2917×10^{-11} m
Velocity (v_0)	Electron velocity in Bohr orbit ($e^2/\hbar = \alpha c$)	2.1877×10^6 m s^{-1}
Energy (e^2/a_0)	Twice the ionization energy of H	27.2112 eV
Frequency	$v_0/a_0 = me^4/\hbar^3 = 4\pi R_y$	4.1341×10^{-16} s^{-1}

Appendix B

Spectroscopic Data for the 389 nm transition

Quantity	Value
Excited state lifetime (τ)	105.5 ns
Transition Linewidth ($\frac{\Gamma}{2\pi}$)	1.51 MHz
Saturation Intensity ($I_s = \frac{\pi hc}{3\lambda^3\tau}$)	3.35 $\frac{\mathrm{mW}}{\mathrm{cm}^2}$
Capture velocity ($v_c = \frac{\Gamma}{k}$)	58.7 $\frac{\mathrm{cm}}{\mathrm{s}}$
Recoil velocity ($v_r = \frac{\hbar k}{M}$)	25.6 $\frac{\mathrm{cm}}{\mathrm{s}}$
Doppler limit ($v_D = \sqrt{\frac{k_B T_D}{M}}$)	27.4 $\frac{\mathrm{cm}}{\mathrm{s}}$
Doppler temperature ($T_D = \frac{\hbar\Gamma}{2k_B}$)	36.2 μK

Table B.1 Spectroscopic data for the $2\,^3\mathrm{S}_1 \rightarrow 3\,^3\mathrm{P}_2$ transition [44]

(mass $M = 6.646 \times 10^{-27}\,\mathrm{kg}$, $k = 2\pi/\lambda$ with $\lambda = 388.98$ nm)

Appendix C

Operational Manual

C.1 Vacuum System

The vacuum system was designed in a way that allows us to bring the different chambers to air without having to turn the diffusion pumps off. The gate valves in our system, however, might not close tight, because the O-rings in them, which cannot easily be replaced, are old and probably worn out. Thus, in order to prevent the system from any kind of serious trouble due to imperfections of the gate valves, the diffusion pumps are usually turned off whenever the system is brought to air. It takes the diffusion pumps around three hours to cool down so that any work on the vacuum system should be carefully planned. The following sections describe the experimental procedures to vent and evacuate the different vacuum chambers chambers (see Figure C.1).

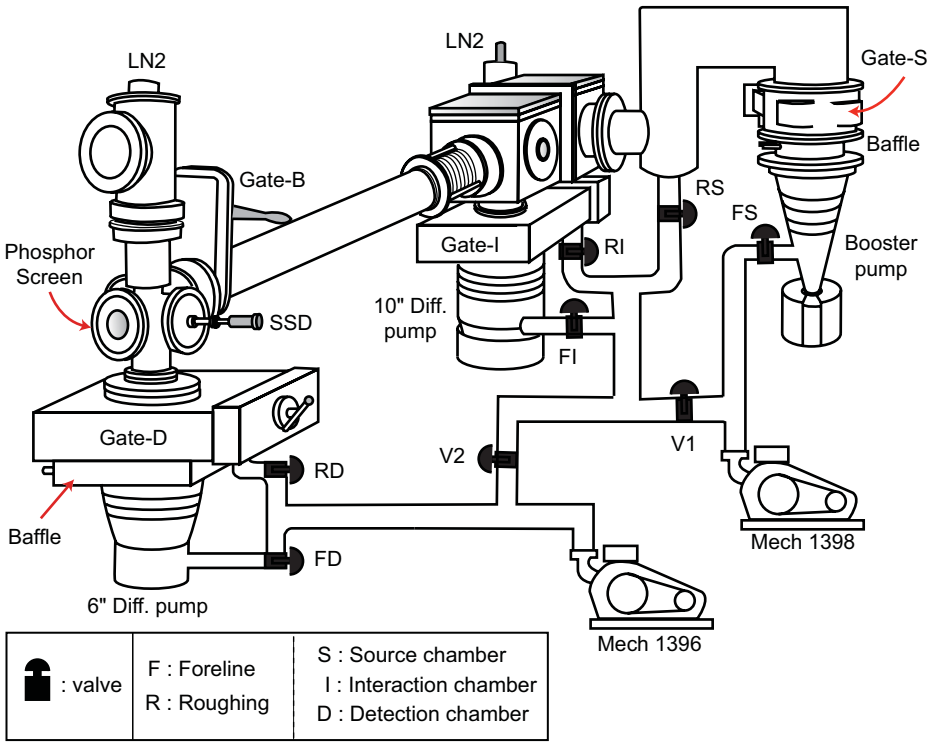

Figure C.1 3D schematic of vacuum system [43]

C.1.1 Source and Interaction Chamber

Venting Procedure

1. Close gate valve **Gate-B** in order to isolate the detection chamber!

2. Turn off the booster pump and the 10" diffusion pump and let them cool down for about three hours!

3. Once the pumps have cooled down, isolate the chambers from the mechanical pumps and from the vacuum loop for the detection chamber by closing valves **FS**, **V1**, and **V2**!

4. Open the vent valve (not shown in Figure C.1) and vent the system!

Evacuation Procedure

1. Close the vent valve!

2. Open **FS** and **V1** simultaneously! This should be done carefully and slowly, because sudden pressure changes in the source chamber result in a big pressure difference between the inside and the outside of the glass tube and might damage it.

3. Once the pressure in the foreline falls below 100 mTorr, it is safe to turn on the diffusion pumps (booster pump and 10")! However, we usually wait until the foreline pressure is lower than 50 mTorr.

4. When the pressure in the interaction chamber falls below 10^{-5} Torr, open **Gate-B** so that the chambers are also pumped down through the detection vacuum loop! Naturally, this does not apply as long as the detection chamber is kept at an extremely different pressure.

C.1.2 Detection Chamber

Venting Procedure

1. Isolate the detection area by closing the gate valve **Gate-B** and make sure that the roughing valve **RD** is closed!

2. Open **V1** and close **V2**!

3. Turn the 6” diffusion pump off and let it cool down for about three hours!

4. Close **FD**!

5. Vent the system by opening the vent valve for the detection chamber (not shown in Figure C.1)!

Evacuation Procedure

1. Close the vent valve!

2. Open valve **FD** (**RD** is always closed) so that the detection chamber is pumped down by the mechanical backing pump! If the pressure does not fall, close **FD** and vent again! Turn the mechanical pump (Welch Duo-seal 1396) off, take the plastic tube at the pump off to reset the pressure at the pump to atmosphere, reconnect the tube, turn the pump on and repeat the procedure from 1. This is necessary, because the mechanical pump will not work properly if the pressure at the outlet of the diffusion pump is too low, that is, out of the pressure range the mechanical pump operates in.

3. Once the pressure in the foreline drops below 100 mTorr, turn the diffusion pump on!

C.2 Source

This section describes how to run the He discharge source and provides some ideas for troubleshooting if the source does not work.

C.2.1 Source Operation

1. At the helium tank, first open the valve $\mathbf{V_2}$ and then $\mathbf{V_1}$! Following this order is important because it avoids a contamination of the high purity helium in the tank by residual gas in the tube between the tank and the source chamber.

2. Using the microvalve $\mathbf{V_P}$ adjust the He flow so that the inlet pressure rises to about $50 - 70$ Torr. This pressure should not exceed 200 Torr, because the glass tube might be damaged in higher pressures. Therefore, it is recommended to close the valves $\mathbf{V_3}$ and $\mathbf{V_4}$ until the inlet pressure is in the safe region below 200 Torr. After adjusting the pressure to the desired value with the microvalve, $\mathbf{V_4}$ can be opened. $\mathbf{V_3}$ should be kept closed all the time except for pumping out gas from the plastic tubing between helium tank and source. Opening $\mathbf{V_3}$ for that purpose will speed up the process because the gas will get pumped out through the source chamber instead of through the glass tube.

3. Wait for ~ 10 minutes until the He flow has reached its equilibrium value!

4. Apply -3 kV to the tungsten needle by turning on the high voltage power supply sitting on the ground! After a delay of few seconds, the discharge usually starts.

5. The source is running in a current limiting mode realized by a 100 kΩ power resistor that is in series with the source circuit. Adjust the current to optimize the signal seen by the ion detector or the phosphor screen

detector! The best conditions are usually in the range of $8 - 10$ mA. At a current of more than 20 mA the power resistor might blow.

C.2.2 Troubleshooting

Sometimes the discharge will not start at the nozzle but inside the glass tube. Since this is mostly the case, if the pressure in the glass tube is too low, increasing the inlet pressure to $\sim$ 100 Torr by adjusting $\mathbf{V_P}$ might solve the problem. Once the discharge runs correctly, the pressure should be reduced again to avoid a higher quenching rate of metastables.

If the discharge does not start at all, there are two things to check: The power resistor could be blown or the nozzle of the glass tube could be blocked. In the latter case, the inlet pressure should be higher than usual whereas the backup pressure at the booster pump should have decreased because there is no gas flow through the nozzle. Unlike replacing the power resistor, cleaning (or even replacing) the glass tube is a considerable effort because the system has to be brought to air.

C.2.3 Building Glass Tubes

Both ends of the glass tube (diameter 25 mm, length $\sim$ 135 mm) are sealed with caps made of boron nitride (BN) that have to be custom machined out of a 1" diameter rod (see Figure C.2) and then glued to the tube with Aremco Inc. *Ceramabond 503*. The hole of 150 μm diameter and approximately 1 mm length has to be drilled into the front cap using a micro-drill. A thin glass

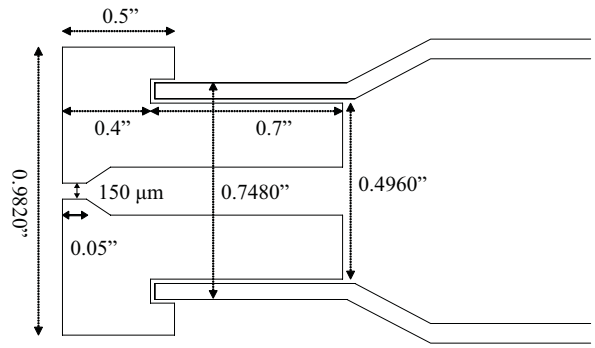

Figure C.2 Schematic of glass tube

tube (diameter 5 mm) is fed through the back cap (not shown in Figure 6.2) in order to guide the tungsten needle to the nozzle in the front cap. A spacer (also made of BN) is inserted in the big glass tube about halfway between front and back cap to support the thin glass tube.

C.3 Laser Systems

This section is intended to provide all necessary information to run the laser systems and optimize their performance. Especially, the somewhat complex locking procedure of the blue laser is elucidated.

C.3.1 Alignment and Locking of Frequency Doubling Cavity

This section summarizes the important aspects of the general alignment procedure of the frequency doubling cavity as described in [97] and provides information the locking and on further alignment optimization.

Alignment from Scratch

1. To align the frequency doubling cavity from scratch, first turn the high voltage power supplies for the two cavity PZTs off!

2. Make sure that the infrared ($\lambda \sim 778$ nm) main beam is travelling parallel to the optical table!

3. Adjusting mirror **M** in Figure 7.6, make the main beam pass through the center of the input coupler $\mathbf{M_1}$ and hit the center of the small mirror $\mathbf{M_2}$!

4. Use the controls of $\mathbf{M_2}$ to guide the beam to the center of the spherical mirror $\mathbf{M_3}$!

5. Adjust $\mathbf{M_3}$ to have the beam pass through the LBO crystal such that it hits the center of the dichroic mirror $\mathbf{M_4}$ (output coupler) which is transmissive for the second harmonic light, but reflective for light at the fundamental frequency! Behind the crystal, the fundamental beam and the second harmonic beam will be visible separately due to the walk-off (see for example [92]). All further instructions refer to the fundamental beam.

6. Align $\mathbf{M_4}$ to make the beam hit $\mathbf{M_1}$ exactly at the same spot as the incoming beam!

7. Close the loop by adjusting $\mathbf{M_1}$ so that the beam that has already travelled one round trip inside the cavity overlaps with the incoming beam!

A good way to do so is to make the two beams hit the same spot on $\mathbf{M_2}$.

8. Optimize the alignment tweaking mirrors $\mathbf{M_1} - \mathbf{M_4}$ and the crystal mount until infrared flashes appear inside the cavity! If the crystal position is good enough, it will be possible to see blue flashes on a piece of paper behind the output coupler. Fine adjustment of the crystal mount is necessary to maximize the intensity of the blue flashes.

9. Turn on the high voltage supplies for the cavity PZTs and start scanning the cavity!

10. Split a part of the cavity output beam off with a beamsplitter and guide it to a photodiode to observe the transmission signal of the frequency doubling cavity! Trigger the oscilloscope with the TTL signal from the scan!

11. Maximize the transmission signal by doing fine alignment on mirrors $\mathbf{M_1} - \mathbf{M_4}$ and the crystal mount. At the same time, watch the intensity of the main blue beam with a piece of paper and try to find a compromise between maximum transmission and maximum intensity of the blue light. The best alignment is the one where the transmission signal just shows periodic high peaks and no sidepeaks.

12. Check, if the current alignment is really optimum by carefully touching and, if necessary, adjusting **M** and by rotating the waveplate **HWP** in order to change the input ploarization!

Locking

1. Once the alignment is optimized, balance the HC error signal by rotating the waveplate **QWP** and the polarizer **P**!

2. Adjust the DC offset and turn the scan off (Controller # 1)!

3. Switch the integrator on (switch **S2**) and flip $\mathbf{S_R}$ to open the bypass of the integrator!

4. Balance the locking signal around zero by changing DC offset and gain!

5. Use the reset switch $\mathbf{S_R}$ to relock the cavity to resonance if the cavity jumps out of the lock! $\mathbf{S_R}$ resets the PZT voltage for the error compensation, if it reaches its limit value.

Alignment Optimization

It turned out that the performance of the frequency doubling cavity can be improved further, if the mirrors $\mathbf{M_2}$ and $\mathbf{M_3}$ and the crystal mount are adjusted very carefully and slowly while the feedback system is operating. Again, use $\mathbf{S_R}$ to relock!

C.3.2 Locking the blue laser to the correct transition

The way to lock the blue laser to the correct transition basically comprises three steps: finding the first absorption signal by scanning the Ti:Sapph laser cavity, locking the laser to the PDH cavity, and finally stabilizing the latter with the SAS setup. A detailed description follows.

Finding the correct absorption signal

1. Turn the wavemeter on!

2. Carefully tweak the birefringent filter (**BS**) and the etalon (**E**) in the Ti:Sapph laser cavity to tune the wavelength of the laser. The correct wavelength range is obtained when the fluorescence signal in the He cell can be observed. For our system, this is usually the case around $777.9500 - 777.9517$ nm.

3. Lock the frequency doubling cavity! In order to do so, switch the scanning signal from the internal function generator of the HC controller off, enable the feedback signal with S2, and reset the the integrator with S_R. If the cavity jumps out of the lock due to integral windup, use S_R to relock it. Before proceeding further, the output power of the frequency doubling cavity should be maximized as described in C.3.1.

4. With the frequency doubling cavity locked, find the correct absorption signal! Scan the Ti:Sapph laser cavity at a frequency of $\sim$ 13 Hz by flipping **S3** and changing the DC offset thereafter. Once the absorption signal appears, tune the DC offset further to the absorption peak at the highest wavelength which corresponds to the desired transition $2\ ^3S_1 \rightarrow 3\ ^3P_2$, because of the fine structure transitions $2\ ^3S_1 \rightarrow 3\ ^3P_J$, where $J = 0, 1, 2$, it is the lowest one in energy.

Locking the Ti:Sapph laser to the PDH cavity

1. Disabling **S3**, stop scanning the Ti:Sapph laser cavity!

2. Switch the internal function generator in summing box Σ_2 off to deactivate the scan of the PDH cavity!

3. Immediately turn **S1** and **S2** on and quickly adjust the gains of the two integrator stages simultaneously until the transmission signal from **PD2** on the oscilloscope screen jumps up to the same intensity as the one of the transmission peak during the scan! Afterwards, optimize the integral and proportional gain to minimize the deviations of the locking signal from resonance! Successfully doing so will minimize the linewidth of the laser.

Locking the PDH-cavity to the atomic reference

1. Make sure that **S6** of the lock-box is set to "scan"!

2. Enable the feedback loop by switching **S5** on!

3. Adjust the DC offset of Σ_2 until the absorption signal reappears! Doublecheck, if it is the correct transition! In order to see both the $2\,^3S_1 \rightarrow 3\,^3P_2$ transition and the crossover (330 MHz apart) between the correct and the $2\,^3S_1 \rightarrow 3\,^3P_1$ transition during one scan period, the gain **G5** can be increased.

4. Flip **S6** to "lock"! Now the laser is locked.

Bibliography

[1] T. Breeden and H. Metcalf, *Stark Acceleration of Rydberg Atoms in Inhomogeneous Electric Fields*. Phys. Rev. Lett. **47**, 1726 (1981).

[2] U. Gaubatz, P. Rudecki, M. Becker, S. Schiemann, M. Kulz, and K. Bergmann, *Population switching between vibrational levels in molecular beams*. Chem. Phys. Lett. **149**, 463 (1988).

[3] J. R. Kuklinski, U. Gaubatz, F. T. Hioe, and K. Bergmann, *Adiabatic population transfer in a three-level system driven by delayed laser pulses*. Phys. Rev. A **40**, 6741 (1989).

[4] U. Gaubatz, P. Rudecki, S. Schiemann, and K. Bergmann, *Population transfer between molecular vibrational levels by stimulated Raman scattering with partially overlapping laserfields. A new concept and experimental results*. J. Chem Phys. **92**, 5363 (1990).

[5] S. H. Autler and C. H. Townes, *Stark Effect in Rapidly Varying Fields*. Phys. Rev. **100**, 703 (1955).

[6] P. Meystre, *Atom Optics* (Springer-Verlag, New York, 2001).

[7] H. J. Metcalf and P. v. d. Straaten, *Laser Cooling and Trapping* (Springer-Verlag, New York, 1999).

[8] L. de Broglie, *Radiations-Ondes et Quanta*. Comp. Rend. Ac. Sci. **177**, 507 (1923).

[9] C. Davisson and L. H. Germer, *Diffraction of Electrons by a Crystal of Nickel*. Phys. Rev. **30**, 705 (1927).

[10] O. Stern, *Bending a molecular ray by crystal lattice face*. Naturwiss. **17**, 391 (1929).

[11] R. Frisch, *Experimenteller Nachweis des Einsteinschen Strahlungsrückstoßes*. Zeits. f. Phys. **86**, 42 (1933).

[12] P. J. Martin, B. G. Oldaker, A. H. Miklich, and D. E. Pritchard, *Bragg scattering of atoms from a standing light wave*. Phys. Rev. Lett. **60**, 515 (1988).

[13] H. Pu, C. Search, W. Zhang, and P. Meystre, *Atom Optics - From de Broglie Waves to Heigenberg Ferromagnets*. Fortschr. Physics **50**, 664 (2002).

[14] T. W. Hänsch and A. L. Schawlow, *Cooling of gases by laser radiation*. Opt. Comm. **13**, 68 (1975).

[15] D. Wineland and H. Dehmelt, *Proposed* $10^{14}\ \Delta\nu < \nu$ *laser fluorescence spectroscopy on* TI^+ *mono-ion oscillator III*. Bull.Am.Phys.Soc. **20**, 637 (1975).

[16] S. N. Bose, *Plancks Gesetz und Lichtquantenhypothese*. Zeits. f. Phys. **26**, 178 (1924).

[17] A. Einstein, Sitzungsber. Kgl. Preuss. Akad. Wiss. **1924**, 261 (1924).

[18] M. H. Anderson, J. R. Ensher, M. R. Matthews, C. E. Wieman, and E. A. Cornell, *Observation of Bose-Einstein condensation in a dilute atomic vapor*. Science **269**, 198 (1995).

[19] K. B. Davis, M. O. Mewes, M. R. Andrews, N. J. v. Druten, D. S. Durfee, D. M. Kurn, and W. Ketterle, *Bose-Einstein Condensation in a Gas of Sodium Atoms*. Phys. Rev. Lett. **75**, 3969 (1995).

[20] E. W. Hagley, L. Deng, M. Kozuma, J. Wen, K. Helmerson, S. L. Rolston, and W. D. Phillips, *A Well-Collimated Quasi-Continuous Atom Laser*. Science **283**, 1706 (1999).

[21] Y. B. Ovchinnikov, J. H. Müller, M. R. Doery, E. J. D. Vredenbregt, K. Helmerson, S. L. Rolston, and W. D. Phillips, *Diffraction of a Released Bose-Einstein Condensate by a Pulsed Standing Light Wave*. Phys. Rev. Lett. **83**, 284 (1999).

[22] M. Kozuma, L. Deng, E. W. Hagley, J. Wen, R. Lutwak, K. Helmerson, S. L. Rolston, and W. D. Phillips, *Coherent Splitting of Bose-Einstein Condensed Atoms with Optically Induced Bragg Diffraction*. Phys. Rev. Lett. **82**, 871 (1999).

[23] L. Deng, E. W. Hagley, J. Wen, M. Trippenbach, Y. Band, P. S. Julienne, J. E. Simsarian, K. Helmerson, S. L. Rolston, and W. D. Phillips, *Four-wave mixing with matter waves*. Nature **398**, 218 (1999).

[24] J. J. McClelland, in *Handbook of Nanostructured Materials and Nanotechnology*, edited by H. S. Nalwa (Academic Press, San Diego, 2000), Vol. One, pp. 335–385.

[25] E. Vliegen and F. Merkt, *Normal-Incidence Electrostatic Rydberg Atom Mirror*. Phys. Rev. Lett. **97**, 033002 (2006).

[26] G. R. Woestenenk, J. W. Thomsen, M. v. Rijnbach, P. v. d. Straten, and A. Niehaus, *Construction of a low velocity metastable helium atomic beam*. Rev. Sci. Inst. **72**, 3842 (2001).

[27] T. F. Gallagher, *Rydberg Atoms* (Cambridge University Press, Cambridge, 1994).

[28] W. N. Hartley, *LVI.– On homologous spectra*. J. Chem. Soc., Trans. **43**, 390 (1883).

[29] J. R. Rydberg, *On the Structure of the Line Spectra of the Chemical Elements*. Phil.Mag.5th Ser **29**, 331 (1890).

[30] K. T. T. Singer, *Interactions in an ultracold gas of Rydberg atoms*. Ph.D. thesis, Albert-Ludwigs-University, 2004.

[31] H. A. Bethe and E. E. Salpeter, *Quantum Mechanics of one-and two-electron atoms* (Academic Press Inc., New York, 1957).

[32] M. J. Seaton, *Quantum defect theory*. Rep. Prog. Phys. **46**, 167 (1983).

[33] C. J. Lorenzen and K. Niemax, *Quantum Defects of the* $n\,^2P_{1/2;3/2}$ *Levels in* ^{39}KI *and* ^{85}RbI. Phys. Script. **27**, 300 (1983).

[34] T. Bergeman, Professor.

[35] M. L. Zimmerman, M. G. Littman, M. M. Kash, and D. Kleppner, *Stark structure of the Rydberg states of alkali-metal atoms*. Phys. Rev. A **20**, 2251 (1979).

[36] H. J. Silverstone, *Perturbation theory of the Stark effect in hydrogen to arbitrarily high order*. Phys. Rev. A **18**, 1853 (1978).

[37] E. Luc-Koenig and A. Bachelier, *Systematic theoretical study of the Stark spectrum of atomic hydrogen.*. J. Phys. B **13**, 1743 (1980).

[38] P. M. Koch, *Resonant States in the Nonperturbative Regime: The Hydrogen Atom in an Intense Electric Field*. Phys. Rev. Lett. **41**, 99 (1978).

[39] C. T. W. Lahaye and W. Hogervorst, *Stark manifolds and electric-field-induced avoided level crossing in helium Rydberg states*. Phys. Rev. A **39**, 5658 (1989).

[40] G. W. F. Drake, *High Precision Theory of Atomic Helium*. Phys. Script. **T83**, 83 (1999).

[41] D. R. Bates and A. Damagaard, *The Calculation of the Absolute Strength of Spectral Lines*. Phil. Trans. Roy. Soc. Lond. A **242**, 101 (1949).

[42] W. C. Martin, *Improved ^4He I 1snl ionization energy, energy levels, and Lamb shifts for 1sns and 1snp terms*. Phys. Rev. A **36**, 3575 (1987).

[43] S. H. Lee, *Coherent Manipulation of Rydberg Helium Atoms in Inhomogeneous Electric Fields*. Ph.D. thesis, Stony Brook University, 2006.

[44] J. C. J. Koelemeij, *Interaction of UV light with cold metastable helium atoms*. Ph.D. thesis, Vrije Universiteit Amsterdam, 2004.

[45] A. Einstein, *Zur Quantentheorie der Strahlung*. Physik. Zeits. **18**, 121 (1917).

[46] K. Bergmann, H. Theuer, and B. W. Shore, *Coherent population transfer among quantum states of atoms and molecules*. Rev. Mod. Phys. **70**, (1998).

[47] N. V. Vitanov, M. Fleischhauer, B. W. Shore, and K. Bergmann, *Coherent manipulation of atoms and molecules by sequential laser pulses*. Adv. Atom. Mol. Opt. **46**, 55 (2001).

[48] J. Oreg, F. T. Hioe, and J. Eberly, *Adiabatic following in multilevel systems*. Phys. Rev. A **29**, 690 (1984).

[49] C. V. Raman, *A new radiation*. Ind. J. Phys. **2**, 387 (1928).

[50] N. Bloembergen, *The Stimulated Raman Effect*. Am. J. Phys. **35**, 989 (1967).

[51] J. C. Camparo and R. Frueholz, *A dressed atom interpretation of adiabatic rapid passage*. J.Phys.B: At. Mol. Phys. **17**, 4169 (1984).

[52] J. G. Powles, *The adiabatic fast passage experiment in magnetic resonance*. Proc. Phys. Soc. **71**, 497 (1958).

[53] M. O. Scully and M. S. Zubairy, *Quantum Optics* (Cambridge University Press, Cambridge, 1997).

[54] P. M. Farrell and W. R. MacGillivray, *On the consistency of Rabi frequency calculations*. J. of Phys. A **28**, 209 (1995).

[55] I. I. Rabi, *Space Quantization in a Gyrating Magnetic Field*. Phys.Rep. **51**, 652 (1937).

[56] I. I. Sobelman, *Atomic Spectra and Radiative Transitions* (Springer, Berlin, 1979).

[57] E. P. Wigner, *Einige Folgerungen aus der Schrödingerschen Theorie für die Termstrukturen*. Zeits. f. Phys. **43**, 624 (1927).

[58] C. Eckart, *The Application of Group Theory to the Quantum Dynamics of Monatomic Systems*. Rev. Mod. Phys. **2**, 305 (1930).

[59] B. W. Shore, *The Theory of Coherent Atomic Excitation* (Wiley, New York, 1990).

[60] B. W. Shore, K. Bergmann, A. Kuhn, S. Schiemann, and J. Oreg, *Laser-induced population transfer in multistate systems: A comparative study*. Phys. Rev. A **45**, 5297 (1992).

[61] C. Cohen-Tannoudji, J. Dupont-Roc, and G.Grynberg, *Atom-Photon Interactions* (Wiley-Interscience, New York, 1992).

[62] R. Garcia-Fernandez, A. Ekers, J. Klavins, L. P. Yatsenko, N. N. Bezuglov, B. W. Shore, and K. Bergmann, *Autler-Townes effect in a sodium molecular-ladder scheme*. Phys. Rev. A **71**, 023401 (2005).

[63] H. L. Bethlem, M. Tarbutt, J. Küpper, D. Carty, K. W. E. Hinds, and G. Meijer, *Alternating Gradient Focusing and Deceleration of Polar Molecules*. arXiv.org:physics/0604020 v1 (2006).

[64] M. Morinaga, *Focusing ground-state atoms with an electrostatic field*. Appl. Phys. B **79**, 679 (2004).

[65] W. Ketterle and D. E. Pritchard, *Trapping and focusing ground state atoms with static fields*. Appl. Phys. B **54**, 403 (1992).

[66] S. Earnshaw, *On the nature of the molecular forces which regulate the constitution of the luminiferous ether*. Trans. Camb. Phil. Soc. **7**, 97 (1842).

[67] W. Jones, *Earnshaw's theorem and the stability of matter*. Eur. J. Phys. **1**, 85 (1980).

[68] J. G. Kalnins, J. M. Amini, and H. Gould, *Focusing a fountain of neutral cesium atoms with an electrostatic lens triplet*. Phys. Rev. A **72**, 043406 (2005).

[69] H.-R. Noh, K. Shimizu, and F. Shimizu, *Imaging of an atomic beam with electrostatic lenses*. Phys. Rev. A **61**, 041601 (2000).

[70] J. G. Kalnins, G. Lambertson, and H. Gould, *Improved alternating gradient transport and focusing of neutral molecules*. Rev. Sci. Inst. **73**, 2557 (2002).

[71] F. Pereira Dos Santos, J. Léonard, J. Wang, C. J. Barrelet, F. Perales, E. Rasel, C. S. Unnikrishnan, M. Leduc, and C. Cohen-Tannoudji, *Bose-Einstein condensation of metastable helium*. Phys. Rev. Lett. **86**, 3459 (2001).

[72] A. Robert, O. Sirjean, A. Browaeys, J. Poupard, S. Nowak, D. Boiron, C. I.Westbrook, and A. Aspect, *A Bose-Einstein condensate of metastable atoms*. Science **292**, 461 (2001).

[73] N. Greenwood and A. Earnshaw, *Chemistry of the Elements*, 2nd ed. (Butterworth-Heinemann, Oxford, 1997).

[74] J. R. Woodworth and H. W. Moos, *Experimental determination of the single-photon transition rate between the* $2\,^3S_1$ *and* $1\,^1S_0$ *states of He I*. Phys. Rev. A **12**, 2455 (1975).

[75] G. Łach and K. Pachucki, *Forbidden transistions in the helium atom*. Phys. Rev. A **64**, 042510 (2001).

[76] F. M. Penning, *Über Ionisation durch metastabile Atome*. Naturwiss. **15**, 818 (1927).

[77] D. W. Fahey, W. F. Parks, and L. D. Schearer, *High flux beam source of thermal rare-gas metastable atoms*. J. Phys. E **13**, 381 (1980).

[78] J. S. Hack, *Laser Cooling in the Recoil Domain*. Ph.D. thesis, Stony Brook University, 2001.

[79] http://www.sintec keramik.com.

[80] W. Rooijakkers, W. Hogervorst, and W. Vassen, *An intense collimated beam of metastable helium atoms by two-dimensional laser cooling*. Opt. Comm. **123**, 321 (1996).

[81] M. T. Widmer, *Measurements of 1-D Quantized Motion in Laser Cooled Metastable Helium*. Ph.D. thesis, Stony Brook University, 1995.

[82] M. J. Bellanca, *Sub-Recoil Velocity Selective Resonances in Metastable Helium*. Ph.D. thesis, Stony Brook University, 1999.

[83] J. L. Wiza, *Microchannel Plate Detectors*. Nucl. Inst. Meth. **162**, 587 (1979).

[84] M. J. Partlow, *Bichromatic Collimation to make an Intense Helium Beam*. Ph.D. thesis, Stony Brook University, 2004.

[85] N. A. Surplice and R. J. D'Arcy, *Reduction in the work function of stainless steel by electric fields*. J. Phys. F **2**, L8 (1972).

[86] R. D. Rundel, F. B. Dunning, J. S. Howard, J. P. Riola, and R. F. Stebbings, *A Gas Cell Method for the Measurement of Secondary Electron Ejection Coefficients for Metastable Atoms on Metal Surfaces*. Rev. Sci. Inst. **44**, 60 (1973).

[87] R. V. Pound, *Electronic Frequency Stabilization of Microwave Oscillators.* Rev. Sci. Inst. **17**, 490 (1946).

[88] R. W. Drever and J. L. Hall, *Laser Phase and Frequency Stabilization Using an Optical Resonator.*. Appl. Phys. B **31**, 97 (1983).

[89] W. Demtröder, *Laser Spectroscopy: Basic Concepts and Instrumentation*, 3rd ed. (Springer-Verlag, Heidelberg, 2003).

[90] C. J. Foot, *Atomic Physics*, *Oxford Master Series in Atomic, Optical, and Laser Physics* (Oxford University Press, New York, 2005).

[91] T. W. Hänsch and B. Couillaud, *Laser Frequency Stabilization by Polarization Spectroscopy of a Reflecting Reference Cavity.* Opt. Comm. **35**, 441 (1980).

[92] R. W. Boyd, *Nonlinear Optics* (Academic Press, San Diego, 1992).

[93] B. E. A. Saleh and M. C. Teich, *Fundamentals of Photonics* (John Wiley & Sons, New York, 1991).

[94] Y. R. Shen, *The Principles of Nonlinear Optics* (John Wiley & Sons, New York, 1984).

[95] E. D. Black, *An introduction to Pound-Drever-Hall laser frequency stabilization.* Am. J. Phys. **69**, 79 (2001).

[96] M. Weel and A. Kumarakrishnan, *Laser-frequency stabilization using a lock-in amplifier.* Can. J. Phys. **80**, 1449 (2002).

[97] TekhnoScan, *Resonant Frequency Doubler, model FD-SF-07, for CW single frequency lasers.*